Department of Physics and Astronomy

Heidelberg University

Master thesis

in Physics

submitted by

Lennart Kai Röver

born in Lörrach

2021

Constraining Single Field Inflation

with the Square Kilometer Array

This Master thesis has been carried out by Lennart Kai Röver

at the

Institute for Theoretical Physics

under the supervision of

Prof. Dr. Tilman Plehn

Einschränkung der Inflation mit dem Square Kilometer Array:

Das Square Kilometer Array (SKA) ermöglicht es, die Verteilung der Wasserstoffatome im Universum über große Rotverschiebungsskalen hinweg zu messen. Mit dem dreidimensionalen 21 cm Spektrum können nicht nur Präzisionsmessungen von astrophysikalischen Phänomenen, sondern auch von kosmologischen Größen vorgenommen werden. Bereits für einen kleinen Rotverschiebungsbereich kann das SKA Hubble slow-roll Parameter bedeutend stärker einschränken als die Cosmic Micorwave Background (CMB) Messungen der Temperaturanisotropien des Planck Satelliten. Diese Arbeit liefert eine kurze Einführung in die Physik der Inflation, erklärt wie das Krümmungsspektrum direkt nach der Inflation durch die Hubble slow-roll Parameter konstruiert werden kann und stellt eine Möglichkeit vor, SKA Daten zu simulieren. Mit Hilfe dieser simulierten Daten werden schließlich Grenzen für die Hubble slow-roll Parameter aus den kombinierten Planck und simulierten SKA Daten berechnet.

Constraining Single Field Inflation with the Square Kilometer Array:

The Square Kilometer Array (SKA) will map the distribution of neutral hydrogen in the Universe over a vast redshift range. The three-dimensional 21 cm power spectrum found through this map can be used to perform precision tests not only in astrophysics but also in cosmology. Even considering only a small redshift range it will allow to significantly improve current constraints on the Hubble slow-roll parameters when combined with the Cosmic Microwave Background (CMB) anisotropies measurement of the Planck satellite. This thesis will give a short introduction into the physics of inflation, explore how to construct a primordial power spectrum based on the Hubble slow-roll parameters, present a way to construct a likelihood for the SKA and provide improved constraints on the Hubble slow-roll parameters when combining this likelihood with the one computed with the Planck 2018 data.

Contents

1 Introduction **6**

2 Inflation **8**
2.1 Geometry and Dynamics 8
2.2 The Horizon Problem 9
2.2.1 Solution to the Horizon Problem 11
2.3 The Flatness Problem 12
2.4 Equivalent Ways of Characterizing Inflation 12
2.5 Scalar Field Inflation 14
2.6 Slow-Roll Inflation 15
2.7 Reheating 17

3 Cosmological Perturbations **19**
3.1 Generalities 19
3.1.1 Linear Perturbations 19
3.1.2 Gauge Choice 19
3.1.3 Types of Perturbations 19
3.2 The Inhomogeneous Universe 20
3.2.1 Scalar Metric Perturbations 20
3.2.2 Matter Perturbations 21
3.2.3 Gauge Invariant Variables 21
3.3 The Quantum Origins of Structure 22
3.4 The Mode Equation 24
3.4.1 Quantization and Boundary Conditions 24
3.5 Tensor Perturbations 25

4 Contact with the Observation **27**
4.1 Contact with the CMB 27
4.1.1 Temperature Fluctuations 27
4.1.2 Polarization 28
4.2 Contact with Large Scale Structures 30
4.2.1 Galaxy Surveys 31
4.2.2 21cm Intensity Mapping 31

5 Brief Introduction to MCMC **32**

6 Numerical Analysis **34**
6.1 Primordial Power Spectra . . . 34
6.1.1 Spectral Index and its Runnings . . . 34
6.1.2 Integration of the Mode Equation . . . 35
6.2 CLASS . . . 40
6.3 MontePython . . . 42
6.4 SKA Likelihood . . . 42

7 Comparison to Planck Results **46**
7.1 ΛCDM Contours . . . 46
7.2 Spectral Index and its Runnings . . . 50
7.3 Slow-roll Parameters . . . 52

8 Square Kilometer Array Results **58**
8.1 Spectral Index and its Runnings . . . 58
8.2 Slow-roll Parameters . . . 62
8.2.1 Two-dimensional Results . . . 62
8.2.2 Three-dimensional Results . . . 65

9 Combined Results **72**
9.1 Spectral Index and its Runnings . . . 72
9.2 Slow-roll Parameters . . . 74

10 Summary and Conclusion **80**

A Nuisance parameters **84**

B SKA with Four Slow-roll Parameters **85**

C Lists **86**
C.1 List of Figures . . . 86
C.2 List of Tables . . . 88

D Bibliography **89**

1 Introduction

Inflation is a period in the early Universe first proposed by Guth [1981] to explain some of the open questions in the standard model of cosmology. It postulates a phase of accelerated expansion in the early Universe, explaining the isotropy of the Cosmic Microwave Background (CMB) even on scales that were never in causal contact in the standard cosmological model (ΛCDM). Cosmological perturbations during inflation give a way to seed structure formation. Thus, inflation can on the one hand be probed by considering the temperature anisotropies in the CMB Akrami et al. [2020], which reflect the cosmological perturbations during inflation. On the other hand, the density power spectrum encoding the distribution of dark and luminous matter yields additional information on this period of accelerated expansion.

In this thesis single field inflation is considered, which can be constrained through the properties of the curvature power spectrum at the end of inflation. For that purpose, it is parameterized as a Taylor series around an arbitrarily chosen pivot scale k_*. The parameters influencing the shape of the spectrum are the scalar amplitude A_s, the spectral index n_s and further logarithmic derivatives of the spectral index with respect to the comoving wave number. This approach allows to derive constraints on inflationary models by computing these quantities in the model considered. Single field inflation can also be studied in a model independent way by constraining the Hubble function during inflation through its derivatives with respect to the inflaton field. For more desirable statistical properties so called Hubble slow-roll parameters have been constructed from these derivatives. An early description of the Hubble slow-roll parameters can be found in Liddle et al. [1994] and Stewart and Gong [2001]. The focus of this thesis will be on the second approach with the exact method described in Lesgourgues et al. [2008]. Here, the Hubble function is approximated as a Taylor series in the inflaton field values, which is then used to compute the background evolution and the solution to the mode equation described in Mukhanov et al. [1992].

In addition to the original paper, this approach has been used in the generation of constraints for the Hubble slow-roll in Hamann et al. [2008], Ade et al. [2016] and Akrami et al. [2020]. This thesis will reproduce the Planck 2018 result, and also give a forecast for the constraints that can be obtained by applying the same method to the Square Kilometer Array (SKA) which being constructed in Australia and South Africa. The SKA will be able to measure the 21 cm hyperfine line of neutral hydrogen during the Epoch of Reionization and into the dark ages Dewdney [2015]. Useful descriptions of the SKA and its properties can be found in Dewdney [2015], Pritchard et al. [2015] and Bacon et al. [2020].

Forecasts for the noise level, foreground removal and likelihoods for SKA have been found by Bowman et al. [2007], McQuinn et al. [2006], Mao et al. [2008] and Tegmark and Zaldarriaga [2009]. Similar to Muñoz et al. [2017], this thesis focuses on the redshift region of 8 to 10 and bases the construction of the SKA likelihoods on their analysis. However, the parameters used to constrain inflation as well as the method to compute the contours are chosen differently.

There are several works on constraining inflation using the SKA Kohri et al. [2013], Muñoz et al. [2017], Pourtsidou [2016] where the formalism used relies on constraining the curvature spectrum after inflation. In Barger et al. [2009b], the Hubble slow-roll parameters are constrained, however, the formalism used in that work relies on computing the spectral index and its running from them. All three of these rely on the Fisher matrix approximation in their analysis. In addition to constraining the Hubble function during inflation directly, the approach in this thesis uses Markov chain Monte Carlo to derive the contours. This provides a method to probe the parameter space in a more detailed way. Recently Sprenger et al. [2019] have used the same method to find constraints on cosmological parameters using the SKA, however, they consider only the scalar amplitude and spectral index to constrain the primordial spectrum. They also consider a different redshift region to derive their constraints.

Chapter 2 of the thesis is meant to give a short overview over single field inflation and provide an overall intuition for the more exact calculations presented in chapter 3. It deals with primordial fluctuations as the origin of structures in the Universe and describes the evolution of the fluctuations using the mode equation until the end of inflation. Chapter 4 briefly describes the angular power spectra measured by the Planck satellite, the power spectrum associated with large scale structures and how they are linked to the primordial power spectrum.

Chapters 5 and 6 give a short overview over the methods used and the different codes and packages relevant to find the power spectra at arbitrary redshifts. This includes a description of the slow-roll parameters used in the analysis as well as how the mode equation and background equation are solved using them as an approximation.

The last three chapters focus on the results obtained through the setup described in 6. In chapter 7 the setup is used to reproduce the Planck 2018 Akrami et al. [2020] results to verify that it is viable to use it for different experiments. The spectral index and its runnings as well as the Hubble slow-roll parameters are then constrained using only the SKA in chapter 8 and finally using both of them combined in chapter 9.

2 Inflation

The inflationary paradigm was first proposed by Guth [1981] to cure the standard cosmological model (ΛCDM) of both the horizon and the flatness problem. Instead of setting an initial condition for the ΛCDM such that the Universe is homogeneous at early times even over distances that were not in causal contact, the inflationary paradigm postulates a period of accelerated expansion of a causally connected region which then makes up the entire observed Universe. This would also explain the small curvatures observed today.

This chapter is devoted to the basics of single field inflation, how it solves the problems mentioned above and forms a foundation upon which all further discussion in this thesis can be based.

2.1 Geometry and Dynamics

For the purpose of this thesis the Universe will be considered as a Friedmann-Lemaître-Robertson-Walker (FLRW) Universe, here the metric is defined as

$$\mathrm{d}s^2 = -\mathrm{d}t^2 + a^2(t)\left[\frac{\mathrm{d}r^2}{1-kr^2} + r^2\mathrm{d}\Omega^2\right] \tag{2.1}$$

where a is the scale factor, $k \in \{-1, 0, 1\}$ characterizes the spatial curvature and the speed of light is set for the rest of this thesis. Here, $k = -1$ corresponds to negative, $k = 0$ to zero and $k = 1$ to positive curvature. The metric described in (2.1) exhibits a rescaling symmetry

$$a \to \lambda a, \qquad r \to \frac{r}{\lambda}, \qquad k \to \lambda^2 k.$$

Spacetime remains unchanged under the simultaneous rescaling of these quantities. This allows to set a value for the scale factor today as $a_0 = a(t_0) = 1$ which in turn means that the scale factor is set to be dimensionless while r and $k^{-1/2}$ inherit the dimension of length. By a variable transformation

$$r^2 = \Phi_k(\chi^2) = \begin{cases} \sinh^2\chi & k = -1 \\ \chi^2 & k = 0 \\ \sin^2\chi & k = +1 \end{cases} \tag{2.2}$$

the metric can be rewritten as

$$\mathrm{d}s^2 = -\mathrm{d}t^2 + a^2(t)(\mathrm{d}\chi^2 + \Phi_k(\chi^2))(\mathrm{d}\theta^2 + \sin^2\theta\mathrm{d}\phi^2). \tag{2.3}$$

Since the causal structure of the Universe depends on the propagation of light which travels along null geodesics $ds^2 = 0$, it is convenient to define conformal time as

$$\tau = \int \frac{\mathrm{d}t}{a(t)}. \tag{2.4}$$

The metric then takes the form

$$\mathrm{d}s^2 = a(\tau)^2 \left[-\mathrm{d}\tau^2 + (\mathrm{d}\chi^2 + \Phi_k(\chi^2))(\mathrm{d}\theta^2 + \sin^2\theta \mathrm{d}\phi^2)\right]. \tag{2.5}$$

For the metric defined as above the dynamics of the Universe can be found by considering the Einstein equation

$$G_{\mu\nu} = 8\pi G T_{\mu\nu} - \Lambda g_{\mu\nu}$$

where the Einstein tensor is governed by the spacetime curvature and the stress-energy tensor depends on the matter content of the Universe. In the following, units are chosen such that $8\pi G = 1$.

The stress energy-tensor can be derived using the isotropy and homogeneity of the Universe to be the stress-energy tensor of a perfect fluid. It follows a four component conservation equation $\nabla_\mu T^\mu_\nu = 0$, which for a perfect fluid, can be written as

$$\dot{\rho} + 3\frac{\dot{a}}{a}(\rho + P) = 0, \tag{2.6}$$

where ρ is the energy density and P the pressure in the fluid rest frame. Combining this with the Einstein tensor for FLRW-space yields the Friedmann equations

$$H^2 = \frac{\rho}{3} - \frac{k}{a^2} \tag{2.7}$$

$$\frac{\ddot{a}}{a} = -\frac{1}{6}(\rho + 3P). \tag{2.8}$$

Here; the $H = \frac{\dot{a}}{a}$ denotes the Hubble parameter. In a flat Universe one can define the critical density as

$$\rho_{crit,0} = 3H_0^2$$

where the 0 denotes present time.

2.2 The Horizon Problem

In order to understand the motivation for postulating a period of accelerated expansion, the concept of horizons, the particle horizon in particular, becomes relevant. It is the greatest comoving coordinate distance from which an observer at time t is able to receive signals moving at the speed of light.

Since radial propagation with the speed of light is governed by

$$\mathrm{d}s^2 = a(\tau)^2 \left[\mathrm{d}\tau^2 - \mathrm{d}\chi^2\right] = 0. \tag{2.9}$$

Radial null geodesics satisfy $\chi(\tau) = \pm\tau + \text{const}$. This allows to quantify the definition of the comoving particle horizon as

$$\chi_{ph} = \tau - \tau_i = \int_{t_i}^{t} \frac{\mathrm{d}t}{a(t)}. \tag{2.10}$$

Here, τ_i is some initial comoving time, typically the time of the Big Bang. The comoving particle horizon can also be defined in terms of the comoving Hubble radius $(aH)^{-1}$ via

$$\chi_{ph} = \int_{t_i}^{t} \frac{\mathrm{d}t}{a(t)} = \int_{a_i}^{a} \frac{\mathrm{d}a}{a\dot{a}} = \int_{\ln a_i}^{\ln a} (aH)^{-1} \mathrm{d}\ln a, \tag{2.11}$$

where $a_i = 0$ is the scale factor at the Big Bang singularity.

In a Universe dominated by a perfect fluid with constant equation of state $\omega = \frac{P}{\rho}$ the comoving Hubble radius can be expressed as

$$(aH)^{-1} = H_0^{-1} a^{\frac{1}{2}(1+3\omega)}, \tag{2.12}$$

where H_0 denotes the current Hubble parameter. For the radiation and matter dominated epochs the equation of state fulfills $(1 + 3\omega) > 0$. The integral equation for the particle horizon can then be solved, which yields

$$\chi_{ph} = \frac{2H_0^{-1}}{1+3\omega}[a^{\frac{1}{2}(1+3\omega)} - a_i^{\frac{1}{2}(1+3\omega)}] \tag{2.13}$$

$$= \frac{2}{1+3\omega}[(aH)^{-1} - (aH)_i^{-1}]. \tag{2.14}$$

Particles that are at comoving coordinate distance greater than the particle horizon can never have communicated. Particles that are at greater comoving coordinate distance than the comoving Hubble radius $(aH)^{-1}$ cannot communicate in one expansion time $t_H = H^{-1}$. For standard Big Bang cosmology the particle horizon is dominated by the Hubble radius at late times. This can be seen by setting $a_i \to 0$ while keeping in mind that the equation of state still fulfills $(1 + 3\omega) > 0$.

The horizon problem arises when considering two points in the Cosmic Microwave Background (CMB), the light emitted right after the recombination of electrons and protons, in opposite directions in the sky. Using equation (2.13) it is possible to construct a particle horizon for each of these points. Comparing the size of the particle horizons with the spatial difference of the points at the time of CMB emission results in the conclusion that they were not in causal contact at any time in standard Big Bang cosmology. However, the CMB is almost perfectly isotropic, the points in opposite directions of the sky are almost exactly at the same temperature. This observation seems to imply that, contrary to the result obtained by assuming standard Big Bang cosmology, at least all of the observable points in the CMB appear to have been in causal contact at some point in the history of the Universe.

2.2.1 Solution to the Horizon Problem

The horizon problem can be solved if there is some process that increases the size of the particle horizon in the early Universe. A possible way of achieving this is to assume a shrinking Hubble radius with

$$\frac{\mathrm{d}}{\mathrm{d}t}(aH)^{-1} < 0. \tag{2.15}$$

If this period of decreasing Hubble radius lasts long enough, it can significantly expand the particle horizon of any point. This condition requires a fluid with $(1 + 3\omega) < 0$. Taking this into account and letting the scale factor go to zero in equation 2.13 will lead to the conclusion that the size of the particle horizon must now be dominated by the early time Hubble radius. This pushes the beginning of the Universe to negative conformal times and $\tau = 0$ is the transition point between ordinary Big Bang cosmology and inflationary cosmology Baumann [2012]. The statement that the period of decreasing Hubble radius must last long enough can be made more precise by assuming that at least all of the observable Universe today must have been in causal contact at some point to solve the horizon problem. The Hubble radius of the Universe today must then fit into the Hubble radius at the beginning of inflation.

$$(a_0 H_0)^{-1} < (a_I H_I)^{-1} \tag{2.16}$$

To get an estimate of how much the Hubble radius needs to decrease during inflation the expansion of the Universe after inflation needs to be estimated. This can be done by assuming the Universe to be radiation dominated after inflation ($\omega = 1/3$) and that its expansion is adiabatic. In that case equation (2.12) can be used to find

$$\frac{a_0 H_0}{a_E H_E} = \frac{a_0}{a_E}\frac{a_E^2}{a_0^2} = \frac{a_E}{a_0} \sim \frac{T_0}{T_E} \sim 10^{-28}. \tag{2.17}$$

Here the temperature at the end of inflation, the reheating temperature, is estimated as $T_E \sim 10^{15}$ GeV and the current temperature of the Universe is $T_0 = 10^{-13}$ eV Baumann [2012]. This allows to find by how much the Hubble radius has decreased during inflation

$$\frac{(a_I H_I)^{-1}}{(a_E H_E)^{-1}} > 10^{28} \tag{2.18}$$

Under the assumption that the Hubble parameter is constant during inflation, which will be motivated later, this can be rewritten as

$$\frac{a_E}{a_I} > 10^{28}, \qquad \ln\left(\frac{a_E}{a_I}\right) > 64. \tag{2.19}$$

Thus, the scale factor increases by a factor of e^{64} or by 64 *e-folds*.

2.3 The Flatness Problem

In addition to the horizon problem, there is another puzzle in the ΛCDM which inflation is able to address. By defining the critical density in a time dependent way as $\rho_{crit} > (a) \equiv 3H(a)^2$ and considering the curvature parameter $\Omega_k \equiv \Omega - 1 = \frac{\rho - \rho_{crit}}{\rho_{crit}}$ it is possible to find

$$\Omega - 1 = \frac{3k}{a^2 \rho_{crit}} = \frac{k}{(aH)^2} \tag{2.20}$$

by utilizing the Friedmann equation (2.7). This curvature parameter can be measured at current time to be of order one. As the Hubble radius increases in the standard cosmological model, the value of the curvature parameter must be fine tuned to a very small value in order to explain its value today. In fact, at the Planck scale assumes the value Baumann [2012]

$$|\Omega(a_{pl}) - 1| \leq \mathcal{O}(10^{-61}). \tag{2.21}$$

Similarly to the horizon problem, the flatness problem can be solved by requiring a period in the evolution of the Universe where the Hubble radius decreases. As with the horizon problem the amount the Hubble function needs to decrease to solve the flatness problem can be estimated. This is done by setting the curvature parameter at the beginning of the radiation phase, i.e. the end of inflation to the value in expression (2.21). Its value at the beginning of inflation should be of order one to avoid having to fine tune its initial value. This allows to find

$$\left(\frac{\Omega(a_I) - 1}{\Omega(a_E) - 1} \right)^{\frac{1}{2}} = \frac{(a_I H_I)^{-1}}{(a_E H_E)^{-1}} \sim \mathcal{O}(10^{30}), \tag{2.22}$$

which is consistent with the number found in expression 2.18.

2.4 Equivalent Ways of Characterizing Inflation

Both the horizon problem and the flatness problem can be solved by assuming a period of decreasing Hubble radius in the early Universe. This period is called inflation and can also be characterized as either a period of accelerated expansion, slowly varying Hubble parameter or negative pressure. All of these are equivalent and can be derived from the original assumption of a decreasing Hubble radius. This also allows to recover tools to describe inflation more conveniently for the later chapters.

- Accelerated expansion: Taking the time derivative of the Hubble radius yields

$$\frac{\mathrm{d}}{\mathrm{d}t}(aH)^{-1} = \frac{\mathrm{d}}{\mathrm{d}t}\frac{1}{\dot{a}} \tag{2.23}$$

$$= -\frac{\ddot{a}}{\dot{a}^2} \tag{2.24}$$

$$= -\frac{\ddot{a}}{(aH)^2}. \tag{2.25}$$

  The condition $\frac{\mathrm{d}}{\mathrm{d}t}(aH)^{-1} < 0$ then translates into $\ddot{a} > 0$ which means that the Universe undergoes an accelerated expansion during inflation.

- Slowly varying Hubble parameter: The Hubble parameter must be slowly varying since $\frac{\mathrm{d}}{\mathrm{d}t}H = \frac{\ddot{a}}{a} - H^2$ can be rewritten as

$$\frac{\ddot{a}}{a} = H^2\left(\frac{\dot{H}}{H^2} + 1\right) \tag{2.26}$$

  which in turn can be brought to the form

$$-\frac{\ddot{a}}{(aH)^2} = \frac{1}{a}\left(\frac{\dot{H}}{H^2} + 1\right). \tag{2.27}$$

  Since the left hand side is now the time derivative of the Hubble radius, this gives the condition $-\frac{\dot{H}}{H^2} < 1$. In terms of e-folds, this can be rewritten into

$$-\frac{\dot{H}}{H^2} = -\frac{\mathrm{d}\ln H}{\mathrm{d}N} < 1, \tag{2.28}$$

  where the measure for the number of e-folds is defined as $dN = Hdt = d\ln a$.

- Negative pressure ($P < -\frac{1}{3}\rho$): Combining the first Friedmann equations (2.7) in a Universe with no or negligible curvature $H^2 = \frac{8\pi G}{3}\rho$ with the four component conservation equation 2.6 $\dot{\rho} = -3H(\rho + P)$ allows to give a condition for the pressure during inflation. By taking the time derivative of the Friedmann equation and inserting the continuity equation one obtains

$$\dot{H} = -\frac{1}{2}(\rho + P). \tag{2.29}$$

  Inserting this and equation (2.7) into expression (2.28) yields

$$\frac{3}{2}\left(1 + \frac{P}{\rho}\right) \leq 1. \tag{2.30}$$

  This can be used to find the equation of state parameter during inflation as $\omega = \frac{P}{\rho} < -\frac{1}{3}$. Since the density is always positive, this results in negative pressure during inflation.

2.5 Scalar Field Inflation

For a simple model of inflation it is sufficient to consider a scalar field ϕ, the *inflaton* and couples it to gravity as described in this action

$$S_\phi = \int \mathrm{d}^4x\sqrt{-g}\left[\frac{1}{2}g^{\mu\nu}\nabla_\mu\phi\nabla_\nu\phi - V(\phi)\right]. \tag{2.31}$$

Here g denotes the determinant of the metric $g_{\mu\nu}$ and $V(\phi)$ is a potential describing the self interaction of the inflaton field. Given this action, it is possible to find conditions for the inflaton field and its potential that allow for an accelerated expansion. To that end, the energy-momentum tensor $T_{\mu\nu}$ can be found by varying the metric by some $\delta g^{\mu\nu}$ in the expression S_ϕ. This leads to

$$T_{\mu\nu} = \nabla_\mu\phi\nabla_\nu\phi - g_{\mu\nu}\left(\frac{1}{2}g^{\alpha\beta}\nabla_\alpha\phi\nabla_\beta\phi - V(\phi)\right). \tag{2.32}$$

In the FLRW metric (2.1) spatial homogeneity was assumed. Restricting the inflaton field to also be homogeneous, which is equivalent to considering only the background field without quantum fluctuations, allows to simplify the energy-momentum tensor. Considering the time time component yields

$$T^0_0 = V(\phi) + \frac{1}{2}\dot{\phi}^2. \tag{2.33}$$

The time space components all yield $T^0_i = 0$, while the space space components give

$$T^i_j = -\delta^i_j(V(\phi) - \frac{1}{2}\dot{\phi}^2). \tag{2.34}$$

The energy-momentum tensor thus takes the form of perfect fluid with

$$\rho_\phi = \frac{1}{2}\dot{\phi}^2 + V(\phi) \tag{2.35}$$

$$P_\phi = \frac{1}{2}\dot{\phi}^2 - V(\phi). \tag{2.36}$$

This results in the equation of state parameter

$$\omega_\phi = \frac{P_\phi}{\rho_\phi} = \frac{\frac{1}{2}\dot{\phi}^2 - V(\phi)}{\frac{1}{2}\dot{\phi}^2 + V(\phi)}. \tag{2.37}$$

From the discussion on negative pressure during inflation in the previous section it is clear that $\omega_\phi < -\frac{1}{3}$ must hold to have a period of accelerated expansion. Thus, inflation happens when the potential energy dominates over the kinetic energy of the inflaton field.

The field equation of motion can be obtained by varying the action (2.31) with respect to the inflaton field. This gives

$$\frac{1}{\sqrt{-g}}\partial_\mu(\sqrt{-g}\partial^\mu\phi) + \frac{\mathrm{d}V}{\mathrm{d}\phi} = 0, \tag{2.38}$$

finding the determinant of the metric as $\sqrt{-g} = a^3$ yields

$$\partial_\mu \partial^\mu \phi + \frac{3}{a}(\partial_\mu a)(\partial^\mu \phi) + \frac{\mathrm{d}V}{\mathrm{d}\phi} = 0. \tag{2.39}$$

With a homogeneous inflaton field $\phi = \phi(t)$ this results in

$$\ddot{\phi} + 3H\dot{\phi} + \frac{\mathrm{d}V}{\mathrm{d}\phi} = 0, \tag{2.40}$$

as the equation of motion of the inflaton field. Together with the Friedmann equation

$$H^2 = \frac{1}{3}\rho = \frac{1}{3}\left(\frac{1}{2}\dot{\phi}^2 + V(\phi)\right), \tag{2.41}$$

this determines the dynamics of the scalar field and the FLRW geometry. The same result can be obtained by taking a time derivative of the first Friedmann equation and inserting the second Friedmann equation.

2.6 Slow-Roll Inflation

By considering expression (2.27) it becomes clear that inflation can only be sustained if the Hubble function varies slowly. To quantify this, the first *slow-roll parameter* is defined as

$$\epsilon \equiv -\frac{\dot{H}}{H^2}. \tag{2.42}$$

The condition for accelerated expansion can then be concisely written as $\epsilon < 1$. In terms of the inflaton field and the potential this parameter can be expressed as

$$\epsilon = 3\frac{\frac{1}{2}\dot{\phi}}{\frac{1}{2}\dot{\phi} + V(\phi)} = 3\frac{\frac{1}{2}\dot{\phi}}{\rho} = \frac{\frac{1}{2}\dot{\phi}}{H^2}. \tag{2.43}$$

The first slow-roll parameter thus remains small as long as the potential energy is much larger than the kinetic energy

$$\dot{\phi}^2 \ll V(\phi). \tag{2.44}$$

From the discussion in sections 2.2 and 2.3 it is clear that this phase of accelerated expansion needs to last long enough to solve the horizon and the flatness problem. Thus, the potential energy needs to dominate over kinetic energy during that period. This can only be true if the acceleration of the scalar field remains small. The dimensionless acceleration per Hubble time quantifies this as

$$\delta = -\frac{\ddot{\phi}}{H\dot{\phi}}. \tag{2.45}$$

By taking the time derivative of the first slow-roll parameter

$$\dot{\epsilon} = \frac{\ddot{\phi}\dot{\phi}}{H^2} - \dot{\phi}^2\frac{\dot{H}}{H^3} \tag{2.46}$$

it is possible to link the dimensionless acceleration per Hubble time δ to the second slow-roll parameter η defined by

$$\eta \equiv \frac{\dot{\epsilon}}{H\epsilon} = 2\frac{\ddot{\phi}}{H\dot{\phi}} - 2\frac{\dot{H}}{H^2} = 2(\epsilon - \delta). \tag{2.47}$$

The conditions for slow-roll inflation then read $\epsilon, |\delta| \ll 1$ or equivalently $\epsilon, |\eta| \ll 1$. These guarantee that there is a sustained period of accelerated expansion.

For small slow-roll parameters it is possible to simplify the equations of motion using the *slow-roll approximation*. In the regime where slow-roll inflation happens the potential energy dominates over the kinetic energy, see 2.43, so $V(\phi) \gg \frac{1}{2}\dot{\phi}$. This allows to approximate the first Friedmann equation (2.41) as

$$H^2 = \frac{1}{3}V(\phi). \tag{2.48}$$

The Hubble parameter during slow-roll inflation can then be completely determined by the potential energy of the inflaton field. Since it is clear from (2.28) that the Hubble parameter must vary slowly, the same must be true for the potential. Since in addition to $\epsilon \ll 1$ slow-roll inflation satisfies $|\delta| \ll 1$ which implies $\left|\ddot{\phi}\right| \ll \left|H\dot{\phi}\right|$. The equation of motion can be simplified to

$$3H\dot{\phi} = -\frac{\mathrm{d}V}{\mathrm{d}\phi}(\phi) = -V'(\phi). \tag{2.49}$$

Here and in the following, primes denote derivatives with respect to the inflaton field. It is convenient to define approximate slow-roll parameters solely based on the potential of the inflaton field as

$$\epsilon_V = \frac{M_{pl}^2}{2}\left(\frac{V'}{V}\right)^2 \tag{2.50}$$

$$\eta_V = M_{pl}^2\frac{V''}{V}. \tag{2.51}$$

The reduced Planck mass $M_{pl} = 1/\sqrt{8\pi G}$ was temporarily reintroduced to make the parameters dimensionless. Indeed, by inserting the slow-roll approximation of the equations of motion into the expressions for ϵ and η, the relations

$$\epsilon = \epsilon_V \qquad\qquad \eta = \eta_V - \epsilon_V \tag{2.52}$$

can be recovered. The parameters ϵ_V and η_V are called *potential slow-roll parameters*.

It is often useful to give a description of the amount of inflation happening before the end of inflation t_{end} as the number of e-folds N that the scale factor a grows,

$$a_{end} = ae^N. \tag{2.53}$$

In slow-roll inflation this quantity can be expressed as

$$N(\phi) = \ln \frac{a_{end}}{a} = \int_t^{t_{end}} H \mathrm{d}t = \int_\phi^{\phi_{end}} \frac{H}{\dot{\phi}} \mathrm{d}\phi \approx \int_{\phi_{end}}^{\phi} \frac{V}{V'}(\phi) \mathrm{d}\phi. \tag{2.54}$$

In terms of the slow-roll parameters this reads as

$$N(\phi) = \int_\phi^{\phi_{end}} \frac{\mathrm{d}\phi}{\sqrt{2\epsilon}} \approx \int_{\phi_{end}}^{\phi} \frac{\mathrm{d}\phi}{\sqrt{2\epsilon_V}}. \tag{2.55}$$

The total amount of e-folds during inflation can then be obtained by integrating up to the inflaton field value at the end of inflation or up to the time when inflation ends. This time or field value is characterized by $\epsilon(\phi_{end}) = 1$ since the accelerated expansion of the Universe stops at that point, see equations (2.27) and (2.25).

2.7 Reheating

In order for the expansion of the Universe to resume as postulated by the standard cosmological model, inflation needs to end. Thus, the slow-roll parameter ϵ must approach one

$$\epsilon = 3 \frac{\frac{1}{2}\dot{\phi}}{\frac{1}{2}\dot{\phi} + V(\phi)} \approx 1. \tag{2.56}$$

The potential steepens towards the end of inflation, the inflaton field picks up kinetic energy until the kinetic energy of the inflaton dominates over the potential energy.

After the end of inflation the inflaton oscillates around the minimum of its potential $V(\phi)$. At this point any entropy that the Universe had at the beginning of inflation has been inflated away, and the energy of the Universe is entirely in the oscillation of the inflaton around the minimum Riotto [2003]. Thus, during this phase the inflaton behaves like pressureless matter Baumann [2012]

$$\dot{\overline{\rho}}_\phi + 3H\overline{\rho}_\phi = 0. \tag{2.57}$$

In order for the cosmic history to resume with the hot Big Bang scenario, the low entropy Universe at the end of inflation must transform into a high entropy Universe dominated by radiation. The process transforming the energy of the inflaton field into standard model degrees of freedom is referred to as reheating. A very simple model of reheating would be for the inflaton to decay into other particles with a decay width Γ_ϕ. These particles then scatter off each other and thermalize to form

a thermal background Riotto [2003]. The average inflaton energy density can then be described by

$$\dot{\overline{\rho}}_\phi + (3H + \Gamma_\phi)\overline{\rho}_\phi = 0. \tag{2.58}$$

The inflaton energy density thus decays while producing standard model particles through the term $\Gamma_\phi \overline{\rho}_\phi$. Eventually, all the inflaton energy density is converted into standard model degrees of freedom and the hot Big Bang scenario commences Baumann [2012].

3 Cosmological Perturbations

The previous chapter dealt with the classical background evolution of the inflationary Universe. However, in order to understand many of the observations used to test inflation, e.g. the Cosmic Microwave Background (CMB), it is necessary to study the effects of quantum fluctuations around this background. This section will be the first step towards that goal, as it will give a brief introduction into cosmological perturbations and the effects the gauge choice has on them. For more exact treatments read Baumann [2012] and Mukhanov [2005].

3.1 Generalities

3.1.1 Linear Perturbations

At the time of photon decoupling observation of the CMB shows that the Universe was nearly homogeneous with homogeneities at 10^{-5} smaller than the background. It is then possible to describe all quantities of interest $X(t, \mathbf{x})$ by a homogeneous background part $\overline{X}(t)$ and a space dependent perturbation $\delta X(t, \mathbf{x})$. They then read

$$X(\mathbf{x}, t) = \overline{X}(t) + \delta X(t, \mathbf{x}). \tag{3.1}$$

Since the perturbations are small $\delta X \ll \overline{X}$, many equations can be significantly simplified by expanding only to the first order in δX.

3.1.2 Gauge Choice

While it is possible to describe all quantities as a background field and a space dependent perturbation, the choice of the background field depends on the coordinate choice. This constitutes a gauge choice. Since in inhomogeneous spacetime there is no preferred coordinate choice, the gauge choice performed to choose coordinates also fixes what constitutes the background field and the perturbation.

In order to obtain physically meaningful results, it is necessary to consider gauge independent quantities and study their perturbations, as these are invariant under coordinate changes.

3.1.3 Types of Perturbations

For a spatially flat, homogeneous and isotropic spacetime it is possible to decompose metric and stress-energy perturbations into independent scalar (S), vector (V) and

tensor (T) perturbations. This SVT-decomposition can be understood by going to Fourier space, where

$$\delta X(t, \mathbf{k}) = \int \mathrm{d}^3 x \delta X(t, \mathbf{x}) e^{-i\mathbf{k}\cdot\mathbf{x}}. \tag{3.2}$$

The Fourier modes $\delta X(t, \mathbf{k})$ evolve independently as a consequence of the translation invariance of the associated equations of motion. Thus, each Fourier mode can be studied independently.

Perturbations can be classified by considering the behavior of their Fourier modes under the rotation around $\mathbf{k}$ with an angle Ψ. A perturbation has helicity m if its amplitude is multiplied by $e^{im\Psi}$ under this rotation. Thus,

$$\delta X(t, \mathbf{k}) \to e^{im\Psi} \delta X(t, \mathbf{k}). \tag{3.3}$$

As a consequence of the rotation invariance of the background perturbations with different helicities evolve independently Baumann [2012]. Scalar, tensor and vector components are then identified by their helicities, where perturbations with helicity 0 are scalar, those with helicity ± 1 are vector and those with helicity ± 2 are tensor perturbations. With this it is possible to decompose any perturbation into scalar, vector and tensor perturbations that evolve independently. On top of that each of their Fourier modes also evolve independently.

3.2 The Inhomogeneous Universe

3.2.1 Scalar Metric Perturbations

According to Baumann [2012], the most general first order perturbation of the flat FLRW metric, made up of only helicity scalars and their derivatives, is

$$\mathrm{d}s^2 = -(1 + 2\Phi)\mathrm{d}t^2 + 2a(t)B_{,i}\mathrm{d}x^i\mathrm{d}t + a^2(t)\left[(1 - 2\Psi)\delta_{ij} + 2E_{,ij}\right]\mathrm{d}x^i\mathrm{d}x^j. \tag{3.4}$$

Here, Φ and Ψ are 3-scalars called lapse and curvature perturbation, $B_{,i}$ is a 3-vector called shift and $E_{,ij}$ is a symmetric and traceless spatial 3-tensor called shear. The comma in the subscript denotes that the quantity is a derivative with respect to the spatial coordinates following it.

Under the two scalar gauge transformations

$$t \to t + \alpha \tag{3.5}$$

$$x^i \to x^i + \delta^{ij}\beta_{,j} \tag{3.6}$$

the scalar metric perturbations transform as

$$\Phi \to \Phi - \dot{\alpha} \tag{3.7}$$

$$B \to B + a^{-1}\alpha - a\dot{\beta} \tag{3.8}$$

$$E \to E - \beta \tag{3.9}$$

$$\Psi \to \Psi + H\alpha. \tag{3.10}$$

While it is possible to modify (3.4) to also include vector and tensor perturbations, it is not useful to determine gauge invariant quantities of interest since the vector perturbations are not created by inflation and decay with the expansion of the Universe and the tensor perturbations are gauge invariant Baumann [2012].

3.2.2 Matter Perturbations

The matter perturbations, i.e. the perturbations of the density, the pressure and the momentum density and their behavior under gauge transformations may be found by considering the stress-energy tensor. It can be constructed from a density ρ, a pressure p, the 4-velocity u^μ and an anisotropic stress tensor $\Sigma^{\mu\nu}$ in the frame in which the 3-momentum density vanishes. The pressure and density perturbations may be defined by taking the background fields $\overline{\rho}$ and $\overline{p}$ to be homogeneous and defining all the inhomogeneity as perturbations $\delta\rho$ and δp. Since the 4-velocity has to satisfy $g_{\mu\nu}u^\mu u^\nu = -1$ its perturbation has only three independent components. The perturbed 4-velocity can be written as

$$u_\mu = (-1-\Phi, a v_i) \qquad\qquad u^\mu = (1-\Phi, a^{-1}(v^i - B^i)). \tag{3.11}$$

Anisotropic stress is a traceless symmetric 3-tensor and vanishes in the unperturbed Universe.

The perturbed stress energy tensor reads Baumann [2012]

$$T^0_0 = -(\overline{\rho} + \delta\rho) \tag{3.12}$$
$$T^0_i = (\overline{\rho} + \overline{p}) a v_i \tag{3.13}$$
$$T^i_0 = -(\overline{\rho} + \overline{p})(v^i - B^i)/a \tag{3.14}$$
$$T^i_j = \delta^i_j(\overline{p} + \delta p) + \Sigma^i_j. \tag{3.15}$$

The momentum density perturbation is defined as $(\delta q)_i = (\overline{\rho} + \overline{p}) v_i$. With this definition it is possible to find the effect of gauge transformations on the matter perturbations as

$$\delta\rho \to \delta\rho - \dot{\overline{\rho}}\alpha \tag{3.16}$$
$$\delta p \to \delta p - \dot{\overline{p}}\alpha \tag{3.17}$$
$$\delta q \to \delta q + (\overline{\rho} + \overline{p})\alpha. \tag{3.18}$$

Here, q is the scalar part of the 3-momentum density.

3.2.3 Gauge Invariant Variables

With the definitions of the different fluctuations and their behavior under gauge transformations above it is possible to construct gauge invariant variables by combining matter and metric perturbations. One of these is the curvature perturbation

on uniform density hypersurfaces

$$-\xi \equiv \Psi + \frac{H}{\dot{\overline{\rho}}}\delta\rho, \tag{3.19}$$

a scalar quantity which measures spatial curvature of constant density hypersurfaces. The gauge invariance of this quantity can be checked by inserting (3.16) and (3.10) into the expression.

For the remainder of this thesis matter perturbations are assumed to be adiabatic. They fulfill the condition

$$\delta p_{en} \equiv \delta p - \frac{\dot{\overline{p}}}{\dot{\overline{\rho}}}\delta\rho = 0. \tag{3.20}$$

This is typically the case for single field inflation.

The next gauge invariant quantity of interest is the comoving curvature perturbation

$$\mathcal{R} \equiv \Psi - \frac{H}{\overline{\rho} + \overline{p}}\delta q. \tag{3.21}$$

Since δq is the scalar part of the 3-momentum density T^0_i, the comoving curvature perturbations can be expressed as

$$\mathcal{R} = \Psi + \frac{H}{\dot{\overline{\Phi}}}\delta\Phi \tag{3.22}$$

during inflation.

Both curvature perturbations ξ and $\mathcal{R}$ are constant on superhorizon scale $k \ll aH$ for adiabatic matter perturbations. Here, k is the comoving wave number.

3.3 The Quantum Origins of Structure

Allowing for quantum fluctuations during inflation gives a way to generate inhomogeneities in the Universe. This can be understood as the origin of structures in the Universe. The expansion parameter H determines the scale of the fluctuations during inflation and while fluctuations are created at all length scales with a spectrum of wave number k, they only become relevant if they are inside the comoving Hubble radius at their creation. The relevant fluctuations are created on subhorizon scales $k \gg aH$. Their wave number stays constant while the comoving Hubble radius $(aH)^{-1}$ decreases during inflation. They thus exit the horizon to exist on superhorizon scales $k < aH$.

Since cosmic inhomogeneity is characterized by the intrinsic curvature of spatial hypersurfaces, the perturbations of interest are $\mathcal{R}$ and ξ. As mentioned in the previous section, these fluctuations are gauge invariant and remain constant on superhorizon scales. Their amplitudes are not affected by the physics right after

inflation. After the end of inflation the comoving Hubble radius begins to grow and the different fluctuations re-enter the horizon. This allows to probe the physics of inflation from observables such as Large Scale Structures and the Cosmic Microwave Background without detailed knowledge of the physics right after the end of inflation.

A statistical measure of the primordial fluctuations is provided by the power spectrum of $\mathcal{R}$. It can be found by taking the ensemble average over the fluctuations for different comoving wavevectors $\mathbf{k}$ and $\mathbf{k}'$

$$\langle \mathcal{R}_{\mathbf{k}} \mathcal{R}_{\mathbf{k}'} \rangle = (2\pi)^3 \delta(\mathbf{k} + \mathbf{k}') P_{\mathcal{R}}(k), \tag{3.23}$$

where the scalar power spectrum is defined as

$$\Delta_s^2 \equiv \Delta_{\mathcal{R}}^2 = \frac{k^3}{2\pi^2} P_{\mathcal{R}}(k). \tag{3.24}$$

It is often characterized by its scale dependence through the scalar spectral index

$$n_s - 1 \equiv \frac{\mathrm{d} \ln \Delta_s^2}{\mathrm{d} \ln k}. \tag{3.25}$$

Here scale invariance corresponds to $n_s = 1$ and the running of the spectral index

$$\alpha_s \equiv \frac{\mathrm{d} n_s}{\mathrm{d} \ln k}. \tag{3.26}$$

The power spectrum can then be approximated in the proximity of an arbitrary pivot scale k_* as

$$\Delta_s^2(k) = A_s(k_*) \left(\frac{k}{k_*} \right)^{n_s(k_*) - 1 + \frac{1}{2} \alpha_s(k_*) \ln\left(\frac{k}{k_*}\right)}. \tag{3.27}$$

For better approximations to the power spectrum higher order derivatives of the scalar spectral index may be considered.

The tensor power spectrum for the polarization modes of h_{ij} can be computed in a similar way as

$$\langle h_{\mathbf{k}} h_{\mathbf{k}'} \rangle = (2\pi)^3 \delta(\mathbf{k} + \mathbf{k}') P_h(k). \tag{3.28}$$

The power spectrum of the tensor perturbations is defined as the sum of the power spectra for the two polarizations

$$\Delta_t^2 \equiv 2\Delta_h^2 = 2 \frac{k^3}{2\pi^2} P_h(k). \tag{3.29}$$

Similar to the case of scalar perturbations its scale dependence can be defined as

$$n_t \equiv \frac{\mathrm{d} \ln \Delta_t^2}{\mathrm{d} \ln k}. \tag{3.30}$$

In the following chapters the power spectra of the scalar and tensor perturbations will be computed exactly.

3.4 The Mode Equation

In order to obtain an exact expression for the power spectrum, the action for single field slow-roll inflation, which reads as

$$S = \frac{1}{2}\int \mathrm{d}^4x\sqrt{-g}\left[\mathcal{R} - (\nabla\phi)^2 - 2V(\phi)\right], \tag{3.31}$$

is expanded in terms of the fluctuations $\mathcal{R}$. A convenient gauge to perform the calculation in is

$$\delta\phi = 0 \qquad g_{ij} = a^2((1-2\mathcal{R})\delta_{ij} + h_{ij}) \qquad \partial_i h_{ij} = h_{ii} = 0 \tag{3.32}$$

Maldacena [2003]. In this gauge all of the scalar degrees of freedom are parameterized by $\mathcal{R}$. This is useful, since the fluctuations $\mathcal{R}$ are constant outside the horizon which allows to restrict the calculation to times before horizon crossing. Following the calculations by Maldacena allows to expand the action to second order in the fluctuations $\mathcal{R}$. The second order perturbation of the action then reads

$$S_{(2)} = \frac{1}{2}\int \mathrm{d}^4x a^3 \frac{\dot{\phi}^2}{H^2}\left[\dot{\mathcal{R}}^2 - a^{-2}(\partial_i\mathcal{R})^2\right]. \tag{3.33}$$

Setting the variables

$$z^2 \equiv a^2\frac{\dot{\phi}^2}{H^2} \qquad u = z\mathcal{R} \tag{3.34}$$

allows to rewrite this expression into the form

$$S_{(2)} = \frac{1}{2}\int \mathrm{d}\tau\mathrm{d}^3x\left[(u')^2 + (\partial_i u)^2 + \frac{z''}{z}u^2\right]. \tag{3.35}$$

Partially integrating with respect to τ in the first term and x_i in the second allows to find the mode equation as

$$u_k'' + \left(k^2 - \frac{z''}{z}\right)u_k = 0. \tag{3.36}$$

Here, u_k are the Fourier modes of the perturbations u, obtained as

$$u(\tau,\mathbf{x}) = \int \frac{\mathrm{d}^3k}{(2\pi)^3}v_k(\tau)e^{i\mathbf{k}\cdot\mathbf{x}}. \tag{3.37}$$

3.4.1 Quantization and Boundary Conditions

In order to obtain the full time evolution of the Fourier modes of the perturbations u through the mode equation, the two initial conditions for this second order differential equation need to be found. Since the field u and with it its Fourier

components u_k are fluctuating fields, they are quantized in the following to obtain these initial conditions. Since equation (3.36) is a harmonic oscillator equation, the Fourier modes u_k can be promoted to operators $\hat{u}_k$ and then be expanded in terms of creation and annihilation operators as

$$\hat{u}_k = u_k(\tau)\hat{a}_k + v^*_{-k}\hat{a}^\dagger_{-k}. \tag{3.38}$$

Requiring that the canonical commutation relations

$$[\hat{u}_k, \hat{u}'_{\tilde{k}}] = i(2\pi)^3\hbar\delta(k-\tilde{k}) \tag{3.39}$$

and

$$[\hat{a}_k, \hat{a}^\dagger_{\tilde{k}}] = (2\pi)^3\delta(k-\tilde{k}) \tag{3.40}$$

hold fixes one of the initial conditions as

$$\frac{i}{\hbar}\left(u'_k u^*_k - u_k u'^*_k\right) = 1. \tag{3.41}$$

This can be verified by inserting the expansion (3.38) into the commutation relation (3.39) while requiring (3.40) to hold.

The second boundary condition is typically chosen as the Bunch-Davies vacuum, which corresponds to choosing a vacuum state for the fluctuations Birrell and Davies [1982]. For the rest of the thesis the boundary condition is chosen in the far past, where $t \to -\infty$ or $k \gg aH$. In this limit the mode equation (3.36) becomes the simple harmonic oscillator equation $u''_k + ku_k = 0$ Baumann [2012]. This allows to use the unique solution in the infinite past as the initial condition for the mode equation. The initial condition then reads

$$u_k(\tau \to -\infty) = \frac{e^{-ik\tau}}{\sqrt{2k}}. \tag{3.42}$$

Together with expression (3.41) this fixes the initial conditions for the mode equations. After solving the differential equation for the mode equations the scalar power spectrum can be computed as Powell and Kinney [2007]

$$\Delta_{\mathcal{R}}(k) = \frac{k^3}{2\pi^2}\left|\frac{u_k}{z}\right|^2. \tag{3.43}$$

Further computations to simulate the distribution of the observable structures in the Universe can be based on this primordial power spectrum.

3.5 Tensor Perturbations

Similarly to the scalar case the Einstein-Hilbert action can be expanded in the tensor perturbations which allows to find the second order action as Baumann [2012]

$$S_{(2)} = \frac{M^2_{pl}}{8}\int \mathrm{d}\tau \mathrm{d}^3x a^2\left[(h'_{ij})^2 - (\partial_l h_{ij})^2\right]. \tag{3.44}$$

The Fourier transformation of the tensor fluctuations read as

$$h_{ij} = \int \frac{\mathrm{d}^3 k}{(2\pi)^3} \sum_{s=+,\times} \epsilon_{ij}^s(k) h_{\mathbf{k}}^s(\tau) e^{i\mathbf{k}\cdot\mathbf{x}}. \tag{3.45}$$

Here, $+, \times$ represent the two polarization modes of the gravitational perturbations. The coefficients fulfill the relations $\epsilon_{ii} = k^i \epsilon_{ij} = 0$ and $\epsilon_{ij}^s \epsilon_{ij}^{s'} = 2\delta_{ss'}$. With this the second order action can be expressed as

$$S_{(2)} = \sum_s \frac{1}{2} \int \mathrm{d}\tau \mathrm{d}^3 k \left[(v_k^{s\prime})^2 - \left(k^2 - \frac{a''}{a} \right) (v_k^s)^2 \right]. \tag{3.46}$$

The perturbation modes v_k^s are defined as $v_k^s \equiv \frac{a}{2} M_{pl} h_k^s$. This allows to extract a differential equation for the modes of the perturbations as

$$v_k'' + \left(k^2 - \frac{a''}{a} \right) v_k = 0, \tag{3.47}$$

where the polarization indices have been omitted. This is consistent with the mode equation used in Powell and Kinney [2007]. The initial conditions can be found in the same way as for the scalar perturbations. Since the differential equation is still a harmonic oscillator equation, the first condition, reading as

$$\frac{i}{\hbar} \left(v_k' v_k^* - v_k v_k^{'*} \right) = 1, \tag{3.48}$$

holds with the same argument. Similarly to the derivation of (3.42) for $\tau \to -\infty$ the term $\frac{a''}{a} v_k^s$ also vanishes for sufficiently early conformal times Baumann [2012]. This allows to find the second initial condition as

$$v_k(\tau \to -\infty) = \frac{e^{-ik\tau}}{\sqrt{2k}}. \tag{3.49}$$

As for the scalar case, these allow to find the complete time evolution of the tensor perturbation modes. These in turn allow to find the tensor power spectrum as Powell and Kinney [2007]

$$\Delta_t^2 = \frac{32k^3}{\pi} \left| \frac{v_k}{a} \right|^2. \tag{3.50}$$

The normalization of the tensor fluctuations is typically chosen relative to the amplitude of the scalar perturbations. The tensor to scalar ratio r describes how this normalization is performed.It is defined as

$$r \equiv \frac{\Delta_t^2(k)}{\Delta_s^2(k)}. \tag{3.51}$$

4 Contact with the Observation

In the previous chapter cosmological perturbations were used to find the scalar and tensor power spectrum at any time during inflation. The different modes described through expressions (3.36) and (3.47) exit the horizon when $k = a(\tau_*)H(\tau_*)$ and then freeze retaining the value they had shortly after horizon crossing. After the end of inflation the comoving Hubble radius $(aH)^{-1}$ increases allowing the different modes to reenter the horizon. They then start to evolve again and give rise to the anisotropies in the CMB and the fluctuations in the matter power spectrum at later time. This chapter gives a short introduction into the physics and calculations involved in obtaining the CMB and Large scale structures (LSS) based on given primordial power spectra. In the analysis chapters these computations are performed with the Boltzmann code CLASS Audren et al. [2013].

The general idea this chapter will follow is that the primordial fluctuations, which are known at horizon reentry, are used to compute an observable $\mathcal{Q}$. The fluctuations and the observables time evolve after horizon reentry. The evolution is performed with a transfer function T. Schematically the observable $\mathcal{Q}$ at conformal time τ is computed from the fluctuations at horizon exit $\mathcal{R}(\tau_*)$ as

$$\mathcal{Q}_k = T_{\mathcal{Q}}(k, \tau, \tau_*)\mathcal{R}_k(\tau_*). \tag{4.1}$$

As indicated by the arguments, the transfer function may depend on the scale of the fluctuations k.

4.1 Contact with the CMB

4.1.1 Temperature Fluctuations

One of the observables in the CMB is the variation of the temperatures at specific directions in the sky $\hat{n}$ relative to the background temperature $T_0 = 2.73$ K. The harmonic expansion of the quantity $\Theta(\hat{n}) \equiv \frac{\Delta T(\hat{n})}{T_0}$ can then be used to construct an angular power spectrum. The harmonic expansion reads

$$\Theta(\hat{n}) = \sum_{\ell m} a_{\ell m} Y_{\ell m}(\hat{n}), \tag{4.2}$$

where $Y_{\ell m}$ are the spherical harmonics, and the multipole moments $a_{\ell m}$ are constructed as follows

$$a_{\ell m} = \int \mathrm{d}\Omega Y^*_{\ell m}(\hat{n})\Theta(\hat{n}). \tag{4.3}$$

These can be used to estimate the angular power spectrum as

$$C_\ell^{TT} = \frac{1}{2\ell+1} \sum_m \langle a_{\ell m}^* a_{\ell m} \rangle. \tag{4.4}$$

These equations can be used to find the angular power spectrum of the CMB based on experimental data. The most recent Planck measurement is depicted in Figure 4.1.

In order to compare the experimental data with a theory prediction, it is necessary to also compute the multipole moments and the angular power spectrum based on a predicted primordial spectrum $P_\mathcal{R}$ and a transfer function $\Delta_{T\ell}(k)$, linking the scalar modes $\mathcal{R}$ to the temperature fluctuations ΔT at the time of the CMB. According to Baumann [2012], the multipole moments can be found by

$$a_{\ell m} = 4\pi(-i)^\ell \int \frac{\mathrm{d}^3 k}{(2\pi)^3} \Delta_{T\ell}(k) \mathcal{R}_k Y_{\ell m}(\hat{k}). \tag{4.5}$$

This allows to compute the angular power spectrum according to (4.4) as

$$C_\ell^{TT} = \frac{2}{\pi} \int k^2 \mathrm{d}k P_\mathcal{R}(k) \Delta_{T\ell}(k) \Delta_{T\ell}(k). \tag{4.6}$$

The transfer functions $\Delta_{T\ell}(k)$ depend on the background cosmology and are computed numerically using CLASS.

4.1.2 Polarization

This section will give a very brief introduction to CMB polarization, for a more detailed introduction into the topic see Hu and White [1997].

The polarization of the CMB photons arises through Thompson scattering during recombination. In this process the net linear polarization of the CMB is generated, since the photons obtain a quadrupole moment during decoupling from electrons and protons Baumann et al. [2009]. The velocity field of the electrons that the CMB photons scatter off has an influence on Thompson scattering. Therefore, the anisotropies in the temperature polarization offer a way to track the primordial density perturbations and to probe inflation. In addition, this also explains why correlations between the polarization anisotropies and temperature anisotropies may arise.

Since polarization is not a scalar field, the expansion into spherical harmonics is not as straightforward as with the temperature. To get a sensible expansion, the 2×2 intensity tensor $I_{ij}(\hat{n})$ is considered, where $\hat{n}$ denotes the direction in the sky. Linear polarization can then be described by the Stokes parameters $Q = \frac{1}{4}(I_{11} - I_{22})$ and $U = \frac{1}{2} I_{12}$, temperature anisotropy is described as $T = \frac{1}{4}(I_{11} + I_{22})$. While the quantity T is invariant under rotation in the plane perpendicular to $\hat{n}$ the Stokes parameters Q and U transform under rotations by an angle ψ as a spin-2 field,

such that $(Q \pm iU)(\hat{n}) \to e^{\mp 2i\psi}(Q \pm iU)(\hat{n})$. The quantity $(Q \pm iU)(\hat{n})$ can thus be described by tensor spherical harmonics as Dodelson [2003]

$$(Q \pm iU)(\hat{n}) = \sum_{l,m} a_{\pm 2,lm} Y_{\pm 2,lm}(\hat{n}). \tag{4.7}$$

Descriptions of the tensor spherical harmonics can be found in Kamionkowski et al. [1997] and Zaldarriaga and Seljak [1997].

Instead of using the spin-2 quantities Q and U it is possible to characterize the polarization anisotropies with two scalar fields using

$$a_{E,lm} = -\frac{1}{2}(a_{2,lm} + a_{-2,lm}) \qquad a_{B,lm} = -\frac{1}{2i}(a_{2,lm} - a_{-2,lm}). \tag{4.8}$$

This results in the curl-free modes E and the divergence-free modes B defined as

$$E(\hat{n}) = \sum_{l,m} a_{E,lm} Y_{lm}(\hat{n}) \qquad B(\hat{n}) = \sum_{l,m} a_{B,lm} Y_{lm}(\hat{n}). \tag{4.9}$$

The symmetries of the temperature and the E- and B-mode anisotropies allow for the correlations TT, EE, BB and TE while, according to Baumann et al. [2009], all other correlations are zero.

Similar to the angular power spectrum for the temperature anisotropies the angular power spectra for these correlations can be defined as

$$C_\ell^{XY} \equiv \frac{1}{2\ell+1} \sum_m \langle a_{X,lm}^* a_{Y,lm} \rangle, \qquad X, Y \in \{T, E, B\}. \tag{4.10}$$

The spectra for the polarization modes are also measured by Akrami et al. [2020] and are depicted in Figure 4.1.

As with the TT angular power spectrum, the EE and TE angular power spectra can also be computed from the curvature power spectrum $P_\mathcal{R}$. They can be computed via

$$C_\ell^{EE} \approx (4\pi)^2 \int k^2 \mathrm{d}k P_\mathcal{R}(k) \Delta_{E\ell}^2(k) \tag{4.11}$$

$$C_\ell^{TE} \approx (4\pi)^2 \int k^2 \mathrm{d}k P_\mathcal{R}(k) \Delta_{T\ell}(k) \Delta_{E\ell}(k) \tag{4.12}$$

using the transfer functions $\Delta_{E\ell}$ and $\Delta_{T\ell}$. For the computations in this thesis the transfer functions are numerically found using CLASS.

The B-modes are solely generated by the tensor modes of inflation as

$$C_\ell^{BB} = (4\pi)^2 \int k^2 \mathrm{d}k P_h(k) \Delta_{B\ell}^2(k), \tag{4.13}$$

allowing to use the angular power spectrum of the B-modes as a probe for primordial tensor fluctuations.

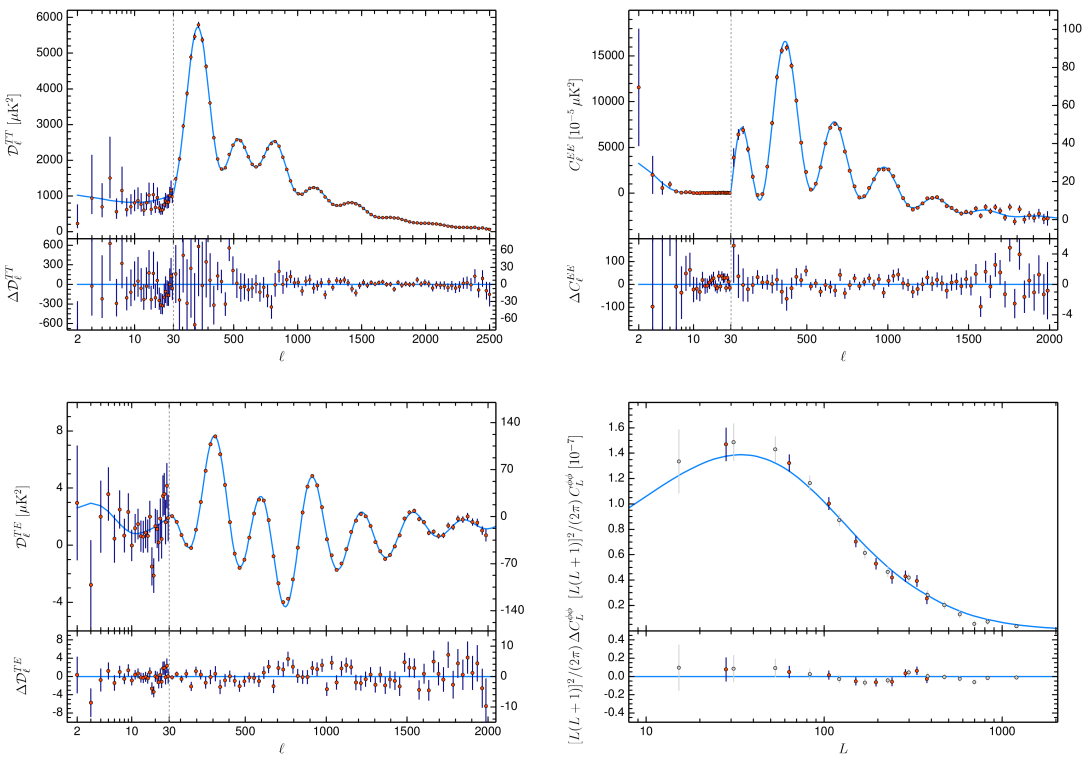

Figure 4.1: Angular power spectra as measured by the Planck experiment in 2018 Akrami et al. [2020]. The blue line represents a ΛCDM best fit, $\mathcal{D}_\ell = \ell(\ell+1)C_\ell/(2\pi)$. The lower part of the panel shows the residuals.

4.2 Contact with Large Scale Structures

While the angular power spectra found with the CMB data already provide a good way to probe inflation, it can be complemented by measuring the Large Scale Structures in the Universe. The underlying idea is that, if the evolution of the Universe is known well enough after horizon reentry of the curvature modes, the density power spectrum in the Universe can be predicted from the primordial power spectrum at the end of inflation. In this way mapping the power spectrum of the dark matter density contrast $\delta = \frac{\delta\rho}{\bar{\rho}}$ the curvature spectrum $P_\mathcal{R}$ can be probed. According to Baumann [2012], the late time density perturbation power spectrum of dark matter can be linked to the curvature spectrum right after inflation through

$$P_\delta(k,\tau) = \frac{4}{25}\left(\frac{k}{aH}\right)^4 T_\delta^2(k,\tau) P_\mathcal{R}. \tag{4.14}$$

Here, T_δ is the dark matter transport function. It can either be approximated following Eisenstein and Hu [1998] or calculated numerically with CLASS Brinckmann and Lesgourgues [2018]. Throughout this thesis, the dark matter transfer function is computed numerically.

Since the density of dark matter can only be observed through lensing, it is useful to consider quantities which can be measured by current or future experiments that allow to find clues to the distribution of the dark matter density in the Universe.

4.2.1 Galaxy Surveys

Instead of focusing on dark matter directly, it is possible to measure the density of luminous matter in the Universe instead. This can be done through galaxy surveys in the low redshift Universe. In the most simple models the galaxy distribution is linked to the dark matter density with a bias parameter b_g, such that $\delta_g = b_g \delta$ Baumann [2012]. This in turn means that the power spectra can be related by

$$P_{\delta_g} = b_g^2 P_\delta. \tag{4.15}$$

A more exact approach to linking the galaxy power spectrum to the matter power spectrum can be found in Sprenger et al. [2019]. The density power spectrum of the luminous matter in the Universe can then be computed using equations (4.14) and (4.15). In addition, it can be measured using galaxy surveys which then allows to test predictions for the primordial spectrum as well as the quantities involved in the computation of the transfer functions.

4.2.2 21cm Intensity Mapping

Instead of measuring the position of all luminous matter through mapping the galaxies in the sky, 21cm tomography aims to find the distribution of neutral hydrogen in the Universe. This is done by measuring the signal from the 21cm transition of neutral hydrogen. Depending on the intensity of the signal in different regions in the sky the density of the neutral hydrogen in that region can be found. A big advantage of this approach is that a three-dimensional map of the neutral hydrogen density can be obtained by simply varying the frequency of the survey which corresponds to varying the redshift at which one is looking for the 21cm signal. Compared to galaxy surveys 21cm tomography can probe larger redshift region as even redshifts at which stars have not yet formed can be taken into account.

For this thesis the redshift region of interest will be during the epoch of reionization, between redshifts 8 and 10. At lower redshifts reionization starts to affect the measured 21cm spectrum significantly. Similar to galaxy surveys the simplest models assume that the density of the neutral hydrogen is related to the matter power spectrum through a bias parameter b_{21} such that

$$P_{HI} = b_{21}^2 P_\delta. \tag{4.16}$$

This again allows to compare the experimental data found with 21cm intensity mapping to predictions made using a primordial spectrum and a dark matter transfer function. The approximation of the 21cm power spectrum is made more precise in section 6.4.

5 Brief Introduction to MCMC

In the previous chapter the computation of the different observable quantities that contain information on the physics of inflation is introduced. The overall goal of this thesis is to obtain constraints on some of the parameters used in this computation. Based on current or future experiments it is possible to find how likely a given power spectrum is to describe the data. Effectively, this allows to give each combination of parameters $\boldsymbol{\theta}$ a likelihood value by computing the power spectra explained in chapter 4 and then compare to the data found in experiments. The following chapter gives a short introduction into Markov chain Monte Carlo (MCMC) techniques, which allow to find constraints on each of the parameters θ^j separately. It is based on Lewis and Bridle [2002], Padilla et al. [2021] and MacKay [2003].

The probability that the model, given the set of parameters $\boldsymbol{\theta}$, describes the data is called *posterior* and is denoted as $P(\boldsymbol{\theta}|D, M)$. The probability that a given set of parameters describes the data is called *likelihood* and is denoted as $P(D|\boldsymbol{\theta}, M)$. The probability distribution which is used to sample the parameter space is called the *prior* which is denoted as $P(\boldsymbol{\theta}|M)$ and the evidence of the model is denoted as $P(D|M)$. According to Bayes theorem the posterior distribution can be described as

$$P(\boldsymbol{\theta}|D, M) = \frac{P(D|\boldsymbol{\theta}, M)P(\boldsymbol{\theta}|M)}{P(D|M)}. \tag{5.1}$$

The evidence does not depend on the parameter values and can be thought of as a normalizing factor for the posterior distribution. The overall idea of MCMC algorithms is to find a Markov chain that converges to the posterior $P(\boldsymbol{\theta}|D, M)$ by making use of randomly sampled parameter values. In order to ensure this convergence the algorithm makes use of the likelihood $P(D|\boldsymbol{\theta}, M)$, which can be computed based on the current parameter values $\boldsymbol{\theta}$ and the data found through experiment. The prior $P(\boldsymbol{\theta}|M)$ needs to be defined as a fixed distribution in the algorithm. This could be some distribution found with the results of a different experiment. For the rest of this thesis the priors are uniformly distributed, in this way it effectively only modifies the posterior as a normalizing factor. If the distribution of the points in the Markov chain follows the posterior distribution, the normalizing factor can be found by summing over all Markov chain points. This allows to approximate the posterior distribution as long as the Markov chain converges to it.

In the course of this thesis this is ensured by using the Metropolis-Hastings algorithm Metropolis et al. [1953], Hastings [1970]. The starting point for this algorithm is a random initial point $\boldsymbol{\theta}_i$ with an associated, as of yet not normalized, posterior distribution $P^*(\boldsymbol{\theta}_i)$. Based on this point a new position in the parameter space $\boldsymbol{\theta}_c$

is chosen according to an arbitrary proposal distribution $q(\boldsymbol{\theta}_i, \boldsymbol{\theta}_c)$ which generates a random next step. This proposed new position is accepted with a probability

$$\alpha(\boldsymbol{\theta}_i, \boldsymbol{\theta}_c) = \min\left\{1, \frac{P(\boldsymbol{\theta}_c)q(\boldsymbol{\theta}_i, \boldsymbol{\theta}_c)}{P(\boldsymbol{\theta}_i)q(\boldsymbol{\theta}_c, \boldsymbol{\theta}_i)}\right\}, \tag{5.2}$$

where $P(\boldsymbol{\theta})$ denotes the normalized posterior distribution. The transition probability to go from $\boldsymbol{\theta}_i$ to $\boldsymbol{\theta}_c$ is then $T(\boldsymbol{\theta}_i, \boldsymbol{\theta}_c) = \alpha(\boldsymbol{\theta}_i, \boldsymbol{\theta}_c)q(\boldsymbol{\theta}_i, \boldsymbol{\theta}_c)$ this ensures that the condition

$$P(\boldsymbol{\theta}_c)T(\boldsymbol{\theta}_c, \boldsymbol{\theta}_i) = \min\{P(\boldsymbol{\theta}_i)q(\boldsymbol{\theta}_c, \boldsymbol{\theta}_i), P(\boldsymbol{\theta}_c)q(\boldsymbol{\theta}_i, \boldsymbol{\theta}_c)\} = P(\boldsymbol{\theta}_i)T(\boldsymbol{\theta}_i, \boldsymbol{\theta}_c) \tag{5.3}$$

holds. With this detailed balance condition fulfilled, the stationary distribution of the Markov chain is $P(\boldsymbol{\theta})$, after performing a large enough number of steps the points in the Markov chain will be distributed according it Lewis and Bridle [2002]. Written concisely the steps in the algorithm are Padilla et al. [2021]:

1. Choose initial point $\boldsymbol{\theta}_i$ and compute posterior distribution
2. Generate new candidate $\boldsymbol{\theta}_c$ using the proposal distribution $q(\boldsymbol{\theta}_{c-1}, \boldsymbol{\theta}_c)$ and compute its posterior distribution
3. Accept or reject the point according to the acceptance rate α
4. If the point is not accepted, repeat the previous point in the chain
5. Repeat steps 2-3 until the chain has the desired length.

For a random initial point $\boldsymbol{\theta}_i$ the Markov chain will take a number of steps to equilibrate before it starts sampling from the posterior distribution. This part of the chain is referred to as burn in and is removed before analyzing the rest of the chain. This method allows to sample from a multidimensional probability distribution to obtain a large number of points from this distribution. In order to derive mean values and confidence regions for a single parameter $(\theta^j)_{j=1,2,\ldots,N}$ the marginalized one-dimensional distributions can be found by counting the number of samples within binned ranges of parameter values. Based on the binned one-dimensional distributions the mean values of the parameters as well as the limits for 68% and 95% confidence regions can be found. For this thesis the Markov chain Monte Carlo is performed using the Metropolis-Hastings method implemented in MontePython, for more specific information on the computation and algorithm see Brinckmann and Lesgourgues [2018]. The analysis of the Markov chains is performed with GetDist, for more precise information on the computations performed to obtain contours and confidence limits see Lewis [2019].

6 Numerical Analysis

In the previous chapters the underlying physical theory and the basic framework of a Monte Carlo Markov chain where introduced. This chapter will give a summary of which tools are used to perform the analysis of the Planck 2018 data and subsequently the simulated data of the Square Kilometer Array.

The overall structure of the computation is similar regardless of which specific packages are used. In a first step, a set of parameters are generated by a Monte Carlo Markov chain code. For the purpose of this thesis the code used is MontePython Brinckmann and Lesgourgues [2018]. This set of parameters is then given to a Boltzmann code which computes a primordial spectrum from some of these parameters. Following this the code time evolves this spectrum up to the redshift of interest. The time evolution may also depend on the parameters generated by the Markov chain code. In this thesis the time evolution of the spectrum is performed by the Boltzmann code CLASS Blas et al. [2011]. Inflation, and in particular the generation of the primordial spectrum is treated separately and more in-depth than the time evolution using the transfer functions described in chapter 4. CLASS itself also treats the generation of the primordial spectrum in a separate module which allows to use a custom code to compute the primordial spectrum separately or set different ways to compute the primordial power spectrum. In the later analysis the computation described in Lesgourgues et al. [2008] is used to construct the primordial power spectrum based on a model independent approximation of the Hubble function.

6.1 Primordial Power Spectra

The power spectrum of the curvature perturbation at the end of inflation is the seed of structure formation in our analysis. This primordial power spectrum can be used as an input for CLASS which computes the CMB spectra and the matter power spectrum at all relevant redshifts z. There are several different ways to approximate the primordial power spectrum, a selection of which are presented in the following.

6.1.1 Spectral Index and its Runnings

The primordial power spectrum around some reference scale k_* can be approximated using a power series expansion in $\ln\left(\frac{k}{k_*}\right)$, where k is the comoving wave number. Up to second order the expression is given in (3.27). To better model the primordial

power spectrum, the following third order expression is used

$$\Delta^2_{\mathrm{har}} = A_s \exp\left(\left[(n_s - 1)\ln\left(\frac{k}{k_*}\right) + \frac{\alpha}{2}\left(\ln\left(\frac{k}{k_*}\right)\right)^2 + \frac{\beta}{6}\left(\ln\left(\frac{k}{k_*}\right)\right)^3\right]\right). \quad (6.1)$$

For the remainder of this thesis the reference scale is chosen as $k_* = 0.05(\mathrm{Mpc})^{-1}$ to match the choice in Akrami et al. [2020]. The spectral index n_s and its running α are defined in (3.25) and (3.26), respectively. The running of the running β is defined in similar way as

$$\beta \equiv \frac{\mathrm{d}\alpha}{\mathrm{d}\ln k}. \quad (6.2)$$

Choosing values of the spectral index evaluated at the pivot scale different from one as well as parameters α and β different from zero allows to depart from the scale invariant Harrison-Zel'dovich spectrum. This is clearly visible in Figure 6.1 where the primordial power spectrum is computed with equation (6.1) and the Planck 2018 mean values for n_s, α and β for subsequent orders in the perturbation series. In this figure the primordial power spectrum is plotted in logarithmic comoving wave number k. Assuming $n_s \neq 1$ allows to introduce a slope into the power spectrum. The parameter α allows to bend it into a parabolic shape in logarithmic wave number, while β allows the power spectrum to take the shape of a third order polynomial.

Performing the whole analysis with this approach to the primordial power spectrum allows to approximate the curvature power spectrum right after inflation, the angular power spectra at the time of recombination and the Large Scale Structures in the Universe. However, it does not directly encode any information on the inflaton field or the shape of its potential. The information is instead encoded in the logarithmic derivatives of the primordial spectrum. For a given inflationary model these have to be calculated separately.

6.1.2 Integration of the Mode Equation

The approaches described in the previous section relies on the approximation of the primordial power spectrum using expression (6.1). Instead, the primordial power spectrum can be computed by the mode equation (3.36). In the approach described below this is done in a model independent way by approximating the Hubble function during and right after inflation with a Taylor series in the inflaton field value. The parameters sampled by the MCMC algorithm can be used to directly compute the Taylor series coefficients at horizon crossing of the pivot scale. This essentially allows to constrain the Hubble function during inflation. The formalism described below is already implemented in CLASS and authored by Lesgourgues et al. [2008].

For inflation driven by a single scalar field ϕ with a potential $V(\phi)$ in a spatially flat FLRW Universe the background evolution of the Universe can be described by

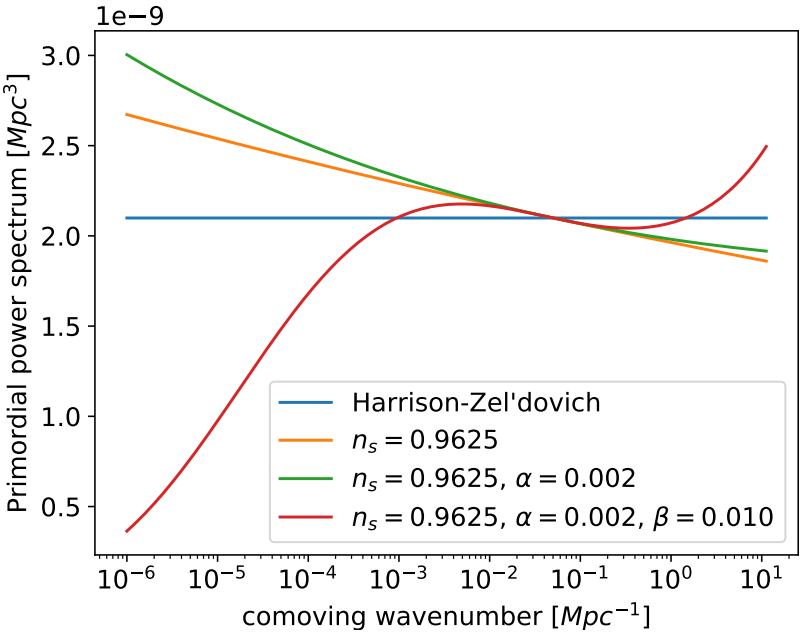

Figure 6.1: Approximated primordial power spectrum allowing for different order in the power series expansion. The spectral index and its runnings are chosen according to the mean values in Akrami et al. [2020]

Salopek and Bond [1990]

$$\dot{\phi} = -\frac{M_{pl}^2}{4\pi} H'(\phi) \tag{6.3}$$

$$-\frac{32\pi^3}{M_{pl}^4} V(\phi) = [H'(\phi)]^2 - \frac{12\pi}{M_{pl}^2} H^2(\phi). \tag{6.4}$$

Here the primes denote derivatives with respect to the field ϕ, while dots denote derivatives with respect to cosmic time. The value ϕ_* denotes the field value at horizon crossing of the pivot scale k_*. In order to acquire a set of model independent parameters the Hubble function $H(\phi - \phi_*)$ is expanded as a Taylor series in the field $\phi - \phi_*$. For the analysis with this method the Hubble function simply reads

$$H(\phi) = \sum_{n=0}^{N} \frac{1}{n!} \frac{\mathrm{d}^n H}{\mathrm{d}\phi^n}\bigg|_{\phi_*} (\phi - \phi_*)^n, \tag{6.5}$$

where the subscript star means evaluated at the field value ϕ_* at the pivot scale. To avoid parameter degeneracies the Hubble slow-roll parameters are used instead of the coefficients in the Taylor series Lesgourgues et al. [2008]. To that end the first

four Hubble slow-roll parameters are defined as

$$\epsilon_H = 2M_{pl}^2 \left(\frac{H'_*}{H_*}\right)^2 \tag{6.6}$$

$$\eta_H = 2M_{pl}^2 \frac{H''_*}{H_*} \tag{6.7}$$

$$\xi_H^2 = (2M_{pl}^2)^2 \frac{H'_* H_*^{(3)}}{H_*^2} \tag{6.8}$$

$$\omega_H^3 = (2M_{pl}^2)^3 \frac{(H'_*)^2 H_*^{(4)}}{H_*^3}. \tag{6.9}$$

These are then sampled over in the MCMC algorithm. In addition a 0th slow-roll parameter is defined as

$$\tilde{A}_s = \frac{4H_*^4}{(8\pi)^3 (H'_*)^2 M_{pl}^6}. \tag{6.10}$$

However, in the computation the slow-roll parameters are used to compute the Taylor series coefficients as

$$H_* = \sqrt{\tilde{A}_s \epsilon_H \pi} \tag{6.11}$$

$$H'_* = -\sqrt{4\pi\epsilon_H} H_* \tag{6.12}$$

$$H''_* = 4\pi\eta_H H_* \tag{6.13}$$

$$H_*^{(3)} = (4\pi)^2 \xi_H^2 \frac{H_*^2}{H'_*} \tag{6.14}$$

$$H_*^{(4)} = (4\pi)^3 \omega_H^3 \frac{H_*^3}{(H'_*)^2}. \tag{6.15}$$

These in turn are then inserted into (6.5) to obtain the Hubble function. As a consistency check the Hubble function can then be inserted into (6.4) to reconstruct the potential. This is illustrated in Figure 6.2.

For each set of parameters a period of slow-roll can be identified for small deviations of the inflaton field values ϕ from the reference value ϕ_*. The regime of slow-roll is then followed by a period during which the potential falls steeply, this is expected if slow-roll breaks down and inflation ends. The field values at which this breakdown happens varies for the different sets of parameters. In combination with equation (6.3) this can be seen as inflation lasting for a different amount of time. The amount of inflation happening and the time it takes is not restricted in this general scenario.

The background evolution of the inflaton field can be found by integrating equation (6.3) numerically after inserting the approximation for the Hubble function. The field ϕ can then in turn be used to integrate the mode equation for the scalar

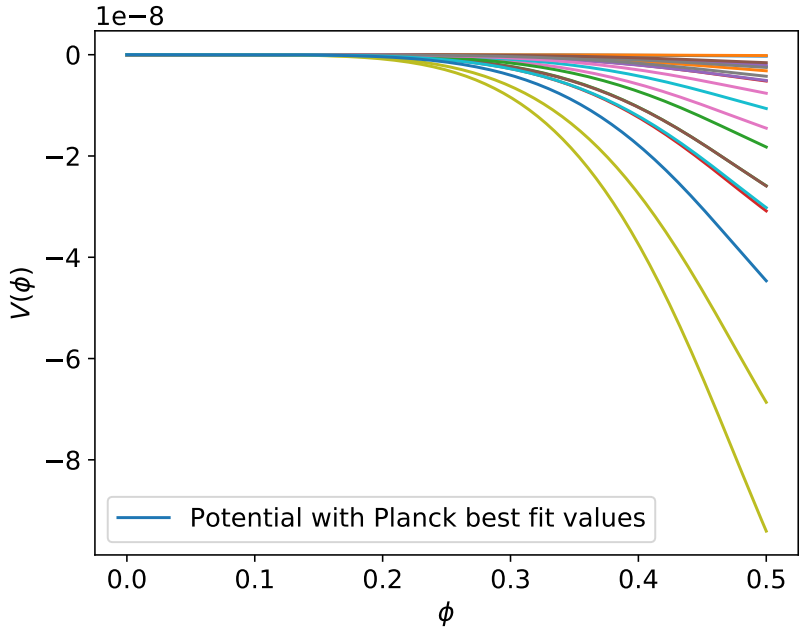

Figure 6.2: Inflaton potentials reconstructed from elements of a Monte Carlo Markov chain used to constrain Planck

perturbations as well as the tensor perturbations. These read

$$\frac{\mathrm{d}^2 u_k^{S,T}}{\mathrm{d}\tau^2} + \left(k^2 - \frac{1}{z^{S,T}}\frac{\mathrm{d}^2 z^{S,T}}{\mathrm{d}\tau^2}\right) u_k^{S,T} = 0, \tag{6.16}$$

where $z^S = a\frac{\dot{\phi}}{H}$ for the scalar modes and $z^T = a$ for the tensor modes. The initial condition for the integration is taken to be the Bunch-Davies vacuum

$$u_k^{S,T} = \frac{e^{-ik\tau}}{\sqrt{2k}} \tag{6.17}$$

$$\frac{\mathrm{d}u_k^{S,T}}{\mathrm{d}\tau} = \frac{-ike^{-ik\tau}}{\sqrt{2k}}, \tag{6.18}$$

at the time when $\frac{k}{aH} = 50$. The integration stops when the scalar and tensor power spectra freeze out for long wavelengths. The power spectra are then computed as

$$\mathcal{P}_\mathcal{R}(k) = \frac{k^3}{2\pi^2}\left|\frac{u_k^S}{z^S}\right|^2 \tag{6.19}$$

$$\mathcal{P}_h(k) = \frac{32k^3}{\pi m_{pl}^2}\left|\frac{u_k^T}{z^T}\right|^2. \tag{6.20}$$

Based on the Hubble slow-roll parameters it is possible to compute the spectral runnings of the spectral index following the formalism in Stewart and Lyth [1993b].

The exact formula to derive the scalar index up to second order in the Hubble slow-roll parameters is given in Powell and Kinney [2007]. By making use of the e-folds evolution of the Hubble slow-roll parameters a conversion formula from the Hubble slow-roll parameters to the spectral index n_s, its running α and the running of its running β can be found. Up to second order in the slow-roll parameters the conversion formula reads as

$$n_s = 1 + 2\eta_H - 4\epsilon_H - \frac{1}{2}(3 - 5C)\eta_H\epsilon_H + \frac{1}{2}(3 - C)\xi_H^2 \tag{6.21}$$

$$\begin{aligned}\alpha = &-2\xi_H^2 - \frac{1}{2}(3 - C)\omega_H^3 + 10\epsilon_H\eta_H - 8\epsilon_H^2 - \frac{1}{2}(1 + 5C)\epsilon_H\xi_H^2 \\ &- \frac{1}{4}(3 - C)(2\eta_H - 4\epsilon_H)\xi_H^2 - \frac{1}{2}(3 - C)\epsilon_H\omega_H^3\end{aligned} \tag{6.22}$$

$$\begin{aligned}\beta = &\, 2\omega_H^3 + 2\epsilon_H\omega_H^3 + 2\eta_H\xi_H^2 - 14\epsilon_H\xi_H^2 + \frac{1}{2}(1 + 5C)\epsilon_H\omega_H^3 \\ &+ \frac{1}{4}(3 - C)(\xi_H^2)^2 + \frac{3}{2}(3 - C)\eta_H\omega_H^3 - \frac{5}{2}(3 - C)\epsilon_H\omega_H^3,\end{aligned} \tag{6.23}$$

where $C = 4(\ln(2) + \gamma_e) - 5$ and $\gamma_e \approx 0.577$. Figures 6.3 and 6.4 illustrates how closely this approach approximates a power spectrum computed through direct integration using the Hubble slow-roll parameters. For the purpose of illustration the approximation is first done using only the spectral index and then adding the two runnings with the values found in Akrami et al. [2020] step by step.

In addition to the Hubble slow-roll parameters described above, it is possible to define potential slow-roll parameters that approximate the inflaton potential. They can be defined as Kohri et al. [2013]

$$\epsilon_V = \frac{1}{2}M_{pl}^2\left(\frac{V'}{V}\right)^2 \tag{6.24}$$

$$\eta_V = M_{pl}^2\frac{V''}{V} \tag{6.25}$$

$$\xi_V^2 = M_{pl}^4\frac{V'V'''}{V^2} \tag{6.26}$$

$$\omega_V^3 = M_{pl}^6\frac{(V')^2V^{(4)}}{V^3}. \tag{6.27}$$

Following the discussion in Stewart and Lyth [1993a], Stewart and Gong [2001] and Leach et al. [2002] then allows to find approximate expressions for the scalar spectral index n_s and the running of the spectral index α. In Kohri et al. [2013] these expressions in addition to the running of the running of the scalar index, β,

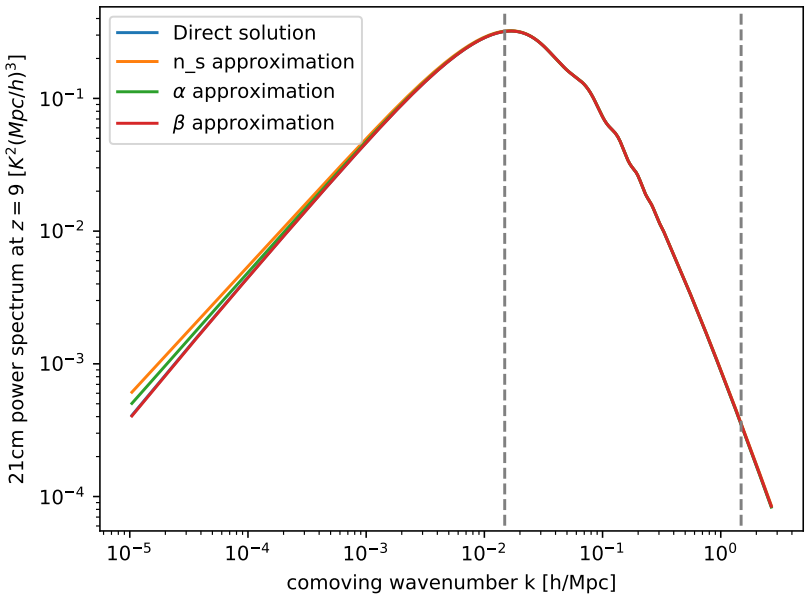

Figure 6.3: Simulated 21cm power spectrum according to section 6.4. The primordial spectrum is constructed using equation (6.1), the evolution until redshift 9 is performed by CLASS.

are given as

$$n_s - 1 = 6\epsilon_V + 2\eta_V + \left(-\frac{10}{3} + 24C\right)\epsilon_V^2 + \frac{2}{3}\eta_V^2 - (2 + 16C)\epsilon_V\eta_V + \left(\frac{2}{3} + 2C\right)\xi_V^2 \tag{6.28}$$

$$\alpha = -24\epsilon_V^2 + 16\epsilon_V\eta_V - 2\xi_V^2 \tag{6.29}$$

$$\beta = -192\epsilon_V^3 + 192\epsilon_V^2\eta_V - 32\epsilon_V\eta_V^2 + (-24\epsilon_V + 2\eta_V)\xi_V^2 + 2\omega_V^3. \tag{6.30}$$

In some of the previous work on constraining inflation with the Square Kilometer Array the Hubble or potential slow-roll parameters are used to approximate the spectral index and its runnings Barger et al. [2009a], Kohri et al. [2013], Pourtsidou [2016]. They can then be used to compute the primordial power spectrum using expression (6.1).

6.2 CLASS

Once the computation of the primordial power spectrum is done, either through the code described in Lesgourgues et al. [2008] or through an approximation following equation (6.1), the power spectrum needs to be time evolved up to the redshift it

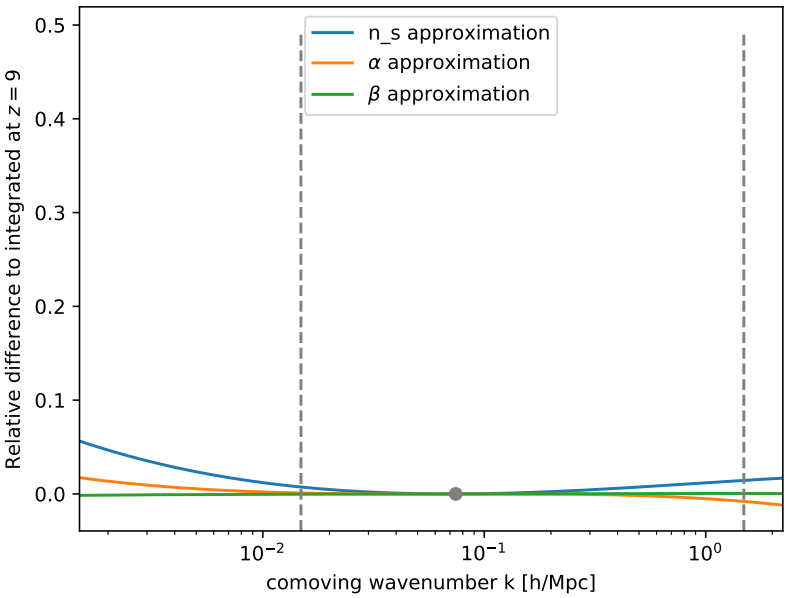

Figure 6.4: Relative difference of the approximations to the direct solution. The primordial spectrum is constructed using equation (6.1), the evolution until redshift 9 is performed by CLASS. The grey dot marks the position of the pivot scale.

is measured at. This is done using the Boltzmann code CLASS Blas et al. [2011]. In the context of this thesis the power spectrum is compared to simulated or real data at two different redshifts. The power spectrum and the angular spectra for the computations involving the Cosmic Microwave Background need to be computed at redshift $z \approx 1100$. To include secondary effects on the temperature anisotropies, the different spectra then need to be evolved up to present time at redshift zero. The simulated measurement with the SKA is performed at present time but considers a signal originating between redshift $z = 8$ and $z = 10$. In the code used to compute the spectrum secondary effects on the 21cm photons emitted in the hydrogen transition are considered only as noise. The power spectrum for this analysis is thus only computed until the redshifts mentioned above.

CLASS has a wide range of capabilities, including the ability to compute the power spectrum at any redshift needed and for many different sets of parameters, describing not only the standard cosmological model but also effects due to the inclusion of the slow-roll parameters mentioned above, massive neutrinos and different reionization histories. All computations are performed fast enough for the result to be used by a MCMC code to perform parameter estimation in reasonable time scales.

6.3 MontePython

The Markov chain Monte Carlo code used in the analysis part of this thesis is MontePython Brinckmann and Lesgourgues [2018]. It samples a set of parameters and computes how likely this combination of parameters is to describe a given set of data. The computation of the likelihood is in the case of the CMB observables performed by the likelihood code used in Akrami et al. [2020]. For the SKA the computation of the likelihoods is performed as described in section 6.4. Here the preexisting likelihood class in MontePython was used. In addition MontePython also has a built in plotting script that allows to visualize the results of a given MCMC run, however, for the all of the plots in this thesis the external plotting script GetDist Lewis [2019] was used.

6.4 SKA Likelihood

Since no real data has been collected by the SKA as of today the likelihoods needed to run a MCMC algorithm are generated by computing a 21cm power spectrum based on the Planck 2018 results and by modeling the noise entering in a future measurement. These likelihoods are then used to find how the SKA would constrain single field inflation. This project focuses on the epoch of reionization and redshifts of about $z \approx 8$ to $z \approx 10$. The upper redshift bound is chosen to avoid the position dependence of the spin temperature, since the spin temperature couples to the gas temperature due to the Wouthuysen-Field Effect at this redshift range Mao et al. [2008]. The lower redshift bound is chosen such that no position dependent reionization fraction has to be introduced as there still is nearly no reionized helium.

The SKA likelihood is computed based on the 21cm power spectrum defined as the two-point correlation

$$\langle \Delta T_{21}(\mathbf{k}) \Delta T_{21}(\mathbf{k}') \rangle \equiv P_{21}(\mathbf{k}, z)(2\pi)^3 \delta(\mathbf{k} - \mathbf{k}'), \tag{6.31}$$

where $\Delta T_{21}(\mathbf{k})$ is the Fourier transformation of the difference between the 21cm temperature $T_{21}(\mathbf{x})$ and the average 21cm temperature $\overline{T}_{21}(\mathbf{z})$.

According to Muñoz et al. [2017] the 21cm power spectrum can be computed as

$$P_{21}(\mathbf{k}) = \left[\mathcal{A}(z) + \overline{T}_{21}(z)\mu^2\right]^2 P_{\mathrm{HI}}(k). \tag{6.32}$$

The parameter $\mu \equiv \frac{k_\parallel}{k}$ is the cosine between the line of sight $k_\parallel$ and the absolute value k. Since the redshift region was chosen to ensure that the data obtained is from before reionization started, the neutral hydrogen fraction is $\overline{x}_H = 1$. This allows to set the power spectrum of the neutral hydrogen perturbations $P_{\mathrm{HI}}(k)$ to equal the matter power spectrum $P_\delta(k)$. Before the beginning of reionization the function $\mathcal{A}(z)$ and the average temperature at a specific redshift can be approximated as

Muñoz et al. [2017]

$$\mathcal{A}(z) = \overline{T}_{21}(z) = 27.3\text{mK} \times \overline{x}_{\text{H}} \frac{T_s - T_\gamma}{T_s} \left(\frac{1+z}{10}\right)^{1/2}. \tag{6.33}$$

This form of $\mathcal{A}(z)$ can be assumed before the beginning of reionization only, since during reionization the ionization power spectrum and the density-ionization power spectrum from Mao et al. [2008] have a significant impact. During the epoch of reionization the spin temperature can be taken to be much larger than the photon temperature due to the Wouthuysen-Field Effect. The gas temperature in the intergalactic medium is heated by X-ray photons up to hundreds of Kelvin Mao et al. [2008]. This allows to drop the temperature factor, which reduces the previous expression to

$$\mathcal{A}(z) = \overline{T}_{21}(z) = 27.3\text{mK} \times \overline{x}_{\text{H}} \left(\frac{1+z}{10}\right)^{1/2}. \tag{6.34}$$

The instrumental noise power spectrum in Fourier space for an antenna array with baseline D_{base}, uniformly covered up to a fraction f_{cover} with an observation time t_o can be expressed as Tegmark and Zaldarriaga [2009]

$$P_{21}^N = \frac{\pi T_{\text{sys}}^2}{t_o f_{\text{cover}}^2} d_A^2(z) y_\nu(z) \frac{\lambda^2(z)}{D_{\text{base}}^2} \tag{6.35}$$

where $\lambda(z)$ is the 21cm-transition wavelength at redshift z. The conversion function from frequency ν to line of sight $k_\parallel$ is $y_\nu = 18.5 \left(\frac{1+z}{10}\right) \frac{\text{Mpc}}{MHz}$ while the system temperature can be parameterized as Muñoz et al. [2017]

$$T_{\text{sys}} = 180\text{K} \times \left(\frac{\nu}{180\text{MHz}}\right)^{-2.6}. \tag{6.36}$$

Here, the frequency is the 21cm transition at redshift z, $\nu = \frac{\nu_0}{1+z}$. The observation time is chosen as $t_o = 10000h$, while the baseline $D_{base} = 1\text{km}$ is taken to be the baseline as specified for SKA-LOW in Bacon et al. [2020]. The coverage fraction in the nucleus of the antenna array can be computed as Tegmark and Zaldarriaga [2009]

$$f_{cover} = N_a \frac{D^2}{D_{base}^2}, \tag{6.37}$$

where N_a is the number of antennas while D is their diameter. For the values given for SKA-LOW in Bacon et al. [2020] the coverage fraction can be computed to be approximately $f_{cover} \approx 0.0091$. The following plot 6.5 contains the 21 cm spectra computed from a MCMC run used to compute the Hubble slow-roll parameters for the Planck reproduction. Both the noise described in (6.35) and the minimal and maximal wave numbers have to be taken into account in the computation of the SKA

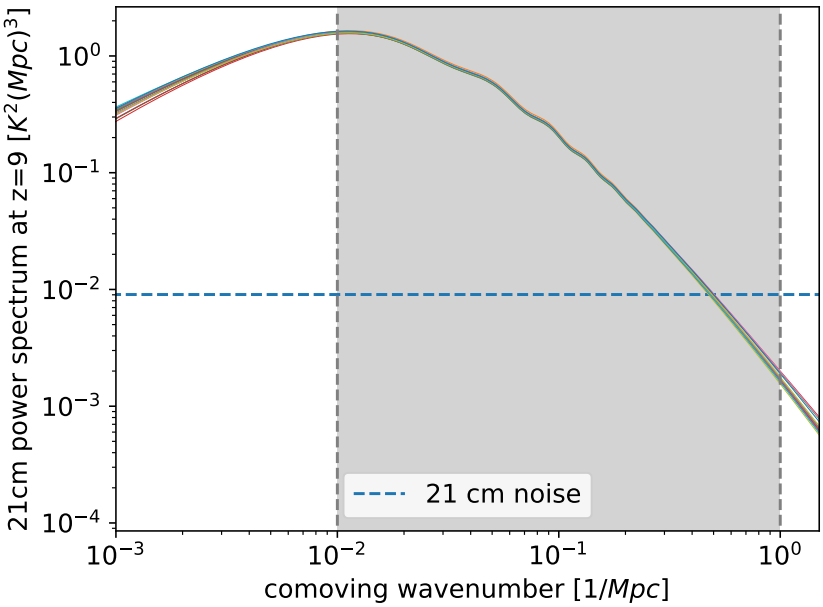

Figure 6.5: Comparison between 21cm power spectrum and the noise power spectrum computed through (6.35). The grey lines denote the maximal and minimal scales considered.

likelihood. The signal to noise ratio is approximately 100 at the peak of the 21cm power spectrum. Note that the units used in this plot are Mpc and not Mpc/h since the implementation is meant to work with CLASS which uses these units internally.

In order to construct a likelihood based on the 21cm power spectrum computed through expression (6.32) and the noise power spectrum in equation (6.35), a redshift and comoving wave number region have to be chosen. In principle, the χ^2 value is then found by computing the χ^2 value for each redshift and comoving wave number and then integrating over both quantities. The redshift integration is approximated by defining a set of redshift bins in which each of the quantities are set to be constant. The contribution of each of the redshift bins is then computed separately and added up to give the overall χ^2. In the analysis section the number of equally spaced redshift bins in the region $z \in [8, 10]$ is set to 22.

The comoving wave numbers that can be used in this analysis during the epoch of reionization are bounded from above by the non-linear scale which will be set as $k_{NL} = 1\text{Mpc}^{-1}$ for consistency with Muñoz et al. [2017]. Astrophysical foregrounds will cut off line-of-sight wave numbers smaller than

$$k_{\parallel}^{min} \approx \frac{2\pi}{y_\nu \Delta\nu}. \tag{6.38}$$

Here, $\Delta\nu$ is the bandwidth probed by SKA. According to Muñoz et al. [2017], the likelihoods do not depend sensitively on this cutoff, thus the minimal value for the

wave number is fixed to $k_{\parallel}^{min} = k_{\perp}^{min} = k^{min} = 10^{-2}\text{Mpc}^{-1}$.

For a specific redshift bin centered at z_i the computation of the χ^2 value is based on the Fisher matrix computation in Muñoz et al. [2017] and reads

$$\chi_i^2 = \frac{f_{sky}}{2}\frac{Vol_i}{(2\pi)^3}\int_{k_{min}}^{k_{max}} \mathrm{d}k(2\pi k^2)\int_{-1}^{1}\mathrm{d}\mu\frac{[P_{21}(\mathbf{k},z,\theta) - P_{21}^{fid}(\mathbf{k},z,\theta_{fid})]^2}{[P_{21}(\mathbf{k},z,\theta) + P_{21}^{N}(z)]^2}. \tag{6.39}$$

In the formula above the subscripts i denote the redshift bin. The comoving volume of the redshift bin Vol_i can be computed as a spherical shell in comoving distance $r(z_i)$ and $r(z_{i-1})$, where z_i and z_{i-1} are the edges of the redshift bin of interest. The expression to compute the volume reads as

$$Vol_i = \frac{4}{3}\pi\left(r(z_i)^3 - r(z_{i-1})^3\right). \tag{6.40}$$

All of the different χ_i^2 at different redshifts are finally summed up to give the overall χ^2 as

$$\chi^2 = \sum_i \chi_i^2. \tag{6.41}$$

The fiducial power spectrum $P_{21}^{fid}(\mathbf{k},z,\theta_{fid})$ is computed according to (6.32) and f_{sky} is set to 0.58 according to Sprenger et al. [2019]. The parameters θ are used to compute the matter power spectrum. In the earlier chapters the examples $\theta = \{\tilde{A}_s, \epsilon, \eta, \xi, \omega\}$ and $\theta = \{A_s, n_s, \alpha, \beta\}$ are discussed in expressions (3.36) and (6.1), respectively. For the computation of the fiducial power spectrum the mean values for these parameters based on only the Planck mean values are chosen.

7 Comparison to Planck Results

In order to verify that the methods, the code and the parameters chosen are sensible the Markov chain Monte Carlo code MontePython Brinckmann and Lesgourgues [2018], Audren et al. [2013] is used to compute contours for the ΛCDM parameters. In addition the spectral index and its runnings n_s, α and β using the parametrization described in expression (6.1) are used to constrain inflation. For all of these parameters the Planck 2018 paper on inflation Akrami et al. [2020] finds limits and contours as well. Finally, a parameter estimation of the Hubble slow-roll parameters is performed using the formalism in Lesgourgues et al. [2008]. This result can also be compared to the results in Akrami et al. [2020]. The same formalism will later be used to find constraints on the slow-roll parameters which might result from the Square Kilometer Array. MontePython computes likelihoods for different parameter sets by first drawing a set of parameters at random, based on the previous position of the chain. It then computes a matter power spectrum and the angular power spectra for the CMB using the Boltzmann code CLASS Blas et al. [2011]. The CMB spectra are then compared to the Planck data, and the likelihood for each of them is computed. Based on this likelihood the proposed step is either assumed or rejected as described in chapter 5. This allows to sample the likelihood in a multi-dimensional parameter space.

7.1 ΛCDM Contours

In a first step, the parameter estimation for the ΛCDM parameters only is performed. The parameters depicted in figure 7.2 are chosen to match the parameters of Figure 7.1 which is taken from Akrami et al. [2020]. The derived parameters as well as the parameter θ_{MC} which differs between MontePython and CosmoMC were removed.

Figure 7.2 depicts the marginalized contours obtained by performing 100000 steps on 16 chains in parallel. The Monte Carlo Markov chain engine is run twice. The first run, performed without a covariance matrix, suffers from a relatively low acceptance rate. For the second run the covariance matrix generated in the first run is used to obtain a better proposal distribution, resulting in a higher rate of accepted steps. Once the Markov chains have been computed, the analysis code GetDist Lewis [2019] is used to plot the marginalized contours and find the 95% confidence regions.

For the generation of these contours the TT, TE and EE likelihoods in addition to the EE likelihood at low multipoles and the TT likelihood at high multipoles were used. The best fit values and confidence limits for these parameters are summarized in Table 7.1. Comparing the values to Table 2 in Akrami et al. [2020] allows to find that both the mean values and the error bars of this analysis are very similar to those

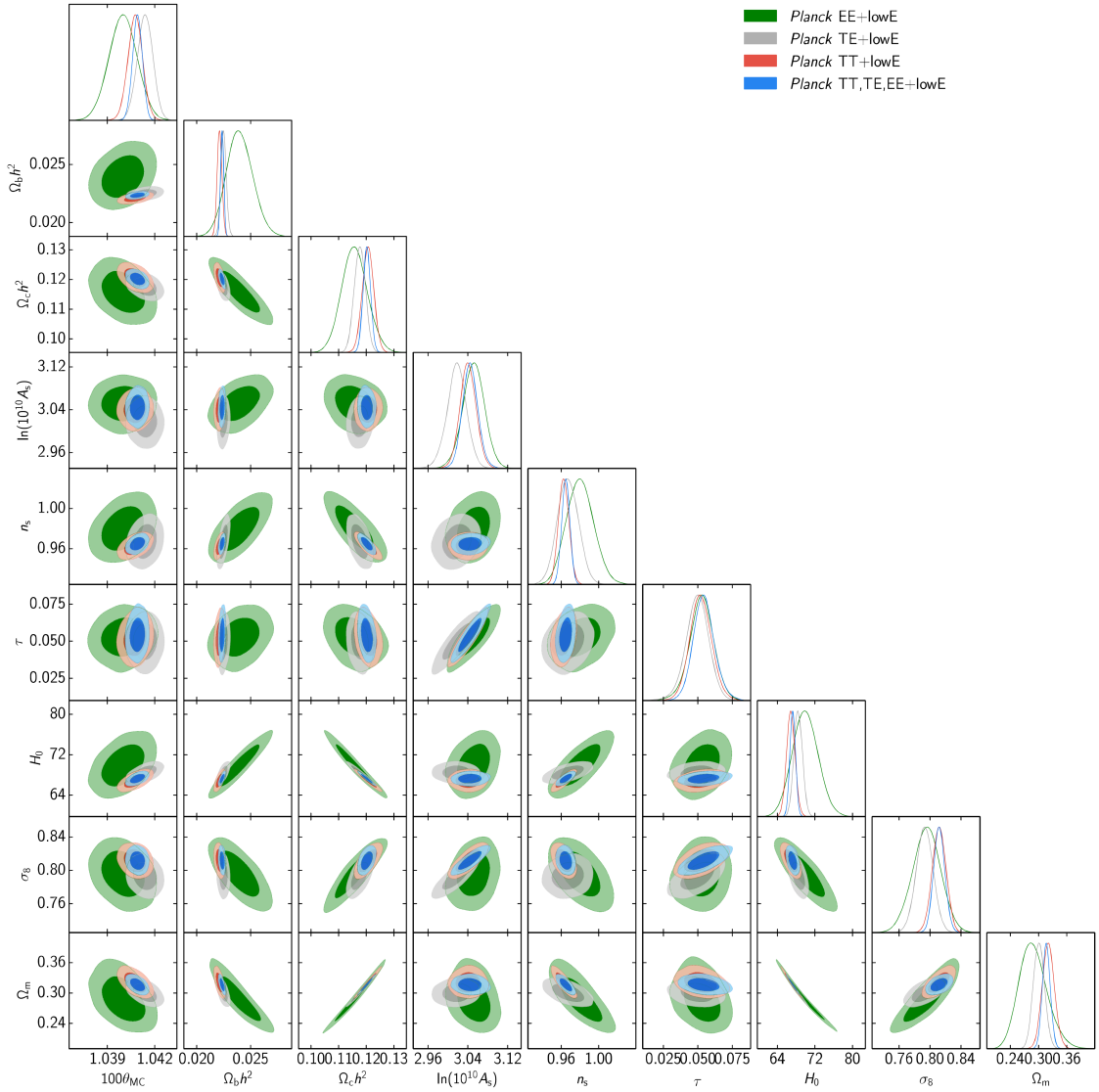

Figure 7.1: Contours of the ΛCDM parameters taken from Akrami et al. [2020]. The different colors in the plot represent different sets of modes considered.

found by the Planck collaboration. Comparing the two-dimensional marginalized contours allows to additionally verify that the directions of the correlations and anticorrelations of the distributions generated for this thesis match with the Planck 2018 results.

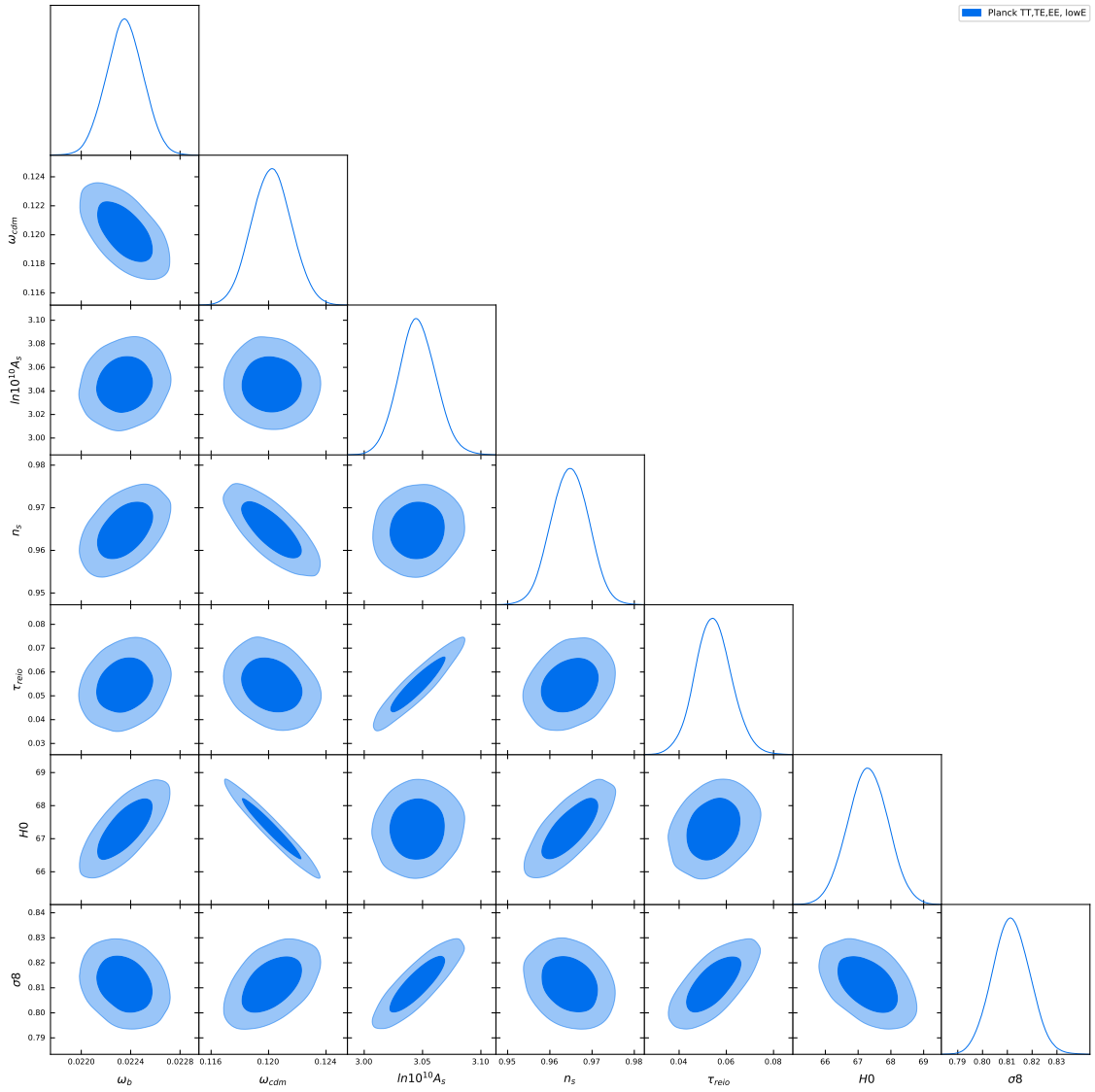

Figure 7.2: 68% (dark blue) and 95% (blue) confidence limits for the ΛCDM parameters. Used joint TT, TE, EE data, EE likelihood at low multipoles and TT likelihood at high multipoles.

Table 7.1: Mean values 95% confidence interval for the ΛCDM found with Planck 2018 data

Param	mean	95% interval
ω_b	0.02235	$[0.02206, 0.02265]$
ω_{cdm}	0.1202	$[0.1174, 0.1229]$
$ln10^{10}A_s$	3.046	$[3.013, 3.078]$
n_s	0.9648	$[0.956, 0.9736]$
τ_{reio}	0.05458	$[0.03855, 0.07048]$
$H0$	67.31	$[66.09, 68.53]$
$\sigma 8$	0.8114	$[0.7966, 0.8264]$

7.2 Spectral Index and its Runnings

After the confirmation in the previous section that the setup is computing ΛCDM parameters consistent with Akrami et al. [2020], a first method of constraining the primordial spectrum using this experiment can be tested. For the contours depicted in Figure 7.2 the primordial power spectrum was computed using the parametrization (6.1) while keeping the running of the spectral index α fixed and setting the running of the running $\beta = 0$. The scalar power spectrum A_s and the spectral index n_s were varied. In order to gain more information on inflation, the next step is to choose all parameters in (6.1) at random and then use the whole setup of MontePython and CLASS to constrain them.

In practice this is done by defining an external power spectrum in CLASS according to expression (6.1) and then sampling over the custom variables used to define it. MontePython then samples these additional parameters and calls CLASS with them, which in turn calls the external code that computes the primordial power spectrum. This is then used to compute the CMB spectra. These are compared to the Planck 2018 data which allows MontePython to compute likelihoods. The resulting 68% and 95% confidence limits are plotted in Figure 7.3. Note that all the ΛCDM parameters are also sampled over, however, in the generation of the figures they are marginalized over.

The best fit values and 68% error bars for all of the involved parameters are summarized in Table 7.2.

Table 7.2: Mean values 95% confidence interval for the spectral index and its runnings using Planck 2018 data

Param	mean	95% interval
ω_b	0.02233	$[0.02202, 0.02264]$
ω_{cdm}	0.1207	$[0.1179, 0.1236]$
h	0.6708	$[0.6584, 0.6833]$
$10^{10}A_s$	21.14	$[20.5, 21.81]$
n_s	0.9615	$[0.952, 0.971]$
α	0.003182	$[-0.01681, 0.02386]$
β	0.01256	$[-0.01122, 0.03706]$

The parameters used to describe the form of the primordial spectrum are A_s, n_s, α and β. They are within the error bars given in Akrami et al. [2020]. It is worth noting at this point that the values here are constrained only by the TT, TE, EE data in addition to the EE likelihoods for low multipoles and the TT likelihoods for high multipoles. The Planck 2018 values are also constrained by lensing. Figure 7.3 shows that the different parameters describing the primordial power spectrum in expression (6.1) are for the most part uncorrelated. There is a slight anticorrelation in $\{n_s, \beta\}$ and a somewhat stronger correlation in $\{\alpha, \beta\}$. Adding the data obtained

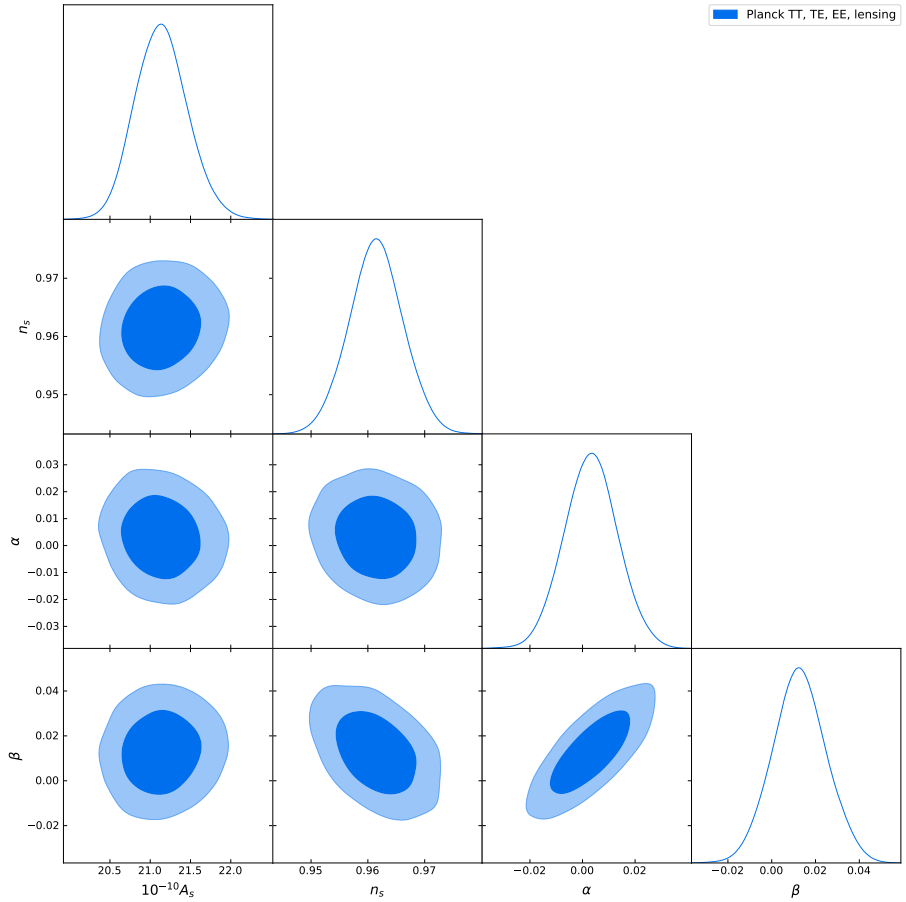

Figure 7.3: 68% (dark blue) and 95% (blue) confidence limits for the ΛCDM parameters and a modified power spectrum. Used joint TT, TE, EE data, EE likelihood at low multipoles, the TT likelihood at high multipoles.

through lensing would decrease the size of the contours as well as possibly change the mean values. Depending on the correlation of the parameters in the lensing data only, it might also change the orientation of the marginalized contours.

7.3 Slow-roll Parameters

The approach described in the previous section allows to find constraints on the primordial spectrum by parametrizing it using the spectral index and its runnings. In order to gain an even better understanding of the physics of inflation, the primordial spectrum is generated as described in chapter 6.1. This approach integrates the mode equations (3.36) to derive the primordial spectrum directly from the Hubble slow-roll parameters. Based on the allowed regions for the Hubble slow-roll parameters, inflationary models can then be checked for their consistency with a given experiment.

In practice the computation is performed using the typical setup of MontePython interfaced with CLASS, while the primordial spectrum is computed using the module described in Lesgourgues et al. [2008]. The 68% and 95% confidence limits for the Hubble slow-roll parameters using the Planck 2018 data (TT, TE, EE, lowE) are depicted in Figure 7.5. In addition to the slow-roll parameters plotted, the baryon density, cold dark matter density, Hubble parameter, the reionization optical depth and the nuisance parameters needed for the Planck data are sampled over. All of these are marginalized over to obtain Figure 7.5.

The contours found by this method and setup reproduce the results in Akrami et al. [2020]. This can be seen by comparing them to Figure 7.4 which was taken from Akrami et al. [2020]. Note that the contours derived in this analysis need to be compared to the dashed contours in Figure 7.4, as it does not include data from the BK15 experiment. The effect varying the slow-roll parameters in the parameter space allowed by Figure 7.5 and Table 7.3 has on the angular power spectra can be seen in figures 7.6b and 7.6a. Here, every thousandth Markov chain element from the Markov chains used to derive the constraints in Figure 7.5 is used as input parameters in CLASS to find the angular TT and EE power spectra associated to them. The different angular power spectrum realizations are largely similar for multipole order higher than 100 while the effect of choosing different Hubble slow-roll and cosmological parameters becomes apparent for low multipole orders. Since the different parameters chosen are the ones constrained by the Planck 2018 data, this also visualizes that in the region of multipole order 2 to 30 the data is not as constraining as for higher multipoles. A similar observation can be made when considering Figure 4.1 where the likelihoods at low multipole order are calculated using a different likelihood computation Akrami et al. [2020].

The noise model for the blue dotted lines in figures 7.6b and 7.6a is taken from Merkel and Schäfer [2017] and Knox [1995], it reads as

$$N^{TT}(\ell) = \left(\frac{\Delta_T}{T_{CMB}}\right)^2 e^{\frac{\theta^2_{\mathrm{FWHM}}\ell(\ell+1)}{8\ln(2)}} \frac{\pi\ell(\ell+1)}{2} \tag{7.1}$$

$$N^{EE}(\ell) = \left(\frac{\Delta_P}{T_{CMB}}\right)^2 e^{\frac{\theta^2_{\mathrm{FWHM}}\ell(\ell+1)}{8\ln(2)}} \frac{\pi\ell(\ell+1)}{2}. \tag{7.2}$$

Here, the CMB temperature was chosen as $T_{CMB} = 2.7255$, the Gaussian beam size

as $\theta_{\mathrm{FWHM}} = 7.1$ arcmin and the sensitivity with respect to temperature and polarization as $\Delta_T = 42.6\ \mu$K arcmin and $\Delta_P = 81.65\ \mu$K arcmin. The increasing noise level for higher order multipoles restricts the Planck experiment to the multipole order range depicted in Figure 4.1.

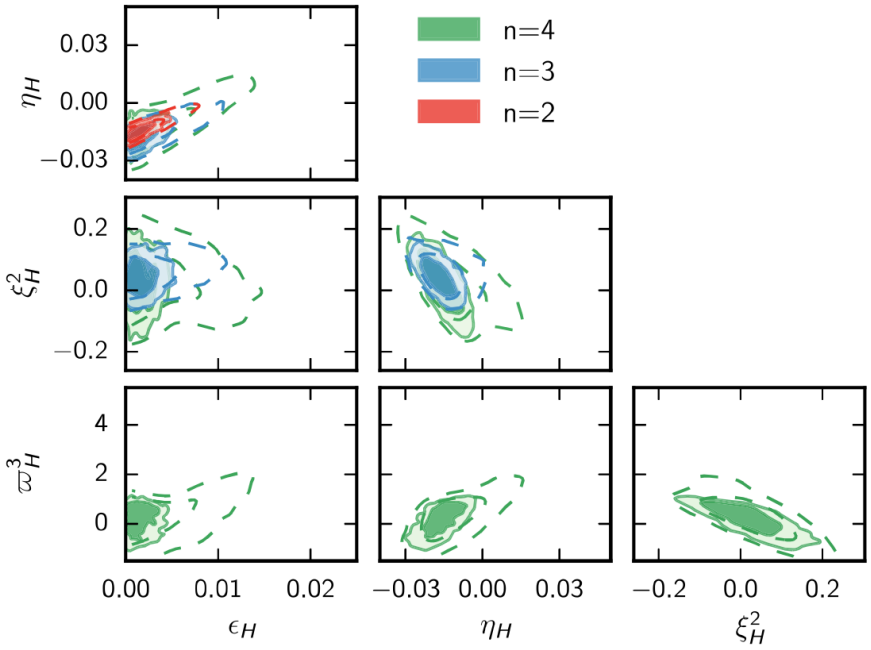

Figure 7.4: Contours for Hubble slow-roll parameters taken from Akrami et al. [2020]. Solid contours are Planck TT, TE, EE, lowE, lensing and BK15. Dashed contours are Planck TT, TE, EE, lowE.

Table 7.3: Mean values and 95% intervals for the cosmological and slow-roll parameters using Planck 2018 TT, TE, EE, lowE data

Parameter	mean	95% interval
$10^{-2}\omega_b$	2.242	$[2.211, 2.54]$
ω_{cdm}	0.1200	$[0.1173, 0.1227]$
h	0.6724	$[0.662, 0.686]$
τ_{reio}	0.05678	$[0.041, 0.075]$
$10^9 \tilde{A}_s$	2.084	$[1.978, 2.197]$
ϵ_H	0.006095	$[0.000000, 0.01518]$
η_H	-0.005849	$[-0.02804, 0.02104]$
ξ_H^2	0.01133	$[-0.1498, 0.1797]$
ω_H^3	0.5182	$[-1.213, 2.309]$

In order to gain some insight into the individual correlations between the different slow-roll parameters without the influence of the cosmological and the nuisance pa-

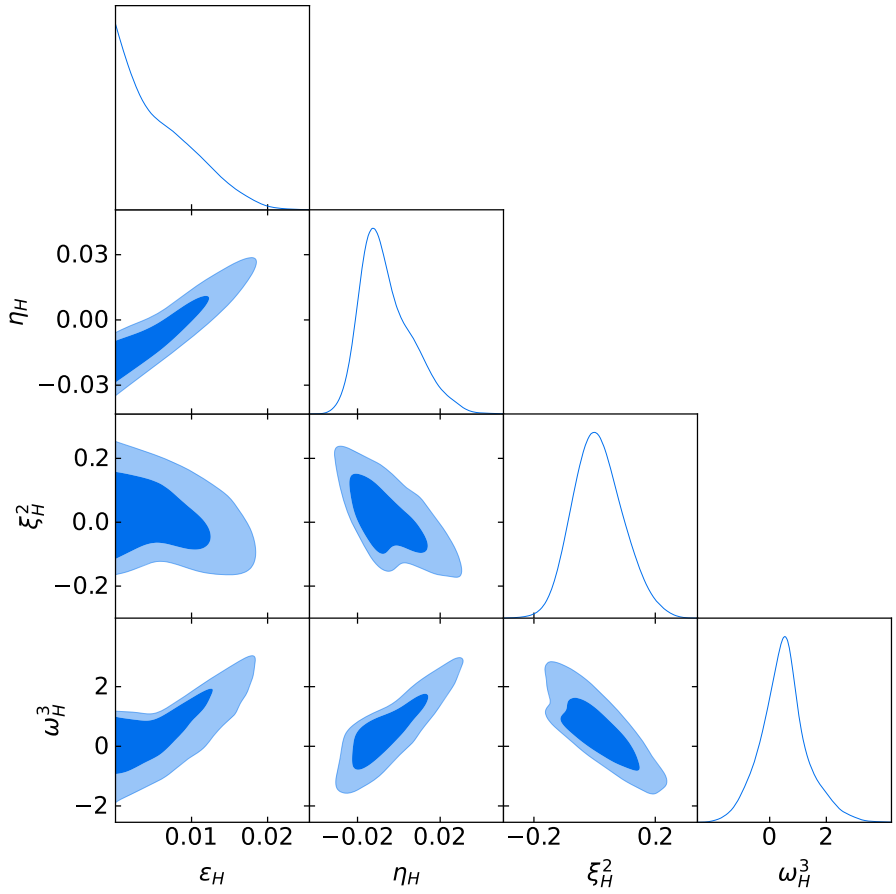

Figure 7.5: 68% (dark blue) and 95% (blue) confidence limits for the Hubble slow-roll parameters. Used joint TT, TE, EE data and EE likelihood at low multipoles and TT likelihood at high multipoles.

rameters, Figure 7.7 shows the correlation between the slow-roll parameters directly. In addition, Table 7.4 gives an overview over the mean values computed in this way and the 95% confidence regions. For the two-dimensional Planck correlations and their respective mean values $10^9 \tilde{A}_s$ was treated as a slow-roll parameter, since it modifies the amplitude of the Hubble parameter and with it the amplitude of the potential as well as the primordial power spectrum. All possible two-dimensional parameter correlations are plotted. For each correlation all parameters that are not varied over, i.e. the cosmological and nuisance parameters as well as the other slow-roll parameters, are set to the mean values obtained in generating Figure 7.4. The fixed values for the nuisance parameters are listed in the appendix A.1. Comparing the mean values from Table 7.4 to the values in Table 7.3 shows that they are consistent with each other, as expected after fixing all other parameters to the mean values from 7.3. The 95% confidence regions have decreased with the lower number of parameters probed. The two-dimensional correlations between the different Hubble slow-roll parameters give some insight which of the slow-roll parameters have a

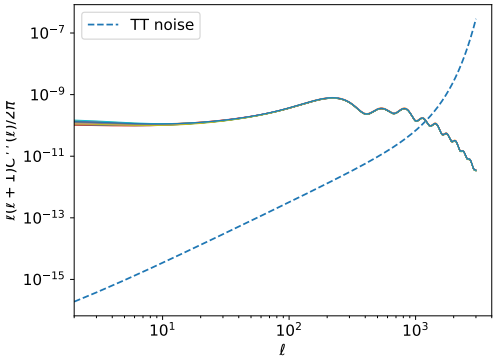

(a) Temperature fluctuations.

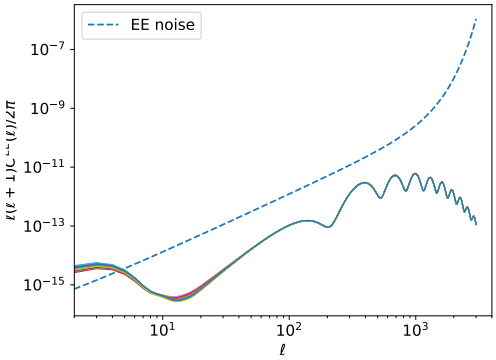

(b) EE polarization modes.

Figure 7.6: Different realizations of the angular CMB spectra, allowed by the Planck TT, TE and EE data with Planck noise levels.

similar effect on the angular spectra in the CMB. Comparison between the $\{\epsilon_H, \xi_H^2\}$ correlations between figures 7.7 and 7.4 allows to see that the direction and shape of the two-dimensional correlations do not easily explain the higher dimensional correlations.

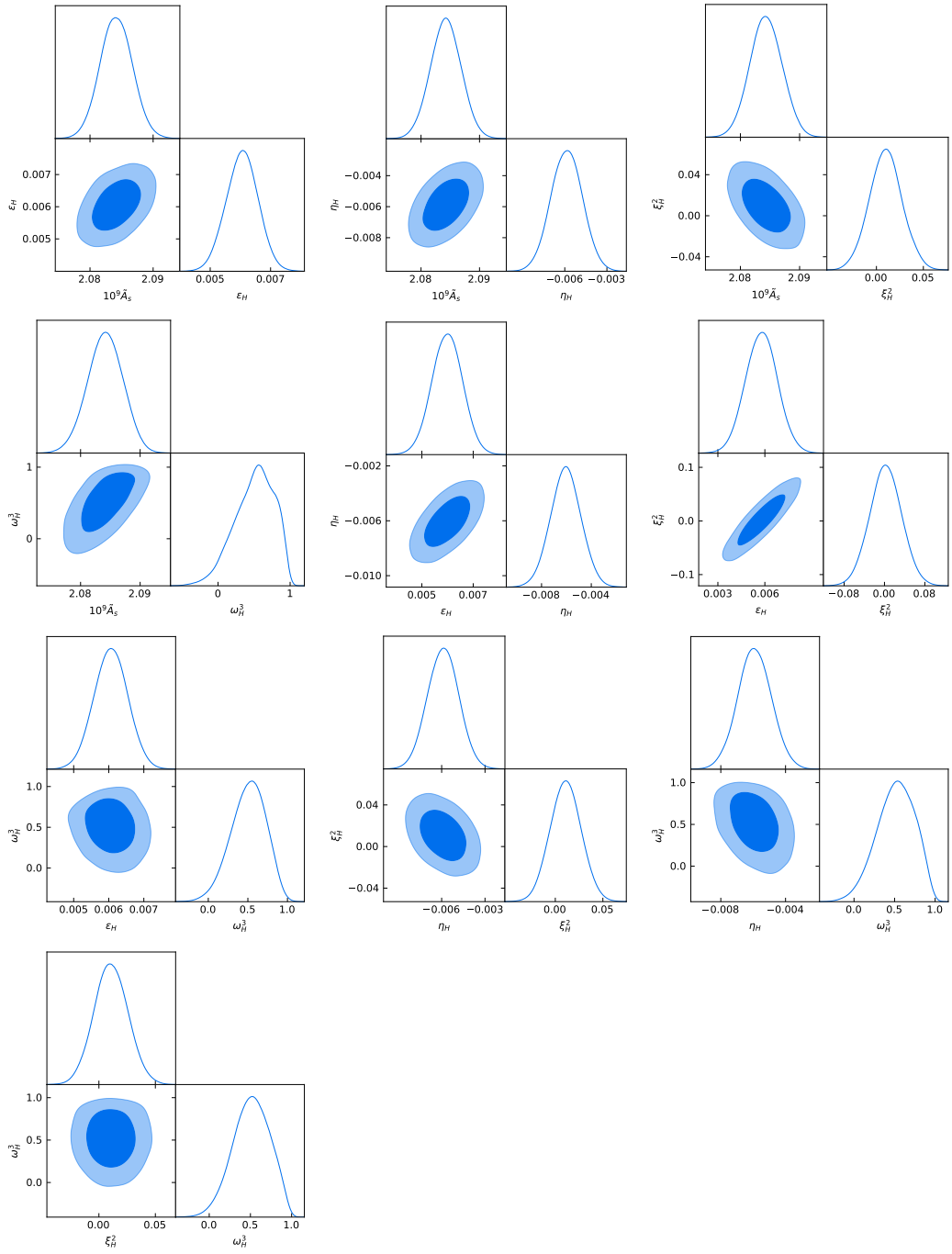

Figure 7.7: Two-dimensional 68% (dark blue) and 95% (blue) confidence limits for the Hubble slow-roll parameters. Used joint TT, TE, EE data, EE likelihood at low multipoles and TT likelihood at high multipoles.

Table 7.4: Mean values and error bars for 2D Markov chains using Planck 2018 data

Param	mean	95% interval
$10^9\tilde{A}_s$	2.0842	$[2.0792, 2.0892]$
ϵ_H	0.0061	$[0.0050, 0.0071]$
$10^9\tilde{A}_s$	2.0842	$[2.0791, 2.0894]$
η_H	-0.0059	$[-0.0081, -0.0037]$
$10^9\tilde{A}_s$	2.0843	$[2.0791, 2.0897]$
ξ^2_H	0.010	$[-0.024, 0.044]$
$10^9\tilde{A}_s$	2.0841	$[2.0782, 2.0898]$
ω^3_H	0.51	$[-0.02, 0.97]$
ϵ_H	0.0060	$[0.0048, 0.0072]$
η_H	-0.0061	$[-0.0085, -0.0037]$
ϵ_H	0.0058	$[0.0038, 0.0078]$
ξ^2_H	0.002	$[-0.059, 0.065]$
ϵ_H	0.00606	$[0.00513, 0.00699]$
ω^3_H	0.51	$[0.07, 0.92]$
η_H	-0.0059	$[-0.0080, -0.0038]$
ξ^2_H	0.011	$[-0.020, 0.043]$
η_H	-0.0059	$[-0.0079, -0.0039]$
ω^3_H	0.52	$[0.07, 0.94]$
ξ^2_H	0.011	$[-0.018, 0.040]$
ω^3_H	0.51	$[0.09, 0.93]$

8 Square Kilometer Array Results

The previous chapter allowed to verify that the computation of contours for both the spectral index and its runnings as well as the slow-roll parameters can be performed using the combination of MontePython and CLASS described above and obtain results that match with the Planck 2018 results. This chapter focuses on applying these two methods to the SKA. To that end, the likelihood for the SKA are constructed as described in 6.4. In the computation of the SKA likelihoods a fiducial power spectrum is used, for computations involving the Hubble slow-roll parameters this spectrum is chosen to be the spectrum resulting from setting all cosmological parameters and Hubble slow-roll parameters to the ones found in the generation of Figure 7.5. The explicit parameter values are shown in Table 7.3. For computations involving the spectral index and its runnings the parameter values to generate the fiducial spectrum are chosen according to the values found in Table 7.2.

This chapter will first present the results for a parametrization of the primordial spectrum using the spectral index and its runnings. In a next step, the slow-roll parameters are constrained using the formalism in Lesgourgues et al. [2008].

8.1 Spectral Index and its Runnings

First the contours for a ΛCDM model with a modified power spectrum according to equation (6.1) are computed using only the SKA likelihoods constructed according to chapter 6.4. Figure 8.1 contains all parameters that are sampled over. The optical depth to reionization τ_{reio} is not treated as a free parameter, since the simulated data of SKA alone can not constrain it. This can be understood from the construction of the likelihood, where we assumed that the ionized fraction of the helium is zero. Thus, at the time at which we simulate the power spectrum to get the 21cm data reionization has not started yet. Consequently this simulated data cannot constrain the optical depth until the onset of reionization. However, the assumption that reionization has not yet started at this redshift itself gives an upper limit on the optical depth to reionization, depending on the model for reionization. For instantaneous reionization at redshift $z_{reio} = 8$ and using the approximate formula

$$\tau(z_{reio}) = 0.03 \frac{\Omega_b h_{75}^2}{\sqrt{\Omega_m h_{75}^2}} z_{reio}^{\frac{3}{2}} \tag{8.1}$$

taken from Mukhanov [2005] together with the approximations $\Omega_b h_{75}^2 \approx 0.004$ and $\Omega_m h_{75}^2 \approx 0.3$ allows to compute an optical depth of about 0.05. This gives a rough

upper limit for the optical depth until reionization for which the approximations made in sections 6.4 are valid. The dashed red contours in Figure 8.1 correspond to the 68% and 95% marginalized contours for a shorter observation time of 1000 hours. This reduces the accuracy with which the SKA can constrain the different parameters by roughly a factor two. It is worth noting that, while most of the constraints on the cosmological parameters ω_b and ω_{cdm} are significantly stronger than the constraints found when using the Planck 2018 data, the constraint on the reduced Hubble parameter is weaker by more than an order of magnitude for both 1000 and 10000 hours of observation time. The SKA constraints on the reduced Hubble parameter h are weaker than the Planck 2018 data.

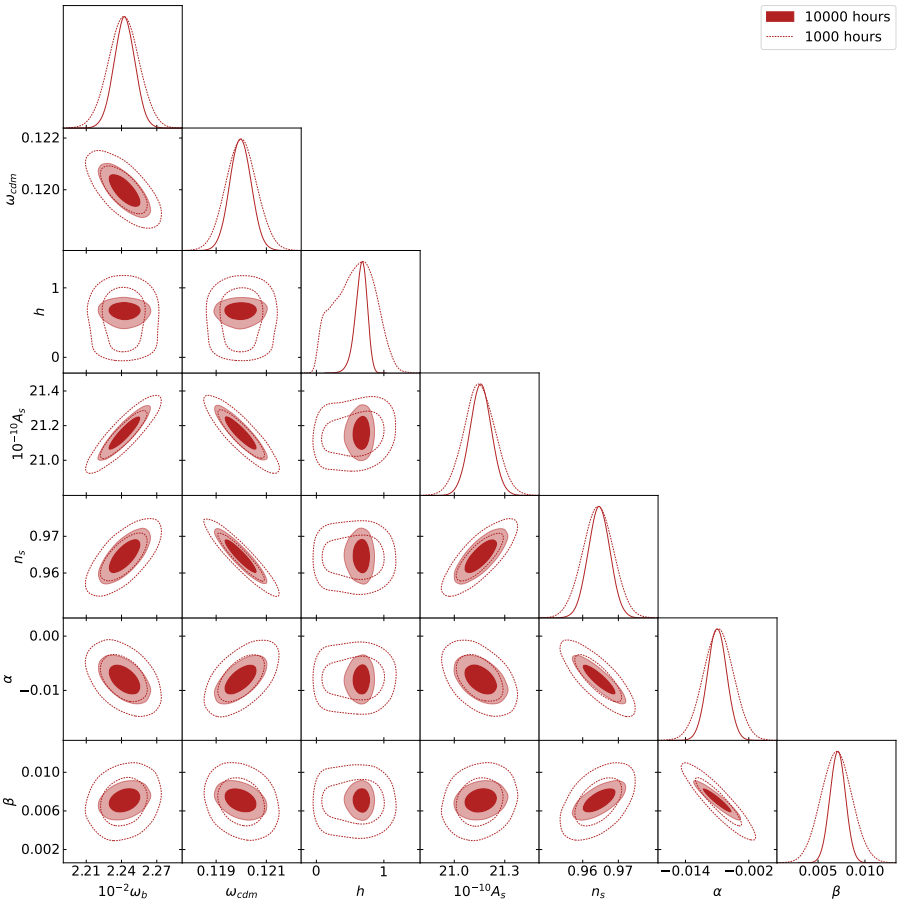

Figure 8.1: 68% and 95% level contours ΛCDM parameters and the spectral index and its runnings for SKA with 10000 hours observation time (red filled) and SKA with 1000 hours observation time (red dashed). Used the SKA likelihood described in section 6.4.

The parameters describing the primordial power spectrum and thus contain information on inflation are shown separately in Figure 8.2. Here, the filled red contours correspond to the constraints on the scalar amplitude A_s, the spectral index n_s and

its runnings α and β using the likelihoods described in section 6.4. The dashed red lines correspond to the contours obtained when the observation time is reduced by a factor of ten to 1000 hours. Comparing the dashed red contours with the filled contours and considering Table 8.1 allows to see that the reduced observation time leads to somewhat weaker constraints in all parameters. For A_s, n_s and α the constraints become weaker by about a factor 1.5, while the constraint on β is about a factor two weaker.

Comparing to Figure 7.3 allows to find that SKA, with the likelihoods defined in section 6.4, can constrain the quantities describing the primordial spectrum significantly better than the Planck 2018 data. Some of the contours, especially the $\{\alpha, \beta\}$ contour, also have different orientations. Considering in addition the 95% confidence limits displayed in tables 7.2 and 8.1 reveals that A_s and n_s are only slightly better constrained, while and α and β are already better constrained only with SKA data by about an order of magnitude. Overall, the simulated SKA likelihood seems to exhibit more and stronger correlations between the parameters.

Table 8.1: Mean values and error bars for the spectral index and its runnings using the SKA likelihoods constructed as in 6.4

	SKA (10000 hrs)		SKA (1000 hrs)	
Parameter	mean	95% interval	mean	95% interval
$10^{-10}A_s$	21.20	$[21.07, 21.32]$	21.19	$[21.01, 21.38]$
n_s	0.9609	$[0.9549, 0.9669]$	0.9609	$[0.9524, 0.9695]$
α	0.0030	$[-0.0006, 0.0066]$	0.0030	$[-0.0025, 0.0085]$
β	0.0140	$[0.0124, 0.0156]$	0.0141	$[0.0109, 0.0172]$

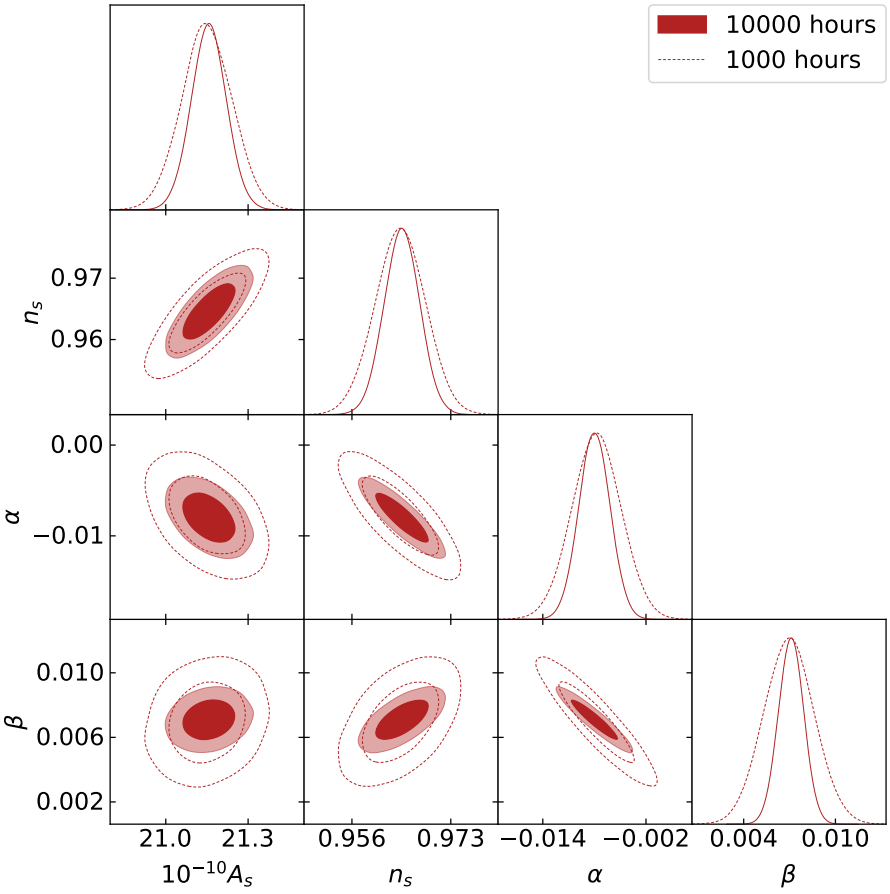

Figure 8.2: 68% and 95% level contours for the scalar amplitude, the spectral index and its runnings for SKA with 10000 hours observation time (red filled) and SKA with 1000 hours observation time (red dashed). Used the SKA likelihood described in section 6.4.

8.2 Slow-roll Parameters

Similarly to chapter 7 the SKA can also be used to constrain the shape of the Hubble function during inflation directly. This is done using the Hubble slow-roll parameters described in chapter 6. The analysis is performed by starting out with exploring the two-dimensional correlations between pairs of slow-roll parameters with fixed cosmological parameters. In a next step, three of the slow-roll parameters are used as free parameters, which already yield very strong correlations in some parameter combinations. These correlations make the analysis of the four and five-dimensional combinations of slow-roll parameters very difficult, in fact, neither the five-dimensional combination nor all of the four-dimensional combinations of slow-roll parameters converge.

8.2.1 Two-dimensional Results

In a first step, the two-dimensional correlations between all parameter pairs are found while keeping both the cosmological parameters as well as the slow-roll parameters not shown in the plots fixed. This analysis is shown in Figure 8.3. From this and the 95% confidence regions shown in Table 8.2 it is already visible that at least for two-dimensional correlations of the slow-roll parameters the SKA is immensely more constraining than the Planck 2018 data. In addition, the different two-dimensional contours exhibit strong correlations and anticorrelations. The most notable ones of these are the correlation between $\{\epsilon_H, \eta_H\}$ and $\{10^9\tilde{A}_s, \epsilon_H\}$ as well as the anticorrelations between $\{10^9\tilde{A}_s, \eta_H\}$ and $\{\epsilon_H, \xi_H^2\}$. The fourth slow-roll parameter ω_H^3 does not appear to be correlated to the other slow-roll parameters in the two-dimensional cases.

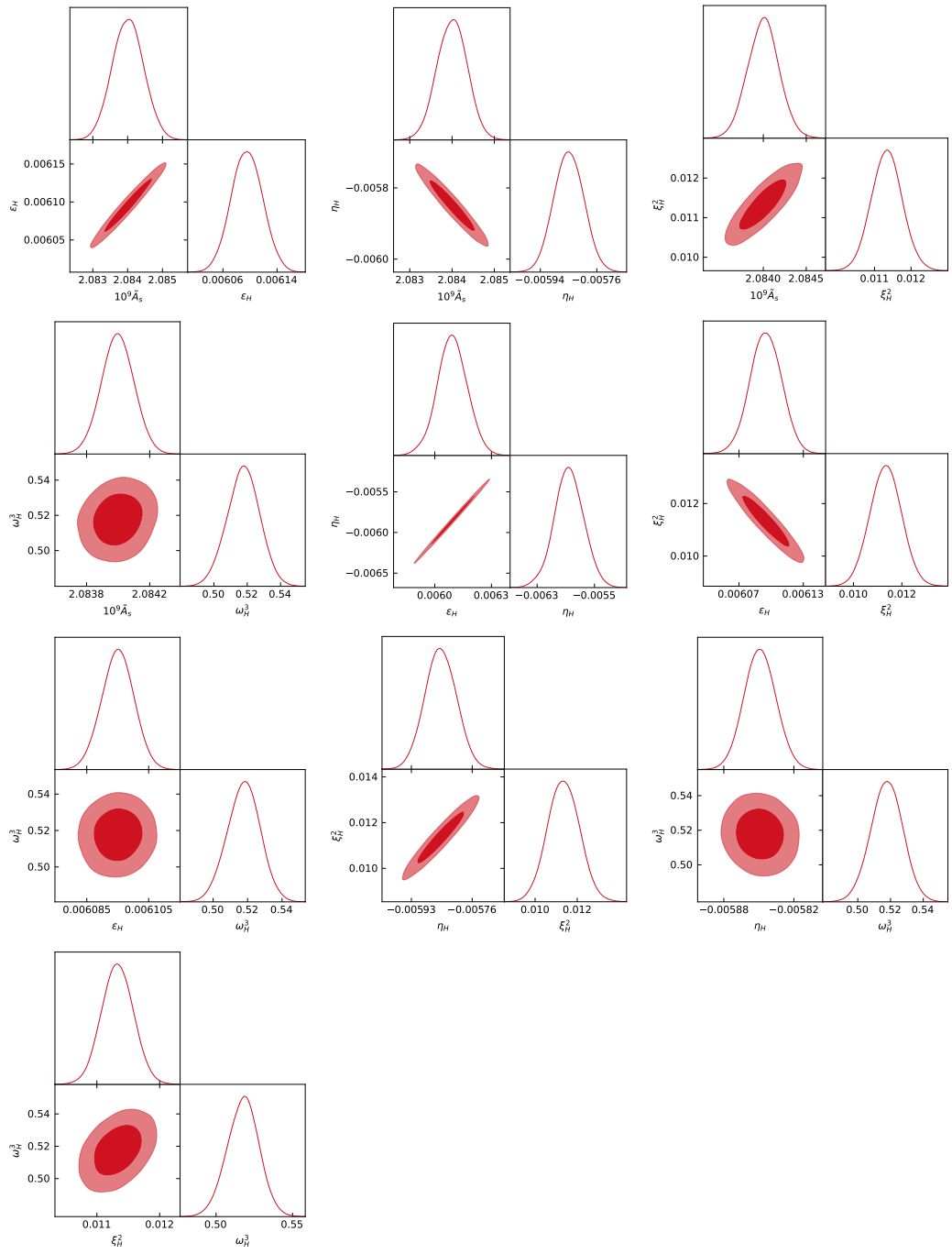

Figure 8.3: Two-dimensional 68% and 95% level contours using SKA likelihoods as computed in 6.4.

Table 8.2: Mean values and error bars for 2D Markov chains using SKA likelihoods as constructed in 6.4

Param	mean	95% interval
$10^9 \tilde{A}_s$	2.08401	$[2.08314, 2.08489]$
ϵ_H	0.006096	$[0.006050, 0.006141]$
$10^9 \tilde{A}_s$	2.08400	$[2.08331, 2.08469]$
η_H	-0.005849	$[-0.005941, -0.005756]$
$10^9 \tilde{A}_s$	2.08400	$[2.08365, 2.08436]$
ξ_H^2	0.01134	$[0.01052, 0.01218]$
$10^9 \tilde{A}_s$	2.08400	$[2.08379, 2.08420]$
ω_H^3	0.518	$[0.498, 0.537]$
ϵ_H	0.00609	$[0.00593, 0.00625]$
η_H	-0.00586	$[-0.00627, -0.00545]$
ϵ_H	0.006095	$[0.006066, 0.006123]$
ξ_H^2	0.0113	$[0.0101, 0.0126]$
ϵ_H	0.006095	$[0.006085, 0.006105]$
ω_H^3	0.518	$[0.499, 0.536]$
η_H	-0.005848	$[-0.005933, -0.005762]$
ξ_H^2	0.0114	$[0.0099, 0.0128]$
η_H	-0.005849	$[-0.005875, -0.005822]$
ω_H^3	0.518	$[0.498, 0.537]$
ξ_H^2	0.01133	$[0.01083, 0.01183]$
ω_H^3	0.518	$[0.497, 0.538]$

8.2.2 Three-dimensional Results

In a next step, three parameters are varied at the same time to gain insight into the impact an additional parameter has on the contours. The ten different combinations are plotted as scatter plots of the Markov chain points in Figure 8.4. This gives a good impression of the position and orientation of the Markov chain in the parameter space and quantifies degeneracies between parameters. The shadows on the parameter walls are marginalizations onto planes keeping one parameter fixed. For the three-dimensional results parameter triplets with strong correlations can be identified, these include $\{\tilde{A}_s, \epsilon_H, \xi_H^2\}$, $\{\tilde{A}_s, \eta_H, \xi_H^2\}$, $\{\epsilon_H, \xi_H^2, \omega_H^3\}$, $\{\eta_H, \xi_H^2, \omega_H^3\}$ and, most notably, the correlations between the first three slow-roll parameters in which the accumulated points are just a thin line in three-dimensional space. While all of these parameter combinations exhibit directions in which they appear correlated only for the $\{\tilde{A}_s, \epsilon_H, \eta_H\}$ combination, the likelihood cloud seems to bend slightly in the negative η_H direction for large values of $\tilde{A}_s$ and ϵ_H.

The three-dimensional plots in 8.4 give a good intuition of the position of the Monte Carlo Markov chain in space. However, it is not very easy to do further analysis with it and especially not possible to give constraints on single parameters. Instead, Figure 8.5 shows the marginalized contours when varying three slow-roll parameters at the same time. The upper-most plot in each column is the marginalized one-dimensional distribution of the Markov chain points for the parameter that this column corresponds to. In addition to the correlations found by varying three parameters, plotted in green, the correlations found by varying only two parameters are superimposed in red and blue. This allows to track the influence of a third parameter on the different parameter correlations. In fact, it is possible to predict some of the behavior of the contours generated using three parameters from the shape of the contours in 8.3. Taking the $\{\tilde{A}_s, \epsilon_H, \omega_H^3\}$ plot as an example it is possible to see that the strong correlation between $\{\tilde{A}_s, \epsilon_H\}$ leads to a correlation in the previously uncorrelated $\{\tilde{A}_s, \omega_H^3\}$ and $\{\epsilon_H, \omega_H^3\}$ contours, since with a varying third parameter the contour only moves in a very specific direction. Similarly, it is not surprising that the direction of the $\{\tilde{A}_s, \epsilon_H\}$ contour does not change a lot upon introducing ω_H^3 as a free parameter because it is not correlated with either of them. A similar argument can be made to explain the orientation of the contours for any of the parameter combinations involving the fourth slow-roll parameter ω_H. For combinations that involve three parameters which are pairwise correlated or anticorrelated with each other the situation gets somewhat more complicated. The combination $\{\tilde{A}_s, \eta_H, \xi_H^2\}$ is an example where the correlation in $\{\tilde{A}_s, \eta_H\}$ for two varying parameters seems to transition into an anticorrelation when varying ξ_H^2 as well. Similarly, the orientation of the other two contours in this plot are also altered by the anticorrelation in $\{\tilde{A}_s, \eta_H\}$. In principle, even for this case, the amount of correlation and anticorrelation the contours for two free parameters exhibit should provide some information on the respective contours when varying three parameters. However, quantifying how strong the correlations are goes beyond the scope of this work.

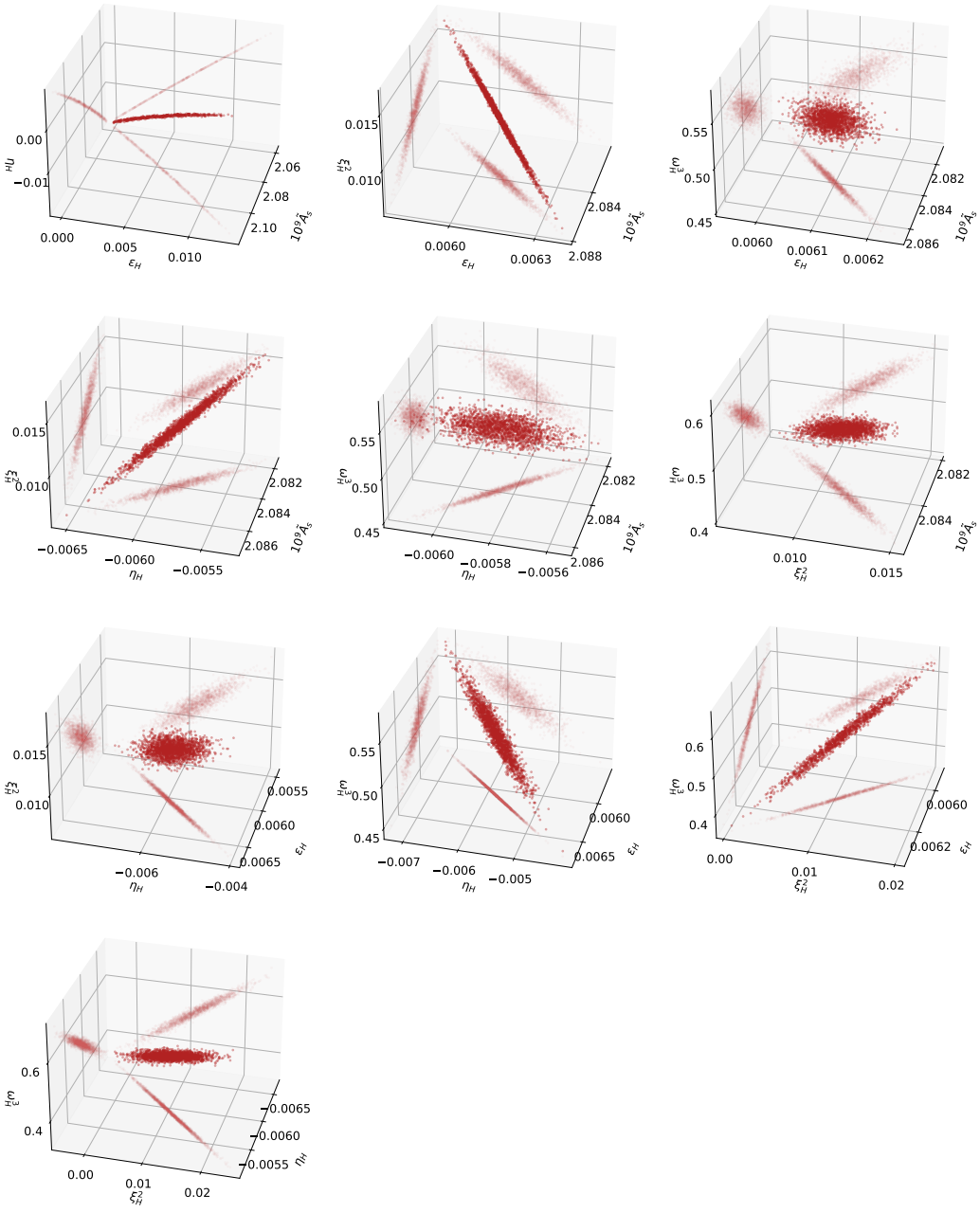

Figure 8.4: Markov chain points in three-dimensional parameters space generated with SKA likelihoods computed as described in 6.4.

The marginalized contours for $\{\tilde{A}_s, \epsilon_H, \eta_H\}$ show an enhancement of the correlations in $\{\tilde{A}_s, \epsilon_H\}$ and $\{\epsilon_H, \eta_H\}$ while flipping the anticorrelation in $\{\tilde{A}_s, \eta_H\}$ into a strong correlation. This might be explained by the fact that both $\{\tilde{A}_s, \epsilon_H\}$ and $\{\epsilon_H, \eta_H\}$ exhibit very strong correlations already for two free parameters. For this particular three-dimensional combination of parameters the computational setup

struggles to find a proposal distribution that allows to find a good amount of accepted points, however, the three-dimensional Markov chain still converges.

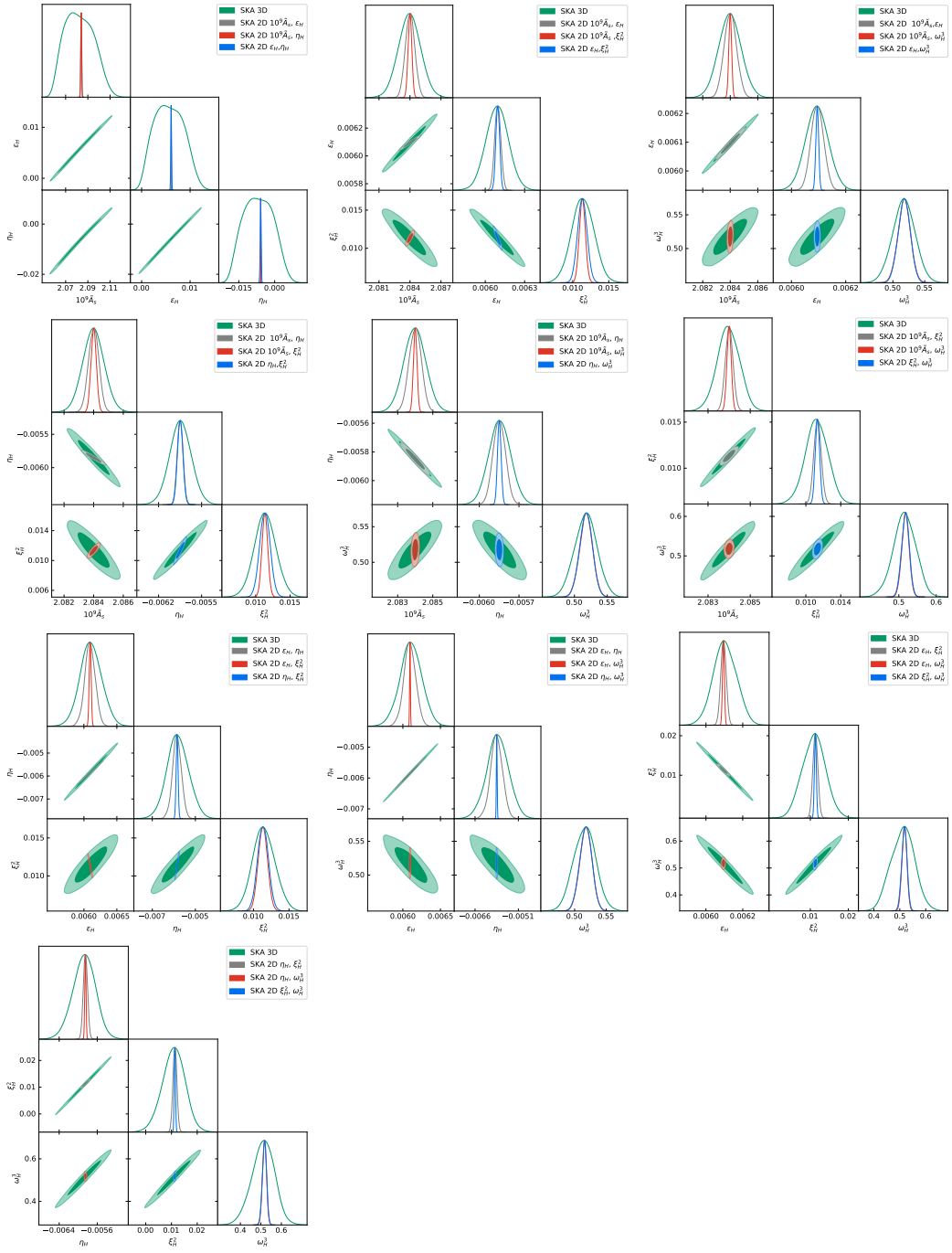

Figure 8.5: Three-dimensional 68% and 95% level contours using SKA likelihoods as computed in 6.4..

Adding a third free parameter to the computation of the likelihoods and the contours for the slow-roll parameters leads to much stronger marginalized correlations

and with that much larger error bars for the individual parameters. Figures 8.6 to 8.8 show that this is indeed an effect of varying this additional parameter. In these figures one parameter in the three-dimensional Markov chains is selected and only those points within a small region around the mean value found in 7.3 are taken into account to generate the figures. For each three-dimensional Markov chain three of these sliced chains are generated. They can then be compared to the corresponding two-dimensional Markov chains where the other three parameters are fixed to their fiducial values from the beginning. As shown in figures 8.6 to 8.8 the cut chains exhibit mean parameter values and correlations very similar to the two-dimensional Markov chains. There are some differences between the cut chains and the two-dimensional chains, for example the mean values in the $\{\tilde{A}_s, \omega_H^3\}$, $\{\eta_H, \omega_H^3\}$, $\{\omega_H^3\}$ and $\{\tilde{A}_s, \xi_H^2\}$ cases do not match exactly. In addition, the shape of some of the contours using the sliced chains are slightly wobbly. This can be explained by the comparatively low number of points in the parameter slices. If more points are included by increasing the interval around the fiducial values, for which points are included in the cut chains, the effects of varying a third parameter can be seen directly. The contours then enlarge in the directions seen in 8.5. This shows that the change of contours generated by varying three parameters and those generated with only two free parameters are indeed consistent.

While it is possible to vary more than three Hubble slow-roll parameters and still have converging Markov chains, the strong correlations seen for the combination $\{\tilde{A}_s, \epsilon_H, \eta_H\}$ is also present when varying more parameters at once, making their analysis difficult. In the timescales considered for the analysis, i.e. 48 hours on 16 chains in parallel, it was not possible to collect enough Markov chain points to find sensible constraints. In the four-dimensional case it is feasible to find contours and parameter constraints for any of the combinations that do not include the combination above. They are shown in Figure B.1 in the Appendix.

For the five-dimensional case no converging Markov chains using only the SKA likelihoods could be obtained. It may be possible to address this problem by performing a principal component analysis and redefining the parameters such that there are weaker correlations.

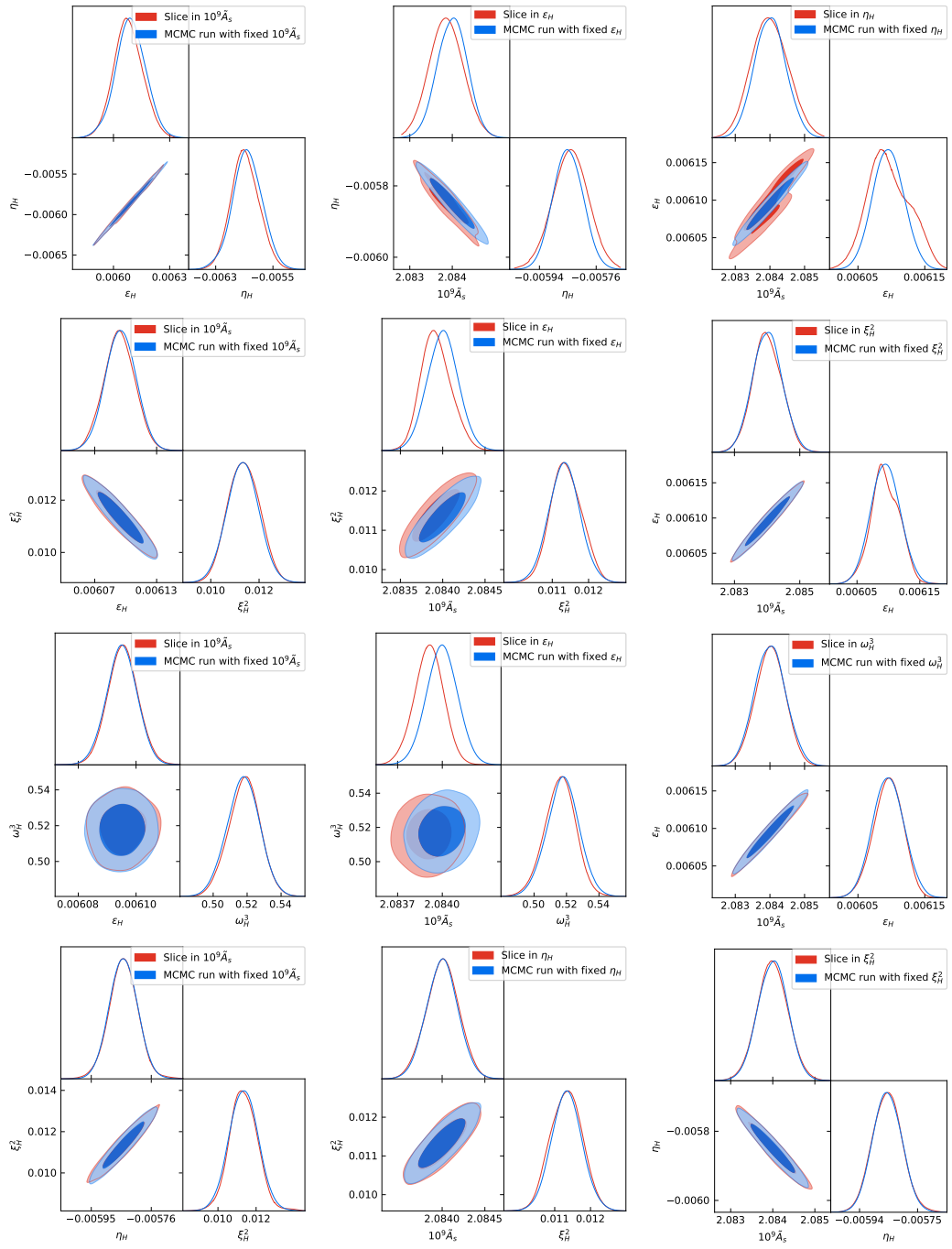

Figure 8.6: Comparison between slices and 2D SKA contours, each row corresponds to slices taken from one 3D SKA chain.

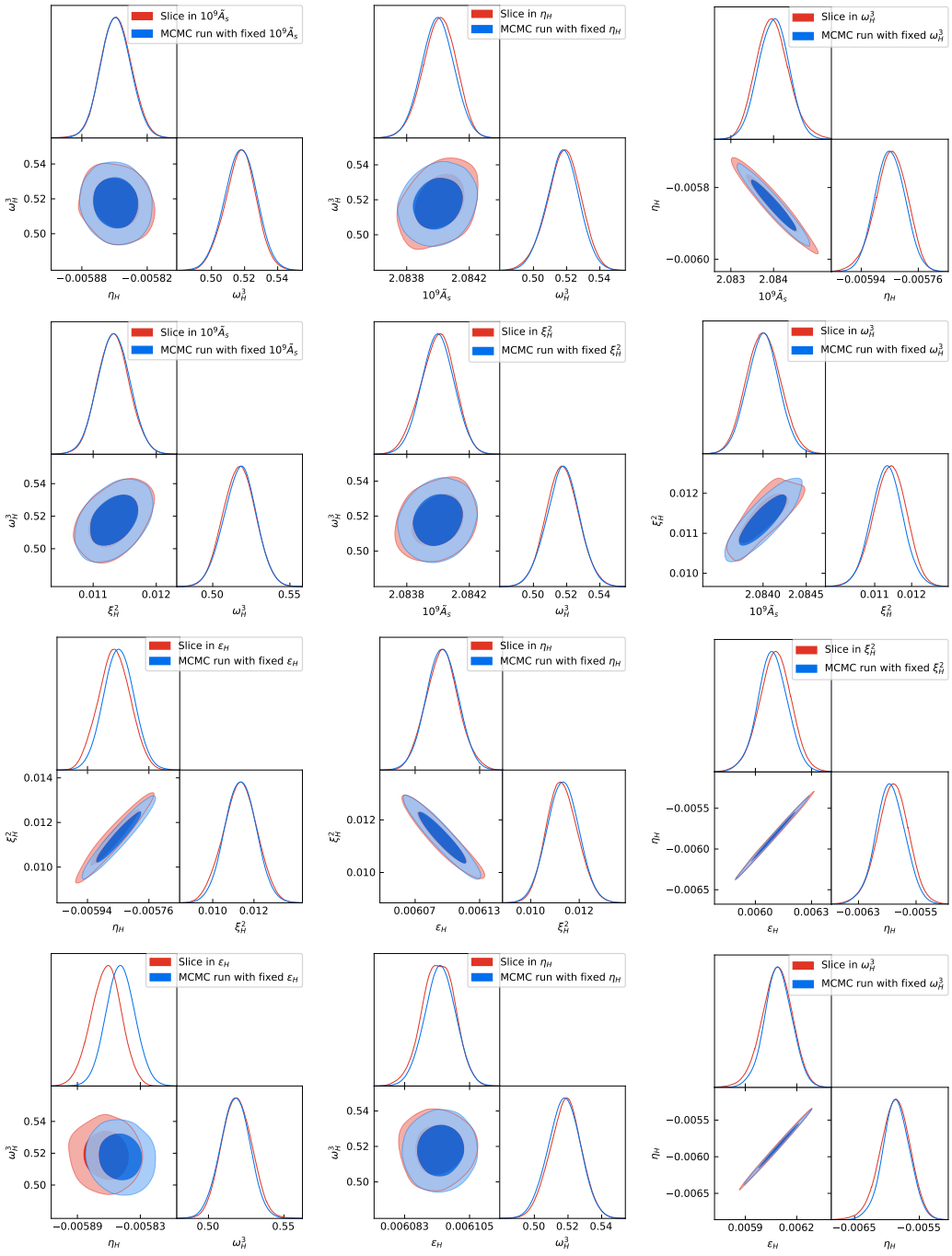

Figure 8.7: Comparison between slices and 2D SKA contours, each row corresponds to slices taken from one 3D SKA chain.

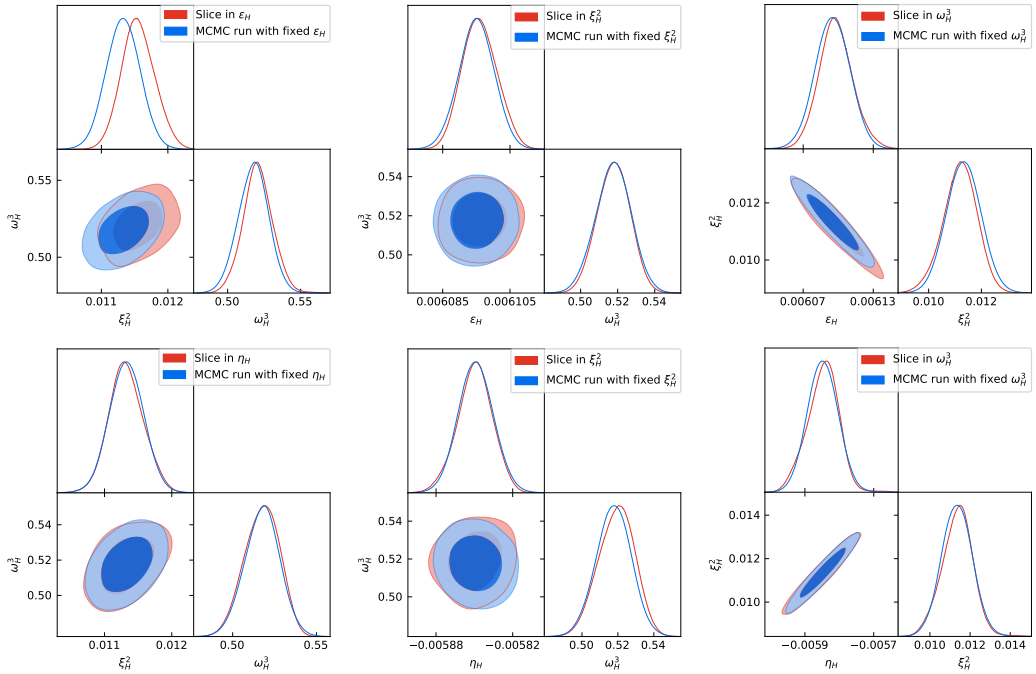

Figure 8.8: Comparison between slices and 2D SKA contours, each row corresponds to slices taken from one 3D SKA chain.

9 Combined Results

As shown in chapters 7 and 8 the two experiments show different behavior when constraining parameters describing inflation. For the spectral index and its runnings the constraints from the SKA are much stronger than the Planck 2018 constraints leading to combined constraints at about the same level of the SKA constraints. In the case of Hubble slow-roll parameters the situation is different since the Planck 2018 data allows to constrain the slow-roll parameters up to order four, while the simulated SKA data can only constrain them well up to second order. However, the slow-roll parameters are much stronger constrained by the SKA data. In the following the likelihoods computed in the two experiments are combined to find constraints on the first four slow-roll parameters. This is done by adding the likelihoods under the assumption that they are uncorrelated.

9.1 Spectral Index and its Runnings

The combination of the simulated SKA likelihood with the likelihood computed from the 2018 Planck data allows to constrain the spectral amplitude, the spectral index and its runnings slightly better than SKA alone and significantly better than the Planck 2018 data alone. Figure 9.1 shows the marginalized one and two-dimensional distributions for Planck alone in blue, for SKA alone in red and for their combination in purple. From the relative sizes of the contours it is clear that the much stronger constraints of the SKA drives the combined constraints to their small values. However, adding the Planck 2018 likelihood values does have the impact of slightly decreasing the contours only from SKA. The strength of the constraints due to the SKA when compared to Planck 2018 alone can be explained by considering the construction of the primordial spectrum in expression (6.1). The spectral index and its runnings modify the primordial spectrum such that their influence is small at comoving wave number values close to the pivot scale, while far away from the pivot scale their influence is large. The SKA measures at comoving wave number further away from the pivot scale, such that the spectral index and especially its runnings can be constrained much better.

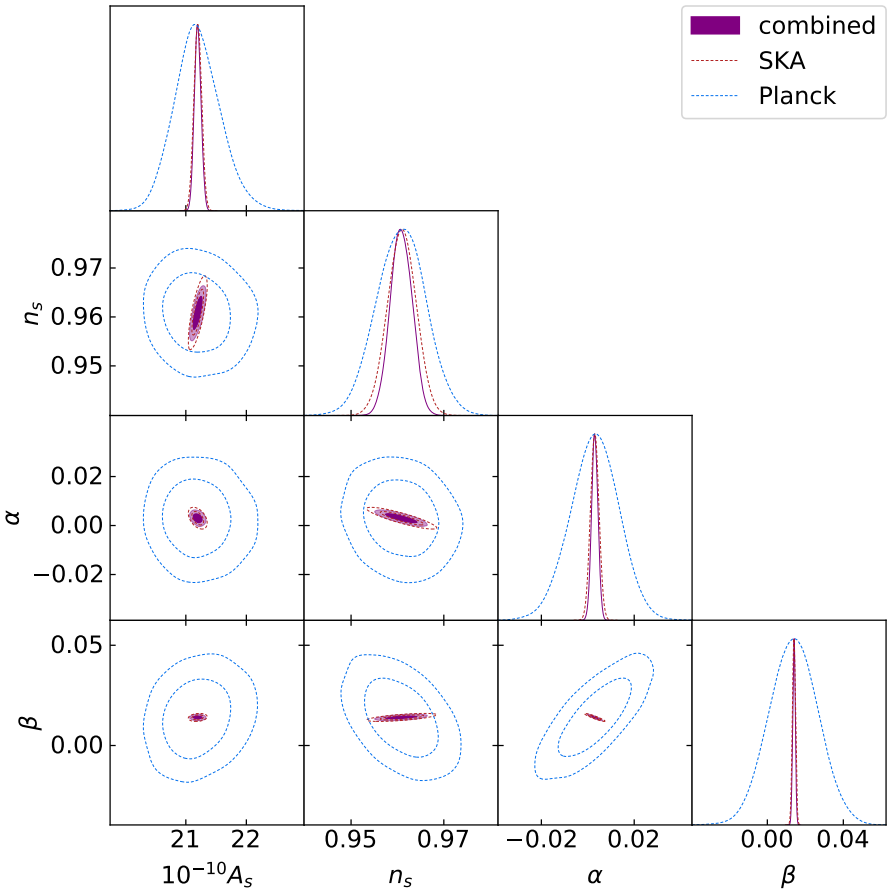

Figure 9.1: 68% and 95% level contours for the scalar amplitude, the spectral index and its runnings for SKA with 10000 hours observation time + Planck 2018 (TT, TE, EE, lowE, highT) (purple), SKA with 10000 hours observation time (red dashed) and Planck 2018 (TT, TE, EE, lowE, highT) (blue dashed). Used the SKA likelihood described in section 6.4.

Table 9.1: Mean values and 95% intervals for the spectral amplitude, index and its runnings using Planck 2018 and SKA combined.

Parameter	mean	95% interval
$10^{-10}A_s$	21.20	$[21.09, 21.31]$
n_s	0.9608	$[0.9562, 0.9653]$
α	0.0030	$[0.0003, 0.0058]$
β	0.0140	$[0.0127, 0.0154]$

9.2 Slow-roll Parameters

Similarly to the analysis in the previous chapter this section will first consider the two-dimensional results obtained when varying only two parameter and then go on to dimension three. Considering the Planck 2018 data on top of the SKA likelihood indeed allows to find decent amounts of Markov chain points for all three-dimensional combinations.

In Figure 9.2 the two-dimensional contours obtained from combining the likelihoods found using the Planck 2018 data and the SKA are shown. As can be seen from the SKA contours plotted as red dashed lines, the addition of the Planck likelihoods does not have a large impact on the two-dimensional constraints. This can be understood by comparing the 95% confidence intervals obtained in Table 7.4 and 8.2 or the overall sizes of the two-dimensional contours between figures 7.7 and 8.3. Overall the SKA contours are about an order of magnitude more constraining than the Planck contours. Adding the two likelihoods to obtain combined constraints therefore does not add a lot of constraining power in the two-dimensional case. This can also be verified by comparing the 95% confidence intervals in Table 9.2 to those in Table 8.2. As was the case for the two-dimensional Planck and SKA contours, all cosmological and nuisance parameters involved as well as those slow-roll parameters not on the axes of the plots are kept fixed to their fiducial values.

In addition to the two-dimensional results the combination of the two likelihoods allows to find converging contours for more than two free parameters. The contours found when varying three slow-roll parameters are shown in Figure 9.3. Considering the parameter combination $\{\tilde{A}_s, \epsilon_H, \eta_H\}$ the effect of adding the Planck likelihoods is clearly visible. The one-dimensional marginalized parameter distributions have a cleaner peak. The acceptance rate for the combined likelihoods could be driven to higher values, allowing to find an adequate amount of Markov chain points to get a clear three-dimensional result. This is possible, since the Planck 2018 data disallows some of the parameter space accessed by the strong correlations. The other parameter combinations exhibit the same behavior as the ones found when considering the SKA likelihood only as depicted in Figure 8.5. Adding the Planck likelihoods to the simulated SKA likelihoods thus allows to find the behavior of the $\{\tilde{A}_s, \epsilon_H, \eta_H\}$ combination. The size of the contours and confidence limits found for these and all other slow-roll parameters are at levels similar to the SKA results.

In fact, the combined SKA and Planck likelihoods allow to find parameter constraints for all of the Hubble slow-roll parameters at once. In order to compare them to the results in Figure 7.5 the cosmological parameters, including the optical depth until reionization τ_{reio}, as well as all nuisance parameters, were chosen as free parameters. The results of this analysis are shown in Figure 9.4 and Table 9.3.

Considering Table 9.3 and comparing the mean values to the fiducial values in 7.3 allows to find a shift in the mean values for the first three Hubble slow-roll parameters. This shift also already appears in the consideration of the contours using three free parameters. It is likely due to the strong correlations in the first three slow-roll parameters that lead to a region where the Markov chain finds very

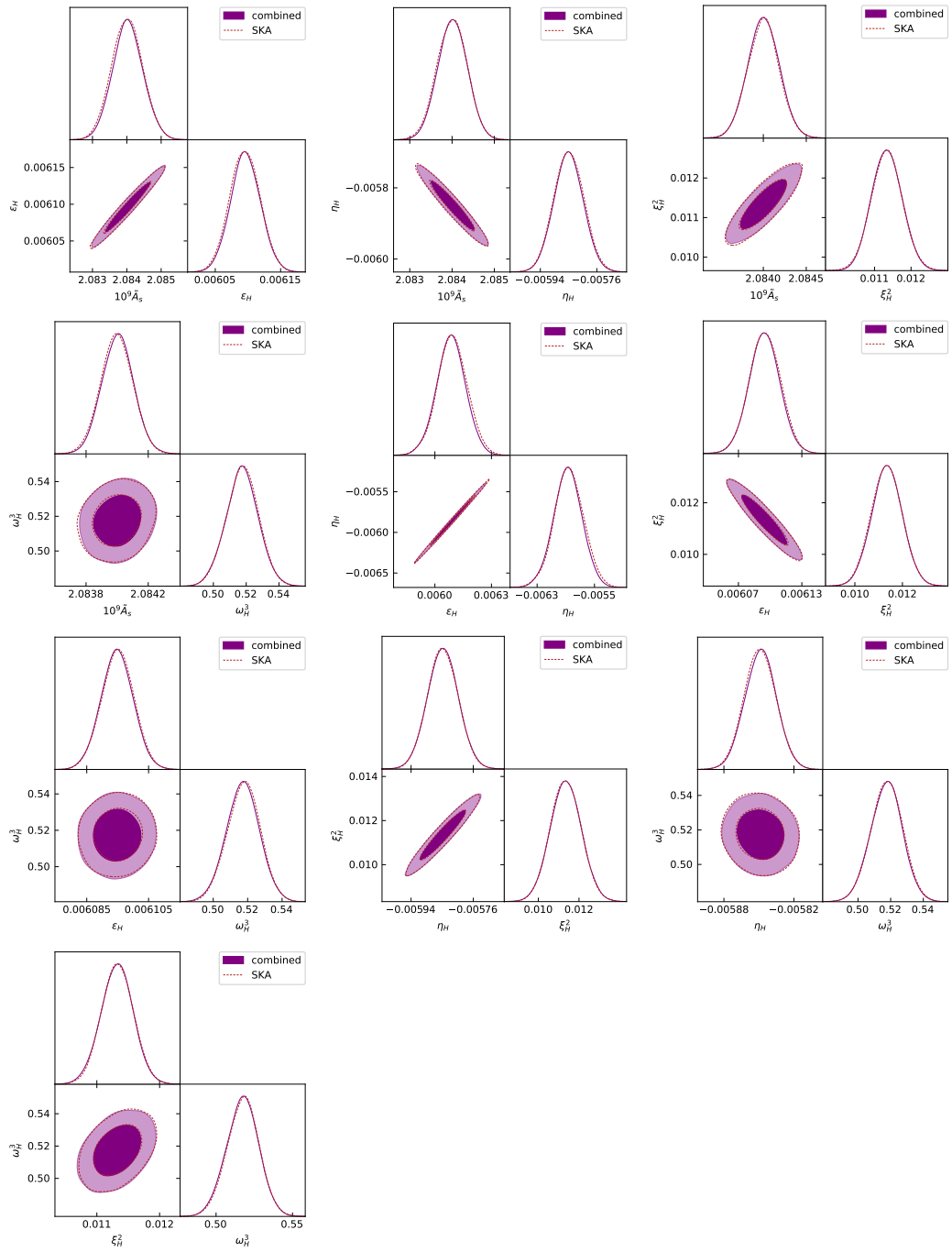

Figure 9.2: Two-dimensional contours from Planck and SKA combined (purple). The two-dimensional SKA contours are overlaid in red.

likely parameter combinations.

Considering only the marginalized distributions for each of the parameters and comparing them and the width of the 95% intervals to the Planck 2018 results allows to find the impact SKA would have on their constraints. For the amplitude $\tilde{A}_s$ the

Table 9.2: Mean values 95% confidence limits for 2D Markov chains using combined SKA and Planck 2018 likelihoods

Param	mean	95% interval
$10^9\tilde{A}_s$	2.08403	$[2.08318, 2.08491]$
ϵ_H	0.006096	$[0.006052, 0.006142]$
$10^9\tilde{A}_s$	2.08401	$[2.08333, 2.08468]$
η_H	-0.005850	$[-0.005940, -0.005758]$
$10^9\tilde{A}_s$	2.08400	$[2.08365, 2.08436]$
ξ_H^2	0.01134	$[0.01055, 0.01215]$
$10^9\tilde{A}_s$	2.08400	$[2.08381, 2.08420]$
ω_H^3	0.518	$[0.498, 0.537]$
ϵ_H	0.00609	$[0.00593, 0.00624]$
η_H	-0.00587	$[-0.00628, -0.00549]$
ϵ_H	0.006095	$[0.006066, 0.006123]$
ξ_H^2	0.0113	$[0.0101, 0.0126]$
ϵ_H	0.006095	$[0.006085, 0.006105]$
ω_H^3	0.517	$[0.498, 0.536]$
η_H	-0.005848	$[-0.005935, -0.005760]$
ξ_H^2	0.0113	$[0.0099, 0.0128]$
η_H	-0.005849	$[-0.005875, -0.005822]$
ω_H^3	0.517	$[0.498, 0.536]$
ξ_H^2	0.01132	$[0.01081, 0.01182]$
ω_H^3	0.517	$[0.496, 0.538]$

Table 9.3: Mean values and 95% intervals for Hubble slow-roll parameters using Planck 2018 and SKA combined.

	SKA+Planck (10000 hrs)		SKA+Planck (1000 hrs)	
Parameter	mean	95% CL	mean	95% CL
$\tilde{A}_s$	2.075	$[2.048, 2.106]$	2.075	$[2.046, 2.110]$
ϵ_H	0.00410	< 0.00951	0.0043	< 0.0101
η_H	-0.0101	$[-0.0197, 0.0022]$	-0.0097	$[-0.0198, 0.0032]$
ξ_H^2	0.011	$[0.000, 0.023]$	0.011	$[-0.002, 0.024]$
ω_H^3	0.51	$[0.41, 0.61]$	0.51	$[0.33, 0.67]$

one dimensional marginalized constraint is stronger by about a factor three, while constraints on the first and second slow-roll parameter are improved by less than

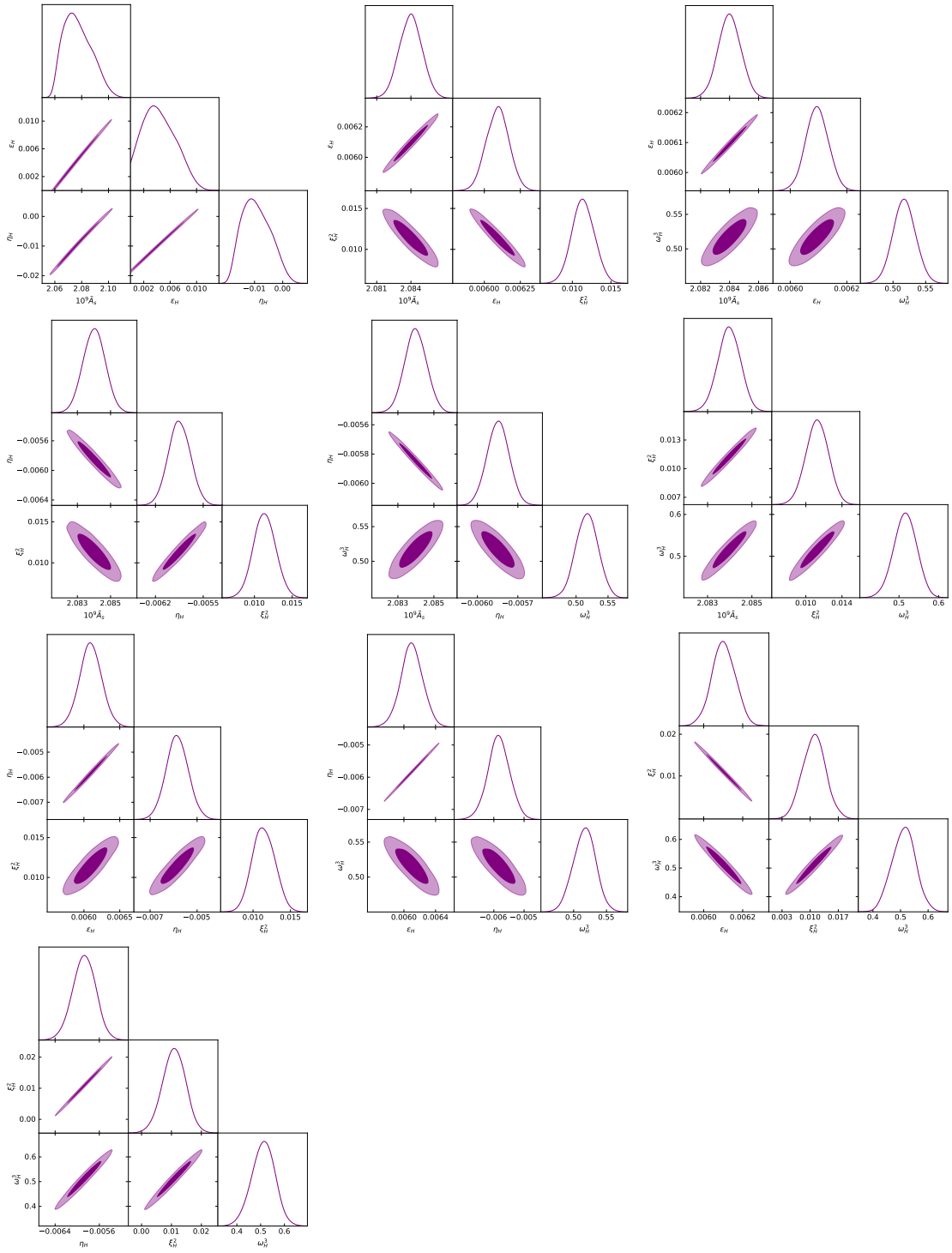

Figure 9.3: Three-dimensional contours from Planck and SKA combined.

a factor of two. In contrast to this relatively modest improvement the constraints on the third and fourth slow-roll parameters are very strong. The 95% intervals

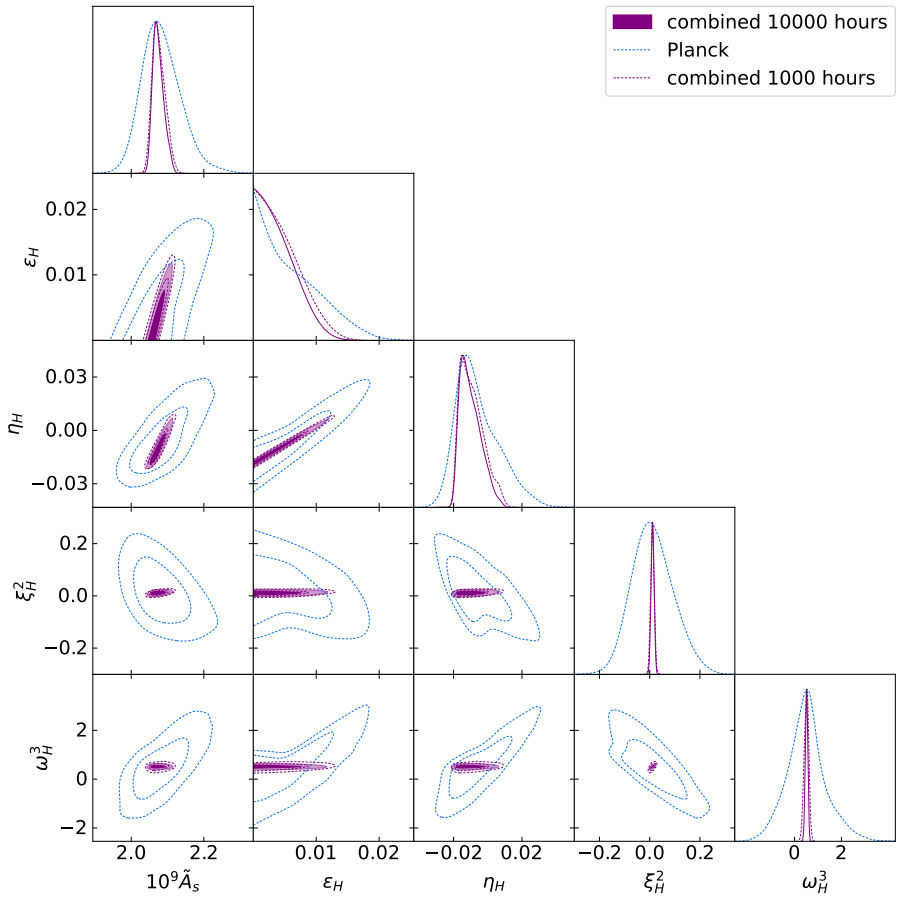

Figure 9.4: Five-dimensional contours using the SKA likelihood in 6.4 and the TT, TE, EE, lowE data from Planck 2018. Depicted are the combined contours with observation time for SKA at 10000 hours (purple), at 1000 hours (purple dashed) as well as the contours from Planck alone (blue dashed).

shrink by more than an order of magnitude. Comparing their values to the 95% intervals found for two free parameters in Table 9.2 allows to find that, while all of the constraints grow weaker when more parameters are included, the constraints on $\tilde{A}_s$, ϵ_H and η_H do so by a much larger factor than the other two. The reason for that can be found by looking at the marginalized contours in figures 9.4 and 9.3 where the strong correlations between the parameters $\{\tilde{A}_s, \epsilon_H\}$ and $\{\epsilon_H, \eta_H\}$ lead to very strong correlations in the marginalized contours whenever all three of these parameters are considered at the same time. This leads to comparatively wide one-dimensional marginalized distributions and thus to large 95% confidence limits.

In order to understand why the SKA can constrain the slow-roll parameters this much more precisely than the Planck 2018 data, it is necessary to consider the construction of the primordial power spectrum in section 6.1.2. The approximation of the Hubble function using the slow-roll parameters is designed as a Taylor series

around the field value at horizon crossing of the pivot scale. Thus, any power spectrum computed using this approximation takes approximately the same value at the pivot scale. For comoving wave numbers close to the pivot scale the effect of varying the slow-roll parameters and with them the coefficients in the Taylor series in expression 6.5 is not very large since the field values at horizon crossing of these scales are also close to the field value at horizon crossing of the pivot scale. For comoving wave numbers far away from the pivot scale the effect of the slow-roll parameters on the values of the power spectrum is large. From the figures comparing the angular power spectra to the noise 7.6 it becomes clear that Planck can only measure at low multipole order ℓ corresponding to low comoving wave numbers. In contrast, the SKA can probe larger comoving wave numbers, see Figure 6.5. Here, the impact different values for the slow-roll parameters have on the 21cm power spectrum can be seen. Especially for large comoving wave numbers the values of the power spectrum changes significantly. For the largest scales probed by the SKA the signal is about a factor 100 stronger than the noise allowing to resolve the relatively small differences due to varying slow-roll parameters.

The purple dashed lines in Figure 9.4 allow to find the impact of decreasing the observation time for the SKA to 1000 hours. This leads to a higher noise level than the one in Figure 6.5 and makes the results more comparable to Muñoz et al. [2017]. This decrease of the observation time leads to a slight increase in the sizes of the marginalized one and two-dimensional distributions. Nevertheless, the constraints on the slow-roll parameters do not appear to be impacted significantly. One of the reasons might be that the likelihoods in this case are not perfectly Gaussian. In addition the Planck likelihood is not impacted by the decrease in the observation time, so the scaling would only impact the SKA likelihood and not necessarily the combined likelihood.

10 Summary and Conclusion

This thesis outlines a path from the beginning of single field inflation and quantum fluctuations in the early Universe to large scale structures in the Universe at redshift 8. First, the motivation for postulating a period of accelerated expansion is explained. Then, working in the framework of single field inflation, quantum fluctuations are used to explain curvature fluctuations in the primordial spectrum after the end of inflation. These can explain the anisotropies in the CMB, which are used as a first probe of the inflationary scenario. The fluctuations are then further evolved with the Boltzmann code CLASS to derive the density power spectrum at redshifts 8 to 10. At these redshifts the 21 cm power spectrum is computed and used to demonstrate the usefulness of a measurement of the 21 cm brightness fluctuations performed with the SKA.

The two-dimensional parameter distributions obtained using the SKA exhibit very strong degeneracies making the analysis of SKA alone numerically challenging. Instead, the SKA likelihood was combined with the Planck 2018 data to demonstrate that the inclusion of a simulated SKA survey of the redshift region from 8 to 10 allows to significantly decrease the constraints on the Hubble slow-roll parameters as was shown in Figure 9.4. Similarly the spectral index and its runnings can be much better constrained with the SKA as can be seen in Figure 9.1. The increase in precision can be attributed to the larger comoving wave numbers probed by the SKA. The construction of the primordial spectrum from the spectral index and its runnings is an expansion around the pivot scale, while the construction using the Hubble slow-roll parameters relies on the expansion of the Hubble function around the field value at horizon crossing of the pivot scale. For both of these it is immediately clear that changes in the parameters used to construct the primordial spectrum have a small effect close to the pivot scale, while their effect becomes more pronounced far away from it. This leads to the stronger constraining power of the SKA compared to the CMB observations of the Planck satellite.

There are several ways to alter the analysis that might be interesting to explore. One of them is to construct the primordial power spectrum following the method described in Powell and Kinney [2007]. There the shape of the Hubble function is not restricted to the polynomial shape assumed in this thesis. Another way might be to consider the potential slow-roll parameters as in Lesgourgues and Valkenburg [2007] to directly constrain the inflaton potential. The drawback in that case is that the conditions defining the end of inflation are more precisely expressed in terms of the Hubble slow-roll parameters.

While the redshift range chosen in the thesis allows for a relatively easy computation of the SKA likelihoods, it is possible to consider larger and different redshift

ranges as shown in Mao et al. [2008] and Sprenger et al. [2019]. To incorporate these regions the computation of the likelihood needs to be altered to include the effects of a position dependent neutral hydrogen fraction for smaller redshifts as well as a position dependent spin temperature for larger redshifts. This would allow to access a larger amount of data, with an appropriate observation time this could lead to stronger constraints on the slow-roll parameters. To access even lower redshift regions other experiments probing the large scale structures at redshifts of order unity could be considered. However, due to the effect of nonlinear structure formation inferring the primordial power spectrum from these experiments is challenging.

Acknowledgments

I would like to thank the ITP for providing the infrastructure and computing power necessary for the analysis in this work. In addition to my supervisor Tilman Plehn I would like to thank Björn Malte Schäfer for the insight into cosmology he provided. I would also like to thank Tanmoy Modak for our productive collaboration.

Appendix

A Nuisance parameters

For the generation of the two and three-dimensional Markov chains the nuisance parameters in the generation of the Planck 2018 likelihoods were fixed in order to understand the correlation between two parameters separate from all others. Table A.1 lists their mean values. In the generation of the two and three-dimensional Markov chains they are fixed to the mean values in this table.

Table A.1: Mean values for the nuisance parameters used in the generation of the 2D and 3D Markov chains whenever Planck 2018 likelihoods are used.

Param	mean
A_{cib217}	47.6
xi_{szcib}	0.511
A_{sz}	5.228
$ps_{A100100}$	263.7
$ps_{A143143}$	49.15
$ps_{A143217}$	43.91
$ps_{A217217}$	116
ksz_{norm}	3.712
$gal545_{A100}$	8.887
$gal545_{A143}$	10.94
$gal545_{A143217}$	18.64
$gal545_{A217}$	93.52
$galf_{TEA100}$	0.1161
$galf_{TEA100143}$	0.1361
$galf_{TEA100217}$	0.4804
$galf_{TEA143}$	0.2281
$galf_{TEA143217}$	0.6651
$galf_{TEA217}$	2.076
$10^{+3}calib_{100T}$	999.7
$10^{+3}calib_{217T}$	998.2
A_{planck}	1.001

B SKA with Four Slow-roll Parameters

Not all of the combinations containing four slow-roll parameters accumulated a sensible number of points for a computation time of 48 hours. This is likely due to the strong degeneracies identified in section 8.2.2. The four-dimensional Markov chains that do not contain the combination $\{\tilde{A}_s, \epsilon_H, \eta_H\}$ do not suffer from this problem. They are shown in B.1.

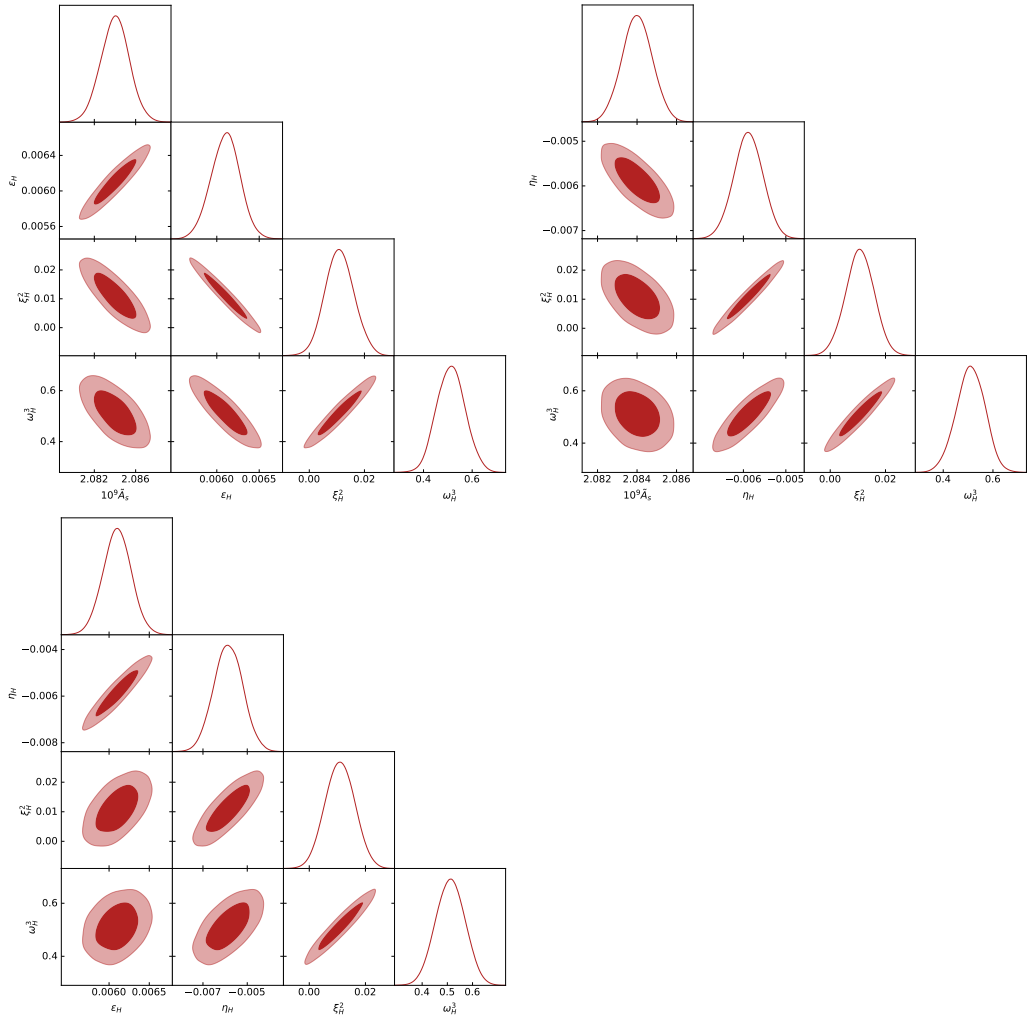

Figure B.1: SKA contours generated by varying four parameters at the same time.

C Lists

C.1 List of Figures

4.1 Angular power spectra as measured by the Planck experiment in 2018 Akrami et al. [2020]. The blue line represents a ΛCDM best fit, $\mathcal{D}_\ell = \ell(\ell+1)C_\ell/(2\pi)$. The lower part of the panel shows the residuals. 30

6.1 Approximated primordial power spectrum allowing for different order in the power series expansion. The spectral index and its runnings are chosen according to the mean values in Akrami et al. [2020] . . . 36
6.2 Inflaton potentials reconstructed from elements of a Monte Carlo Markov chain used to constrain Planck 38
6.3 Simulated 21cm power spectrum according to section 6.4. The primordial spectrum is constructed using equation (6.1), the evolution until redshift 9 is performed by CLASS. 40
6.4 Relative difference of the approximations to the direct solution. The primordial spectrum is constructed using equation (6.1), the evolution until redshift 9 is performed by CLASS. The grey dot marks the position of the pivot scale. 41
6.5 Comparison between 21cm power spectrum and the noise power spectrum computed through (6.35). The grey lines denote the maximal and minimal scales considered. 44

7.1 Contours of the ΛCDM parameters taken from Akrami et al. [2020]. The different colors in the plot represent different sets of modes considered. 47
7.2 68% (dark blue) and 95% (blue) confidence limits for the ΛCDM parameters. Used joint TT, TE, EE data, EE likelihood at low multipoles and TT likelihood at high multipoles. 48
7.3 68% (dark blue) and 95% (blue) confidence limits for the ΛCDM parameters and a modified power spectrum. Used joint TT, TE, EE data, EE likelihood at low multipoles, the TT likelihood at high multipoles. 51
7.4 Contours for Hubble slow-roll parameters taken from Akrami et al. [2020]. Solid contours are Planck TT, TE, EE, lowE, lensing and BK15. Dashed contours are Planck TT, TE, EE, lowE. 53
7.5 68% (dark blue) and 95% (blue) confidence limits for the Hubble slow-roll parameters. Used joint TT, TE, EE data and EE likelihood at low multipoles and TT likelihood at high multipoles. 54

7.6 Different realizations of the angular CMB spectra, allowed by the Planck TT, TE and EE data with Planck noise levels. 55
7.7 Two-dimensional 68% (dark blue) and 95% (blue) confidence limits for the Hubble slow-roll parameters. Used joint TT, TE, EE data, EE likelihood at low multipoles and TT likelihood at high multipoles. 56

8.1 68% and 95% level contours ΛCDM parameters and the spectral index and its runnings for SKA with 10000 hours observation time (red filled) and SKA with 1000 hours observation time (red dashed). Used the SKA likelihood described in section 6.4. 59
8.2 68% and 95% level contours for the scalar amplitude, the spectral index and its runnings for SKA with 10000 hours observation time (red filled) and SKA with 1000 hours observation time (red dashed). Used the SKA likelihood described in section 6.4. 61
8.3 Two-dimensional 68% and 95% level contours using SKA likelihoods as computed in 6.4. 63
8.4 Markov chain points in three-dimensional parameters space generated with SKA likelihoods computed as described in 6.4. 66
8.5 Three-dimensional 68% and 95% level contours using SKA likelihoods as computed in 6.4.. 67
8.6 Comparison between slices and 2D SKA contours, each row corresponds to slices taken from one 3D SKA chain. 69
8.7 Comparison between slices and 2D SKA contours, each row corresponds to slices taken from one 3D SKA chain. 70
8.8 Comparison between slices and 2D SKA contours, each row corresponds to slices taken from one 3D SKA chain. 71

9.1 68% and 95% level contours for the scalar amplitude, the spectral index and its runnings for SKA with 10000 hours observation time + Planck 2018 (TT, TE, EE, lowE, highT) (purple), SKA with 10000 hours observation time (red dashed) and Planck 2018 (TT, TE, EE, lowE, highT) (blue dashed). Used the SKA likelihood described in section 6.4. 73
9.2 Two-dimensional contours from Planck and SKA combined (purple). The two-dimensional SKA contours are overlaid in red. 75
9.3 Three-dimensional contours from Planck and SKA combined. 77
9.4 Five-dimensional contours using the SKA likelihood in 6.4 and the TT, TE, EE, lowE data from Planck 2018. Depicted are the combined contours with observation time for SKA at 10000 hours (purple), at 1000 hours (purple dashed) as well as the contours from Planck alone (blue dashed). 78

B.1 SKA contours generated by varying four parameters at the same time. 85

C.2 List of Tables

7.1 Mean values 95% confidence interval for the ΛCDM found with Planck 2018 data . . . 49
7.2 Mean values 95% confidence interval for the spectral index and its runnings using Planck 2018 data . . . 50
7.3 Mean values and 95% intervals for the cosmological and slow-roll parameters using Planck 2018 TT, TE, EE, lowE data . . . 53
7.4 Mean values and error bars for 2D Markov chains using Planck 2018 data . . . 57

8.1 Mean values and error bars for the spectral index and its runnings using the SKA likelihoods constructed as in 6.4 . . . 60
8.2 Mean values and error bars for 2D Markov chains using SKA likelihoods as constructed in 6.4 . . . 64

9.1 Mean values and 95% intervals for the spectral amplitude, index and its runnings using Planck 2018 and SKA combined. . . . 73
9.2 Mean values 95% confidence limits for 2D Markov chains using combined SKA and Planck 2018 likelihoods . . . 76
9.3 Mean values and 95% intervals for Hubble slow-roll parameters using Planck 2018 and SKA combined. . . . 76

A.1 Mean values for the nuisance parameters used in the generation of the 2D and 3D Markov chains whenever Planck 2018 likelihoods are used. . . . 84

D Bibliography

P. A. R. Ade, N. Aghanim, M. Arnaud, F. Arroja, M. Ashdown, J. Aumont, C. Baccigalupi, M. Ballardini, A. J. Banday, and et al. Planck2015 results. *Astronomy and Astrophysics*, 594:A20, Sep 2016. ISSN 1432-0746. doi: 10.1051/0004-6361/201525898. URL http://dx.doi.org/10.1051/0004-6361/201525898.

Y. Akrami et al. Planck 2018 results. X. Constraints on inflation. *Astron. Astrophys.*, 641:A10, 2020. doi: 10.1051/0004-6361/201833887.

Benjamin Audren, Julien Lesgourgues, Karim Benabed, and Simon Prunet. Conservative constraints on early cosmology with montepython. *Journal of Cosmology and Astroparticle Physics*, 2013(02):001001, Feb 2013. ISSN 1475-7516. doi: 10.1088/1475-7516/2013/02/001. URL http://dx.doi.org/10.1088/1475-7516/2013/02/001.

David J. Bacon, Richard A. Battye, Philip Bull, Stefano Camera, Pedro G. Ferreira, Ian Harrison, David Parkinson, Alkistis Pourtsidou, Mário G. Santos, and et al. Cosmology with phase 1 of the square kilometre array red book 2018: Technical specifications and performance forecasts. *Publications of the Astronomical Society of Australia*, 37, 2020. ISSN 1448-6083. doi: 10.1017/pasa.2019.51. URL http://dx.doi.org/10.1017/pasa.2019.51.

Vernon Barger, Yu Gao, Yi Mao, and Danny Marfatia. Inflationary Potential from 21 cm Tomography and Planck. *Phys. Lett. B*, 673:173–178, 2009a. doi: 10.1016/j.physletb.2009.02.021.

Vernon Barger, Yu Gao, Yi Mao, and Danny Marfatia. Inflationary potential from 21 cm tomography and planck. *Physics Letters B*, 673(3):173178, Mar 2009b. ISSN 0370-2693. doi: 10.1016/j.physletb.2009.02.021. URL http://dx.doi.org/10.1016/j.physletb.2009.02.021.

Daniel Baumann. Tasi lectures on inflation, 2012.

Daniel Baumann, Mark G. Jackson, Peter Adshead, Alexandre Amblard, Amjad Ashoorioon, Nicola Bartolo, Rachel Bean, Maria Beltran, Francesco de Bernardis, Simeon Bird, and et al. Probing inflation with cmb polarization. *AIP Conference Proceedings*, 2009. doi: 10.1063/1.3160885. URL http://dx.doi.org/10.1063/1.3160885.

N. D. Birrell and P. C. W. Davies. *Quantum Fields in Curved Space*. Cambridge Monographs on Mathematical Physics. Cambridge University Press, 1982. doi: 10.1017/CBO9780511622632.

Diego Blas, Julien Lesgourgues, and Thomas Tram. The cosmic linear anisotropy solving system (class). part ii: Approximation schemes. *Journal of Cosmology and Astroparticle Physics*, 2011(07):034034, Jul 2011. ISSN 1475-7516. doi: 10.1088/1475-7516/2011/07/034. URL http://dx.doi.org/10.1088/1475-7516/2011/07/034.

Judd D. Bowman, Miguel F. Morales, and Jacqueline N. Hewitt. Constraints on fundamental cosmological parameters with upcoming epoch of reionization observations. *Astrophys. J.*, 661:1–9, 2007. doi: 10.1086/516560.

Thejs Brinckmann and Julien Lesgourgues. Montepython 3: boosted mcmc sampler and other features, 2018.

Peter Dewdney. Ska1 system baselinev2 description. 2015.

Scott Dodelson. *Modern cosmology*. 2003. URL https://ui.adsabs.harvard.edu/abs/2003moco.book.....D.

Daniel J. Eisenstein and Wayne Hu. Baryonic features in the matter transfer function. *The Astrophysical Journal*, 496(2):605614, Apr 1998. ISSN 1538-4357. doi: 10.1086/305424. URL http://dx.doi.org/10.1086/305424.

Alan H. Guth. The Inflationary Universe: A Possible Solution to the Horizon and Flatness Problems. *Phys. Rev. D*, 23:347–356, 1981. doi: 10.1103/PhysRevD.23.347.

Jan Hamann, Julien Lesgourgues, and Wessel Valkenburg. How to constrain inflationary parameter space with minimal priors. *Journal of Cosmology and Astroparticle Physics*, 2008(04):016, Apr 2008. ISSN 1475-7516. doi: 10.1088/1475-7516/2008/04/016. URL http://dx.doi.org/10.1088/1475-7516/2008/04/016.

W. K. Hastings. Monte Carlo Sampling Methods using Markov Chains and their Applications. *Biometrika*, 57(1):97–109, April 1970. doi: 10.1093/biomet/57.1.97.

Wayne Hu and Martin White. A cmb polarization primer. *New Astronomy*, 2(4):323344, Oct 1997. ISSN 1384-1076. doi: 10.1016/s1384-1076(97)00022-5. URL http://dx.doi.org/10.1016/S1384-1076(97)00022-5.

Marc Kamionkowski, Arthur Kosowsky, and Albert Stebbins. Statistics of cosmic microwave background polarization. *Physical Review D*, 55(12):73687388, Jun 1997. ISSN 1089-4918. doi: 10.1103/physrevd.55.7368. URL http://dx.doi.org/10.1103/PhysRevD.55.7368.

Lloyd Knox. Determination of inflationary observables by cosmic microwave background anisotropy experiments. *Physical Review D*, 52(8):43074318, Oct 1995. ISSN 0556-2821. doi: 10.1103/physrevd.52.4307. URL http://dx.doi.org/10.1103/PhysRevD.52.4307.

Kazunori Kohri, Yoshihiko Oyama, Toyokazu Sekiguchi, and Tomo Takahashi. Precise Measurements of Primordial Power Spectrum with 21 cm Fluctuations. *JCAP*, 10:065, 2013. doi: 10.1088/1475-7516/2013/10/065.

Samuel M. Leach, Andrew R. Liddle, Jérôme Martin, and Dominik J. Schwarz. Cosmological parameter estimation and the inflationary cosmology. *Physical Review D*, 66(2), Jul 2002. ISSN 1089-4918. doi: 10.1103/physrevd.66.023515. URL http://dx.doi.org/10.1103/PhysRevD.66.023515.

Julien Lesgourgues and Wessel Valkenburg. New constraints on the observable inflaton potential from WMAP and SDSS. *Phys. Rev. D*, 75:123519, 2007. doi: 10.1103/PhysRevD.75.123519.

Julien Lesgourgues, Alexei A Starobinsky, and Wessel Valkenburg. What do wmap and sdss really tell us about inflation? *Journal of Cosmology and Astroparticle Physics*, 2008(01):010, Jan 2008. ISSN 1475-7516. doi: 10.1088/1475-7516/2008/01/010. URL http://dx.doi.org/10.1088/1475-7516/2008/01/010.

Antony Lewis. GetDist: a Python package for analysing Monte Carlo samples. 2019. URL https://getdist.readthedocs.io.

Antony Lewis and Sarah Bridle. Cosmological parameters from cmb and other data: A monte carlo approach. *Physical Review D*, 66(10), Nov 2002. ISSN 1089-4918. doi: 10.1103/physrevd.66.103511. URL http://dx.doi.org/10.1103/PhysRevD.66.103511.

Andrew R. Liddle, Paul Parsons, and John D. Barrow. Formalizing the slow-roll approximation in inflation. *Physical Review D*, 50(12):72227232, Dec 1994. ISSN 0556-2821. doi: 10.1103/physrevd.50.7222. URL http://dx.doi.org/10.1103/PhysRevD.50.7222.

David MacKay. *InformationTheory, Inference, and Learning Algorithms*, volume 50. 01 2003. ISBN 978-0-521-64298-9. doi: 10.1109/TIT.2004.834752.

Juan Maldacena. Non-gaussian features of primordial fluctuations in single field inflationary models. *Journal of High Energy Physics*, 2003(05):013013, May 2003. ISSN 1029-8479. doi: 10.1088/1126-6708/2003/05/013. URL http://dx.doi.org/10.1088/1126-6708/2003/05/013.

Yi Mao, Max Tegmark, Matthew McQuinn, Matias Zaldarriaga, and Oliver Zahn. How accurately can 21 cm tomography constrain cosmology? *Phys. Rev. D*, 78: 023529, 2008. doi: 10.1103/PhysRevD.78.023529.

Matthew McQuinn, Oliver Zahn, Matias Zaldarriaga, Lars Hernquist, and Steven R. Furlanetto. Cosmological parameter estimation using 21 cm radiation from the epoch of reionization. *Astrophys. J.*, 653:815–830, 2006. doi: 10.1086/505167.

Philipp M. Merkel and Björn Malte Schäfer. Parameter constraints from weak-lensing tomography of galaxy shapes and cosmic microwave background fluctuations. *Monthly Notices of the Royal Astronomical Society*, 469(3):27602770, May 2017. ISSN 1365-2966. doi: 10.1093/mnras/stx1044. URL http://dx.doi.org/10.1093/mnras/stx1044.

Nicholas Metropolis, Arianna W. Rosenbluth, Marshall N. Rosenbluth, Augusta H. Teller, and Edward Teller. Equation of State Calculations by Fast Computing Machines. *J. Chem. Phys.*, 21(6):1087–1092, June 1953. doi: 10.1063/1.1699114.

Julian B. Muñoz, Ely D. Kovetz, Alvise Raccanelli, Marc Kamionkowski, and Joseph Silk. Towards a measurement of the spectral runnings. *JCAP*, 05:032, 2017. doi: 10.1088/1475-7516/2017/05/032.

Viatcheslav Mukhanov. *Physical Foundations of Cosmology*. Cambridge University Press, 2005. doi: 10.1017/CBO9780511790553.

Viatcheslav F. Mukhanov, H. A. Feldman, and Robert H. Brandenberger. Theory of cosmological perturbations. Part 1. Classical perturbations. Part 2. Quantum theory of perturbations. Part 3. Extensions. *Phys. Rept.*, 215:203–333, 1992. doi: 10.1016/0370-1573(92)90044-Z.

Luis E. Padilla, Luis O. Tellez, Luis A. Escamilla, and Jose Alberto Vazquez. Cosmological parameter inference with bayesian statistics. *Universe*, 7(7):213, Jun 2021. ISSN 2218-1997. doi: 10.3390/universe7070213. URL http://dx.doi.org/10.3390/universe7070213.

Alkistis Pourtsidou. Synergistic tests of inflation. 12 2016.

BrianA. Powell and WilliamH. Kinney. Limits on primordial power spectrum resolution: An inflationary flow analysis. *JCAP*, 0708:006, 2007. doi: 10.1088/1475-7516/2007/08/006.

Jonathan Pritchard et al. Cosmology from EoR/Cosmic Dawn with the SKA. *PoS*, AASKA14:012, 2015. doi: 10.22323/1.215.0012.

Antonio Riotto. Inflation and the theory of cosmological perturbations. *ICTP Lect. Notes Ser.*, 14:317–413, 2003.

D. S. Salopek and J. R. Bond. Nonlinear evolution of long-wavelength metric fluctuations in inflationary models. *Phys. Rev. D*, 42:3936–3962, Dec 1990. doi: 10.1103/PhysRevD.42.3936. URL https://link.aps.org/doi/10.1103/PhysRevD.42.3936.

Tim Sprenger, Maria Archidiacono, Thejs Brinckmann, Sébastien Clesse, and Julien Lesgourgues. Cosmology in the era of euclid and the square kilometre array. *Journal of Cosmology and Astroparticle Physics*, 2019(02):047047, Feb 2019. ISSN

1475-7516. doi: 10.1088/1475-7516/2019/02/047. URL http://dx.doi.org/10.1088/1475-7516/2019/02/047.

Ewan D. Stewart and Jin-Ook Gong. The density perturbation power spectrum to second-order corrections in the slow-roll expansion. *Physics Letters B*, 510 (1-4):19, Jun 2001. ISSN 0370-2693. doi: 10.1016/s0370-2693(01)00616-5. URL http://dx.doi.org/10.1016/S0370-2693(01)00616-5.

Ewan D. Stewart and David H. Lyth. A more accurate analytic calculation of the spectrum of cosmological perturbations produced during inflation. *Physics Letters B*, 302(2-3):171175, Mar 1993a. ISSN 0370-2693. doi: 10.1016/0370-2693(93)90379-v. URL http://dx.doi.org/10.1016/0370-2693(93)90379-V.

Ewan D. Stewart and David H. Lyth. A More accurate analytic calculation of the spectrum of cosmological perturbations produced during inflation. *Phys. Lett. B*, 302:171–175, 1993b. doi: 10.1016/0370-2693(93)90379-V.

Max Tegmark and Matias Zaldarriaga. Fast fourier transform telescope. *Phys. Rev. D*, 79:083530, Apr 2009. doi: 10.1103/PhysRevD.79.083530. URL https://link.aps.org/doi/10.1103/PhysRevD.79.083530.

Matias Zaldarriaga and Uro Seljak. All-sky analysis of polarization in the microwave background. *Physical Review D*, 55(4):18301840, Feb 1997. ISSN 1089-4918. doi: 10.1103/physrevd.55.1830. URL http://dx.doi.org/10.1103/PhysRevD.55.1830.

Erklärung:

Ich versichere, dass ich diese Arbeit selbstständig verfasst habe und keine anderen als die angegebenen Quellen und Hilfsmittel benutzt habe.

Heidelberg, den 20.12.2021 .....